The Physics of a 4th Generation Light Source

A thesis submitted to The Department of Physics

of the University of Strathclyde

for the degree of Doctor of Philosophy.

Lawrence Thomas Campbell

November 9, 2011

Abstract

This thesis describes an unaveraged 3D mathematical model and parallel code of the free electron laser. It is unique in that it is a 3D model which does not perform limiting assumptions performed by commonly used FEL codes. This allows it to model the FEL with a higher resolution, and to model effects which other codes cannot.

The code is written in Fortran 90. The enhanced frequency range results in an increased memory and process uptake, and so the code is written for use on parallel processors using the MPI standard. The problems associated with finding an efficient method of parallelization of the FEL system are described and solutions are considered. The enhanced frequency range also results in a model of diffraction in the transverse dimensions which is frequency dependant, which becomes problematic at low frequencies. To solve this, a low frequency cut-off is defined, and the frequencies below the cut-off are filtered out during the simulations.

Several simulations are presented to test the code against previously published results with the enhanced frequency range in 1D. Then 3D simulations are presented showing the amplification arising from effects which cannot be predicted in more commonly used codes. Finally, a new effect is reported involving the evolution of short chirped electron bunches in an undulator.

Contents

List of Figures

Acknowledgements

Thanks must go to my supervisor, Dr Brian M^{c}Neil, for his time and patience. Thanks to the EPSRC for providing funding. Thanks to my friends and family for their patience, and to my parents for their support. Thanks and love to Kirsty.

Chapter 1

Introduction

The Free Electron Laser [1] is a source of intense, spatially coherent radiation, with devices operating at wavelengths ranging from microwave through to X-ray. It has been of interest for decades now as a promising source of high brightness, short pulse hard X-rays, being referred to as a Fourth Generation Light Source.

Here the term "Light Source" refers to a source of synchrotron radiation. Synchrotron radiation is produced when a charged particle is accelerated. When a relativistic charged particle travels in the arc of a circle it emits radiation tangential to the direction of propagation focused into a narrow cone of angle $\approx \frac{1}{\gamma}$ [2], γ being the relativistic Lorentz factor associated with energy $E = \gamma m_0 c^2$. To produce synchrotron radiation for experimental purposes, beams of electrons are accelerated through circular orbits in large toroidal devices, known as synchrotrons or storage rings. Electrons are used due to their low rest mass.

1.1 Brief History of Synchrotron Radiation

Synchrotron radiation takes its name from the machine in which it was first observed, at the 70MeV electron synchrotron at General Electric in Schenectady, New York in 1947 [3]. It was several years, however, until it was thought to be used experimentally, and was first considered an irritating energy loss. After the spectral and polarization properties of the radiation were measured both at Gen-

eral Electric and at the $250MeV$ synchrotron at the Lebedev Institute in Moscow, Tomboulian and Harteman used it experimentally for the first time in 1956, at the $320MeV$ electron synchrotron at Cornell [4]. Soon after, throughout the 1960's a number of synchrotron, and later, storage ring facilities began operation worldwide with access to users to exploit the radiation for experimental purposes, such as characterization of absorption spectra in solids. These are now known as the 1^{st} generation sources, and were used in parasitic mode, meaning the technology was not expressly designed with the purpose of producing radiation.

Thus, the so-called 2^{nd} generation of dedicated sources began with the SRS (Synchrotron Radiation Source) at Daresbury Laboratory in the UK in 1981. Others which were completed soon after included the National Synchrotron Light Source (NSLS) at Brookhaven National Laboratory, USA, the Photon Factory at the KEK laboratory in Tsukuba, Japan, and the 800MeV SuperACO at Orsay LURE, France. They were now specifically designed to produce synchrotron radiation, resulting in more useful spectral output.

The next generation, the 3^{rd}, brought yet higher intensities, with lower emittance electron beams resulting in higher brightness radiation output. The emittance is a measure of the divergence of the electron and photon beams. A lower emittance means a higher quality beam. The 3^{rd} generation facilities specialize in either V-UV and soft X-ray or hard X-ray radiation [4]. By now, devices called wigglers and undulators were commonly used in straight sections between the bends of the storage rings to produce radiation of higher intensities. These devices are composed of a periodic array of magnetic dipoles which force a relativistic electron beam to oscillate in a direction transverse to its direction of propagation, and were first proposed and operated by Motz in [5] and [6]. The multiple transverse oscillations result in an output many times greater than the output of just one bend. Additionally undulators produce output with narrow spectral lines, enhancing the intensity. The improvements in output led to previously unattainable results, using the radiation for X-ray microscopy and spectromicroscopy experiments on a sub-picosecond time scale. 3^{rd} generation facilities include the European Synchrotron Radiation Facility (the first) in Grenoble,

the Advanced Photon Source at Argonne Laboratory in the US, and Diamond Light Source at Rutherford Appleton Laboratory in the UK. Experiments at Diamond involve characterizing magnetic and electronic properties of materials at the atomic level, probing material under extreme pressure and temperature conditions, and understanding the structure of biological samples.

1.2 The Free Electron Laser

The previous generations of light sources produced radiation by accelerating electrons to force them to spontaneously radiate. The electrons' energy loss due to producing this radiation is negligible. The FEL brings an improvement in output intensity and temporal coherence over previous sources because the electrons give up a significant amount of their kinetic energy to the radiation, resulting in an exponential amplification of the radiation. The interaction is described in the next chapter, but for now it is noted that the desired amplification is achieved by passing both a high quality (low emittance, low energy spread) electron beam and a radiation field through a sufficiently long undulator, and the amplification results from an induced periodic density modulation of the electron beam.

The theory was first described by Madey in 1971 [1], which described what is now known as the low-gain regime of FEL operation. The first lasing and amplification from an FEL was then demonstrated at Stanford [7, 8]. That FEL was a low gain infrared oscillator, where the undulator, enclosed in an optical cavity, amplified radiation over many passes of the device.

The theory of the high gain FEL, in which an exponential amplification of the radiation is achieved within a single pass of the undulator, was subsequently developed in the late 1970's [9, 10, 11, 12, 13, 14]. An important theoretical development showed how the initial synchrotron radiation produced by an electron beam at the start of a long undulator could be subsequently amplified in the high gain regime further along the undulator. This opened the possibility for a high gain X-ray FEL, as no suitable mirrors or seeds existed for these wavelengths. Most current existing VUV/X-ray FEL's exploit this effect, and so are composed

of a long linear electron accelerator followed by a long undulator. The full length of these devices is approximately 1 or a few km, depending on the technology, which varies from one machine to the next. The Japanese XFEL/SPring-8 source is 750m, and is considered a compact source, due to its unique accelerator and compact undulator [15].

A single pass, high gain X-ray FEL generates peak powers on the order of 10^{10}W with pulses 10's of femtoseconds in duration. FLASH was the world's first VUV/soft X-ray FEL, and was completed in 2005, lasing at the wavelength range $6.5 \rightarrow 50$nm, with pulse durations $10 - 50$fs. The LCLS is the first hard X-ray FEL, and reported first lasing in 2009 [16]. Hard X-ray FEL's due to be completed in the near future include (but are not limited to) the European XFEL at DESY in Hamburg, Germany [17], the XFEL/SPring-8 in Japan [15], and SwissFEL in Switzerland [18]. The short, fast radiation pulse durations will enable time-resolved investigations of ultra-fast processes at the atomic scale [19].

1.3 FEL Simulation Codes

Of great importance in the prediction of FEL phenomena and the design of facilities are simulation codes. The most commonly used codes, for example GINGER [20], GENESIS 1.3 [21] and FAST [22], typically make a number of similar assumptions, one of which, known as the Slowly Varying Envelope Approximation or Eikonal Approximation [23], limits the time and spatial resolution of the codes. This is not a severe restriction for describing most FEL's currently in operation [24]. It may be, however, that a code with this assumption will not be adequate to describe FEL's using electron pulses which have a quickly varying current profile, or radiation seeds with a quickly varying intensity profile, with respect to a radiation wavelength [25]. These situations have been previously unattainable, but may soon become a reality in the push towards FEL's either exhibiting greater temporal coherence or of a smaller size.

This thesis presents a 3D theory and Fortran 90 simulation code which is free of this limiting assumption. The resulting code presents significant computational

challenges due to the increased resolution of the model, and these problems are explained and the solutions arrived at described. First of all though, the basic principles behind the theory of the FEL are described.

Chapter 2

Basic Theory of the FEL

2.1 Qualitative Discussion

Synchrotrons are large devices which accelerate electrons around a circular orbit, and the transverse acceleration causes the electrons to radiate. Undulators and wigglers, so-called since they provide a spatially varying magnetic field which causes the electrons to "wiggle" or "undulate," produce radiation of even higher intensities since the electron beam undergoes many transverse oscillations in one pass of the device [2].

By distinction, in the Free Electron Laser, or FEL, radiation is **amplified** by the electron beam. In the most basic terms, the FEL converts a relativistic electron beam's energy into coherent, intense radiation.

The Free Electron Laser consists of an electron beam with energy γmc^2 and

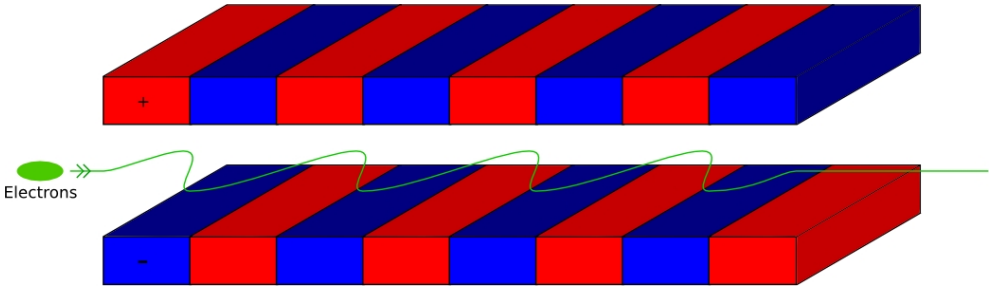

Figure 2.1: Electrons propagating a planar wiggler.

a radiation field copropagating in a spatially varying magnetic field transverse to the direction of propagation. The magnetic field is conventionally supplied by an undulator or wiggler (see figure 2.1). In their simplest configuration, these consist of either two alternating sets of permanent magnetic poles (planar) or two helical coils with opposing current (helical). Each have an associated wiggler wavelength λ_w, peak magnetic field B_w and N_w periods.

The magnetic undulator field forces the electron beam to execute an oscillatory wiggle motion transverse to both the direction of travel and the axis of the magnetic field, see figure 2.1. The resulting transverse electron oscillation allows an energy exchange between radiation and electrons, giving gain or absorption of the radiation field. It differs from conventional solid state lasers in that the electrons are unbound, or free, so the amplified wavelengths are not restricted by the discrete energy states of the atom. The FEL can be fully described by classical electromagnetism [26], and one need not take into account the quantum mechanical recoil of the electrons, except in some extreme situations which are not yet experimentally feasible.

Relativistic effects are key to its inherent tunability. As the beam is relativistic, the undulator wavelength λ_w is twice upshifted by the relativistic factor γ_j in the lab frame, so the resulting wavelength $\lambda_r \propto \lambda_w/\gamma^2$, and the device can be tuned to a different frequency by adjusting the electron beam energy. In practice, there are other limitations which limit the tunability of a single device, such as the length of the undulator and the quality of the electron beam.

Under certain conditions, if the undulator is long enough, the energy exchange results in an exponential amplification of the radiation field due to a cooperative effect, whereby the electrons interact via the common radiation field. The electrons bunch on the scale of a radiation wavelength and coherently amplify the radiation field.

The following sections describe the basic theory of the FEL.

2.1.1 Electron Motion in the Undulator

FEL Spontaneous Emission

Assume the positive z-axis is the direction of electron propagation. Close to the center of the undulator the magnetic field can be described as, in the case of the planar undulator,

$$\mathbf{B}_w = -B_w \sin(k_w z)\hat{\mathbf{y}}, \tag{2.1}$$

and in the case of the helical undulator,

$$\mathbf{B}_w = B_w(\cos(k_w z)\hat{\mathbf{x}} - \sin(k_w z)\hat{\mathbf{y}}), \tag{2.2}$$

where B_w is the peak magnetic field of the undulator, and $k_w = 2\pi/\lambda_w$ is the undulator wavenumber.

An electron traversing the undulator close to the center will be deflected by the Lorentz force, given by

$$F = q(\mathbf{E} + \mathbf{v} \times \mathbf{B}). \tag{2.3}$$

Ignoring for the moment the effect of the radiation field upon the electron, the electron oscillation in x for the planar undulator case will be described by

$$\frac{dp_x}{dt} = -\left|e\right| v_z B_w \sin(k_w z) \tag{2.4}$$

and changing the independent variable to z,

$$\frac{dv_x}{dz} = -\frac{\left|e\right| B_w}{\gamma m} \sin(k_w z) \tag{2.5}$$

$$v_x = \frac{\left|e\right| B_w}{\gamma m k_w} \cos(k_w z) \tag{2.6}$$

$$\frac{dx}{dz} = \frac{\left|e\right| B_w}{\gamma m c k_w} \cos(k_w z) \tag{2.7}$$

where in the last step the approximation $\dfrac{d}{dt} \approx c\dfrac{d}{dz}$ has been made (as the electron is relativistic).

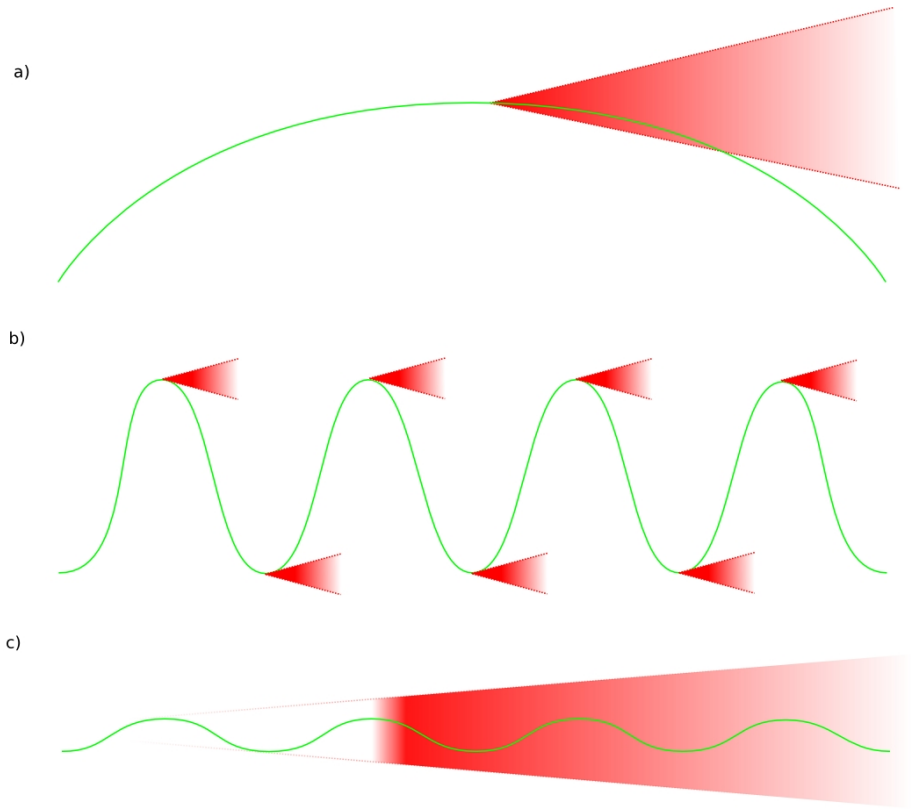

Figure 2.2: The electron path is shown in green and the radiation is shown in red. a) shows the radiation from an electron travelling the arc of a circle, and the radiation is focused into a narrow cone of angle $\frac{1}{\gamma}$ normal to the direction of propagation. The wiggler, shown in b), forces the electron to oscillate transversely, and it executes many such circular arcs, and the output is simply the summation of the multiple source points. If the deviation from the z axis is not as severe, which is the case in the undulator, shown in c), then the radiation from the source points will interfere.

The undulator parameter $a_w = \dfrac{eB_w}{mck_w}$ can now be introduced, so that

$$\frac{dx}{dz} = \frac{a_w}{\gamma}\cos(k_w z) \tag{2.8}$$

If one can assume small deflections from the z axis, then $\dfrac{dx}{dz} \approx \theta$, the angle from the z axis. The radiation from a relativistic electron travelling the arc of a circle is focused into a narrow cone of angle $\approx \dfrac{1}{\gamma}$ in the forward direction. It is easy to see from equation (2.8) that if $a_w \approx 1$ then the electron will overlap with the emitted radiation cone and there will be interference effects present. This is the distinction between a wiggler and an undulator, and is shown in figure 2.2. An undulator has a low value of a_w and produces a spectrum with sharp peaks around a fundamental wavelength and its harmonics, which is a result of this interference effect. In a wiggler the spectrum is more continuous, as there are fewer interference effects present. Depending on the electron beam energy and other parameters, interference effects can still be very pronounced in devices with $a_w \lesssim 10$ [2].

To find which frequencies constructively interfere in the forward direction (the on-axis emission), consider the radiation travelling at the speed of light c, and an electron at $c\bar{\beta}_z < c$, where $\bar{\beta}_z = \dfrac{\bar{v}_z}{c}$, is the speed $\bar{v}_z$ of the electron in the z direction, as a fraction of c, averaged over an undulator period. The emitted radiation is seen to always travel ahead of the electron. Constructive interference will occur if a whole number of radiation wavelengths λ_r propagate ahead of the electron in the time it takes the electron to travel one undulator period λ_w i.e.

$$\frac{\lambda_w}{c\bar{\beta}_z} = \frac{n\lambda_r + \lambda_w}{c} \tag{2.9}$$

which leads to equation

$$\lambda_r = \lambda_w \frac{1 - \bar{\beta}_z}{\bar{\beta}_z}. \tag{2.10}$$

This is the fundamental (n=1) wavelength of the radiation emitted on-axis from an undulator. Similar arguments can be made for the more general case of

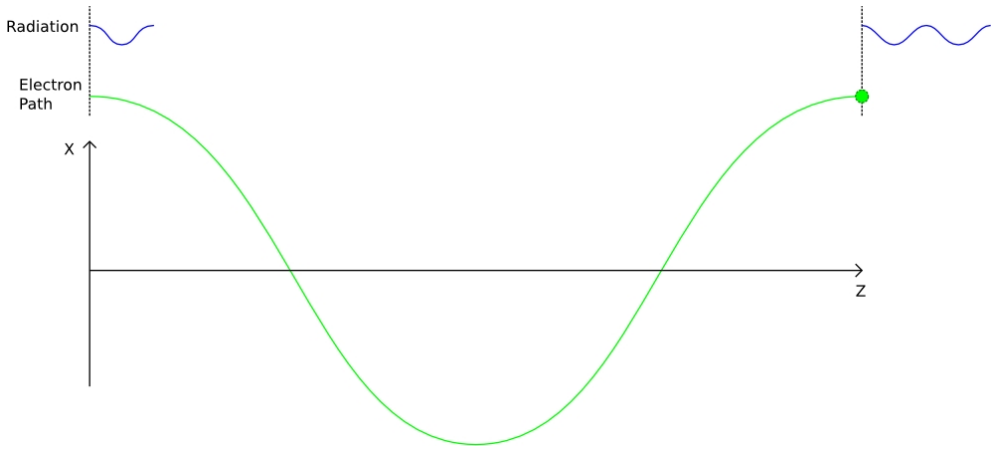

Figure 2.3: Illustration of the condition for resonance. The resonant wavelength is that which slips over the electron by exactly one wavelength during the period of the electron's oscillation. This wavelength then interferes constructively. Frequencies which do not satisfy this condition are annihilated through destructive interference across successive undulator periods.

interference of radiation emitted at angles from the main direction of propagation. One finds the fundamental wavelength increases with the square of increasing angle when observing off-axis. One also finds, upon further analysis, that only odd harmonics are generated on-axis, and even harmonics only off-axis [2]. The interference effect also results in an output focused into a narrower cone of angle $\sim \frac{1}{\gamma\sqrt{N_w}}$.

By analogy with solid state lasers, this undulator radiation is referred to as the FEL spontaneous emission, at the resonance wavelength λ_r. The lasing, or field amplification, can be investigated by considering the self-consistent effects of the field on an electron beam.

FEL Electron Bunching

When an electron beam copropagates an undulator with a radiation field, either the spontaneous radiation or an externally injected seed, the electrons will exchange energy with the field, due to the transverse oscillation provided by the undulator.

To describe an electron's energy exchange with an electromagnetic field, once again one can look at the Lorentz force equation (2.3), this time neglecting the magnetic field and considering only the electric field vector, so

$$\mathbf{F} = \frac{d}{dt}(\gamma m \mathbf{v}) = -\left|e\right| \mathbf{E} \tag{2.11}$$

and multiplying both sides by $\mathbf{v}$ gives

$$\mathbf{v} \cdot \frac{d}{dt}(\gamma m \mathbf{v}) = -\left|e\right| \mathbf{v} \cdot \mathbf{E} \tag{2.12}$$

$$\frac{d\gamma}{dt}\mathbf{v} \cdot \mathbf{v} + \gamma \frac{d\mathbf{v}}{dt} \cdot \mathbf{v} = -\frac{|e|}{m}\mathbf{v} \cdot \mathbf{E} \tag{2.13}$$

$$\left(\frac{d\gamma}{dt}\mathbf{v} \cdot \mathbf{v} + \frac{\gamma}{2}\frac{d\mathbf{v}^2}{dt}\right) = -\frac{|e|}{m}\mathbf{v} \cdot \mathbf{E} \tag{2.14}$$

The term on the LHS can be replaced by rearranging the definition of the relativistic factor γ to obtain

$$\gamma = \sqrt{1 + \gamma^2\beta^2}, \tag{2.15}$$

and differentiating this with respect to t, to find

$$\frac{d\gamma}{dt}\mathbf{v} \cdot \mathbf{v} + \frac{\gamma}{2}\frac{d\mathbf{v}^2}{dt} = \frac{d\gamma}{dt}c^2 \tag{2.16}$$

so

$$\frac{d\gamma}{dt} = -\frac{|e|}{mc^2}\mathbf{v} \cdot \mathbf{E} \tag{2.17}$$

For a planar wiggler, ignoring the field in the y and z directions, this becomes

$$\frac{d\gamma}{dz} = -\frac{|e|}{mc^2}\beta_x E_x \tag{2.18}$$

and the electron speed in x is calculated in equation (2.6), so

$$\beta_x = \frac{|e|\, B_w}{\gamma m c k_w}\cos(k_w z) \tag{2.19}$$

The radiation field takes the form

$$\mathbf{E} = \hat{\mathbf{x}}|\xi_0|\cos(kz - \omega t + \phi), \tag{2.20}$$

where $|\xi_0|$ and ϕ are the magnitude and phase of the slowly varying complex field envelope ξ_0, and k and ω are the radiation wavenumber and angular frequency respectively. So from equation (2.18)

$$\frac{d\gamma}{dz} \propto -\frac{a_w|\xi_0|}{\gamma}\cos(k_w z)\cos(kz - \omega t + \phi) \tag{2.21}$$

$$\Rightarrow \frac{d\gamma}{dz} \propto -\frac{a_w|\xi_0|}{\gamma}(\cos((k - k_w)z - \omega t + \phi) + \cos((k + k_w)z - \omega t + \phi)) \tag{2.22}$$

The term on the left of equation (2.18) has a phase velocity $> c$, but the term on the right leads to the condition for resonance. It shows how the electron energy change varies with respect to the phase of the electron in the combined "ponderomotive" undulator plus radiation field, defined as

$$\theta = (k + k_w)z + \omega t + \phi \tag{2.23}$$

The resonant FEL wavelength is that which allows a continuous energy exchange between the radiation and electrons i.e. when

$$\frac{d\theta}{dz} = 0 \tag{2.24}$$

which is equivalent to equation (2.10), for the resonant FEL wavelength.

In a planar undulator, the unaveraged electron velocity in the z direction, β_z, oscillates at twice the frequency of the oscillation in x, which is why the averaged velocity $\bar{\beta}_z$ is used to define the resonance condition. It is constant in a helical undulator, and in that case $\beta_z = \bar{\beta}_z$. In the planar undulator, the so-called "jitter" motion in the longitudinal axis causes a coupling not just to the fundamental resonant frequency, but also its higher, odd on-axis harmonics. In the helical undulator, there are no higher harmonics observed, since there is no jitter motion.

To find $\bar{\beta}_z$ as an expression of the undulator parameters, and thus to define the resonance condition in terms of the undulator, one simply rearranges the definition of γ so that

$$\beta_z^2 = 1 - \beta_\perp^2 - \frac{1}{\gamma^2} \tag{2.25}$$

where $\beta_\perp^2 = \beta_x^2 + \beta_y^2$ which will be constant for a helical undulator. In the planar undulator expression (2.19) holds, so

$$\beta_z^2 = 1 - \frac{a_w^2}{\gamma^2}\cos^2(k_w z) - \frac{1}{\gamma^2} \tag{2.26}$$

$$\Rightarrow \bar{\beta}_z = \sqrt{1 - \frac{1}{\gamma^2}\left(\frac{a_w^2}{2} + 1\right)}. \tag{2.27}$$

By inserting this into equation (2.10), one obtains

$$\lambda_r = \lambda_w \left(\left(1 - \frac{1}{\gamma^2}\left(\frac{a_w^2}{2} + 1\right)\right)^{-1/2} - 1 \right). \tag{2.28}$$

The term on the left in the bracket can be expanded using the Binomial expansion,

$$\left(1 - \frac{1}{\gamma^2}\left(\frac{a_w^2}{2} + 1\right)\right)^{-1/2} \tag{2.29}$$

$$\approx 1 + \frac{1}{2\gamma^2}\left(\frac{a_w^2}{2} + 1\right) - \frac{3}{8\gamma^4}\left(\frac{a_w^2}{2} + 1\right)^2 ... \tag{2.30}$$

and dropping all terms after second, since typically $\gamma \approx 1000$, then equation (2.28) becomes

$$\lambda_r = \frac{\lambda_w}{2\gamma^2}\left(\frac{a_w^2}{2} + 1\right). \tag{2.31}$$

One more modification is made to (2.31) to generalise further. The $\frac{a_w^2}{2}$ term uses the peak magnetic undulator field. In the resonance expression for a helical undulator this a_w term is not halved, since then the electron oscillates in both x and y and

$$\beta_\perp = \frac{a_w}{\gamma}(\cos(k_w z)\hat{\mathbf{x}} - \sin(k_w z)\hat{\mathbf{y}}), \tag{2.32}$$

Working through the same steps from equation (2.26), the averaging over the square of both oscillatory terms will result in

$$\lambda_r = \frac{\lambda_w}{2\gamma^2}\left(a_w^2 + 1\right). \tag{2.33}$$

for the helical wiggler. If an rms undulator parameter is then defined such that

$$\bar{a}_w = \frac{eB_{rms}}{mck_w}, \tag{2.34}$$

then, for a planar undulator, $a_w^2 = 2\bar{a}_w^2$, so the resonant wavelength is

$$\lambda_r = \frac{\lambda_w}{2\gamma^2}\left(1 + \bar{a}_w^2\right), \tag{2.35}$$

which holds for both helical and planar undulators. Rearranging (2.35) to define the resonant energy, gives

$$\gamma_r = \sqrt{\frac{\lambda_w}{\lambda_r}\left(1 + \bar{a}_w^2\right)}. \tag{2.36}$$

Electrons at the resonant energy will remain at the same phase in the ponderomotive field over many undulator periods, and so from equation (2.22), the radiation field will modify the electron energy. Initially, assuming a cold electron beam (so all electrons have energy γ_r), the electrons will be spread evenly in phase, see figure 2.4, and just as many electrons will gain energy as will lose energy. The resulting energy modulation in the electron beam will result in a physical bunching in phase space, and the bunching causes the electrons to amplify the field coherently, which is the FEL lasing process.

2.1.2 Field Evolution And Approximations

Now, to complete the description of the FEL, the equation describing the field evolution is derived. A more rigorous derivation is given in e.g. [27]: the purpose of this rough derivation is to highlight the approximation or averaging of the equation, as it is a relevant distinction from the 3D model derived in chapter 3 of this thesis.

The field evolution from a moving charged body, in 2 dimensions (direction of propagation z and time t), ignoring the field diffraction and space charge, can be described by Maxwell's wave equation in the 1D approximation:

$$\left(\frac{\partial^2}{\partial z^2} - \frac{1}{c^2}\frac{\partial^2}{\partial t^2}\right)\mathbf{E} = \mu_0\frac{\partial \mathbf{J}}{\partial t} \tag{2.37}$$

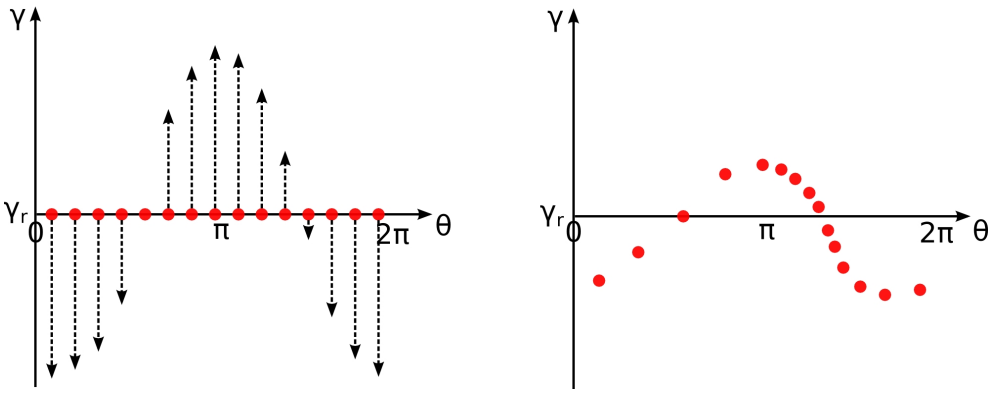

Figure 2.4: Figure showing the effects of the energy change upon position in the ponderomotive phase. The change in energy is constant over many undulator periods, see equation (2.22). For an electron beam with electrons evenly distributed in phase, the energy change is indicated by the dashed arrows in the plot on the left. Electrons which gain energy will travel faster and catch up with those electrons which lose energy. The second plot shows the electron bunching resulting from the energy modulation.

where $\mathbf{J}$ is the current density. If the field is assumed to be composed of a fast oscillatory term with wavenumber $k = \dfrac{2\pi}{\lambda} = \dfrac{\omega}{c}$ and a slowly varying complex envelope, so that

$$\mathbf{E} = \frac{1}{\sqrt{2}}(\hat{\mathbf{e}}\xi_0 e^{i(kz-\omega t)} + c.c.) \tag{2.38}$$

where $\hat{\mathbf{e}} = \dfrac{1}{\sqrt{2}}(\hat{\mathbf{x}} + i\hat{\mathbf{y}})$, then projecting the field equation over $\hat{\mathbf{e}}^*$ gives

$$\left(\frac{\partial^2}{\partial z^2} - \frac{1}{c^2}\frac{\partial^2}{\partial t^2}\right)\xi_0 e^{i(kz-\omega t)} = \mu_0 \frac{\partial J_\perp}{\partial t} \tag{2.39}$$

The transverse current density $J_\perp = \mathbf{J}\cdot\hat{\mathbf{e}}^* = J_x - iJ_y$ is then

$$J_\perp = -e\sum_{j=1}^{N} v_{\perp j}\delta(z - z_j) \tag{2.40}$$

where the sum is over all electrons, $v_\perp = v_x - iv_y$ is the (complex) transverse velocity and $\delta(x)$ is the delta function.

Typically, in most FEL analysis and codes, the Slowly Varying Envelope Approximation (SVEA) is applied, which states that the complex radiation envelope

varies slowly with respect to a radiation wavelength in both time and space. Thus one can state that

$$\left|\frac{\partial \xi_0}{\partial z}\right| \ll |k\xi_0|\,, \left|\frac{\partial \xi_0}{\partial t}\right| \ll |\omega \xi_0| \tag{2.41}$$

and so second order derivatives in both z and t can be dropped. The LHS of equation (2.39) then becomes

$$\left(\frac{\partial \xi_0}{\partial z} + \frac{1}{c}\frac{\partial \xi_0}{\partial t}\right) e^{i(kz-\omega t)} \tag{2.42}$$

The equation is then averaged over a length $l_{||}$ equal to at least one resonant radiation wavelength λ_r, and the field envelope cannot now be driven below the scale of a wavelength. $v_\perp$ can be calculated from the corresponding undulator type (planar or helical), giving, in the case of the helical undulator, ignoring the radiation field contribution to $v_\perp$,

$$\left(\frac{\partial \xi_0}{\partial z} + \frac{1}{c}\frac{\partial \xi_0}{\partial t}\right) \propto \frac{1}{l_{||}} \sum_{j=1}^{N} e^{-i((k_w+k)z+\omega t)} \tag{2.43}$$

$$\left(\frac{\partial \xi_0}{\partial z} + \frac{1}{c}\frac{\partial \xi_0}{\partial t}\right) \propto \frac{1}{l_{||}} \sum_{j=1}^{N} e^{-i\theta_j} \tag{2.44}$$

where the ponderomotive phase of the j^{th} electron, θ_j, was defined earlier in equation (2.23). The sum is now over the N electrons in a localised volume of the electron pulse $l_{||}$, commonly refered to as an electron slice, and the bunching parameter

$$b = \frac{1}{N} \sum_{j=1}^{N} e^{-i\theta_j} \tag{2.45}$$

is defined, so that

$$\left(\frac{\partial \xi_0}{\partial z} + \frac{1}{c}\frac{\partial \xi_0}{\partial t}\right) \propto b \tag{2.46}$$

If the electrons are evenly distributed in the ponderomotive phase, then the bunching term $b = 0$ and there is no net gain to the field. Note that if a planar

wiggler is used, average quantities of θ_j and β_j must be used due to the jitter motion. They are averaged over a wiggler period in z, and the averaging introduces a difference of Bessel functions into the equations to account for the decoupling to the field resulting from the jitter motion.

The universally scaled FEL equations are derived in this manner. The equations describing the energy and position in ponderomotive phase of the electrons are derived from the Lorentz equation, and describe the evolution of the dynamics within a cyclic phase space. New dimensionless scaled variables are defined, which allows the description of the system to become simpler and allows interesting insight into many facets of FEL operation. The variables are defined with respect to the FEL or Pierce parameter ρ [28], given by

$$\rho = \frac{1}{\gamma_r}\left(\frac{\bar{a}_w \omega_p}{4ck_w}\right)^{2/3} \tag{2.47}$$

The "steady state" FEL equations (ignoring $\frac{\partial}{\partial t}$), derived in [27] from equations (2.3) and (2.37), for a helical wiggler and valid for an infinitely long electron beam, so that the slippage of the field over the electrons is neglected, are

$$\frac{d\theta_j}{d\bar{z}} = p_j \tag{2.48}$$

$$\frac{dp_j}{d\bar{z}} = -(Ae^{i\theta_j} + A^* e^{-i\theta_j}) \tag{2.49}$$

$$\frac{dA}{d\bar{z}} = < e^{-i\theta} > \tag{2.50}$$

where A is the scaled complex field envelope, which is scaled so the maximum intensity $|A|^2 \approx 1$ at saturation, θ_j is the phase of the jth electron in the combined (wiggler and radiation) ponderomotive field, p_j is the scaled energy of the jth electron, scaled so that when $p = 0$ the resonant condition is fulfilled, and $\bar{z}$ is the scaled longitudinal distance into the wiggler. $\bar{z}$ is scaled with respect to what is referred to as the FEL gain length $l_g = \lambda_w/4\pi\rho$. As shown in the next section, the FEL gives exponential gain during a gain length in what is known as the high gain regime.

Equation (2.50), the steady state equation for the evolution of the scaled complex envelope, describe how the electron bunching can drive the FEL interaction.

This can be made clearer by splitting the scaled envelope into its magnitude $|A|$ and phase ψ such that $A = |A|\, e^{i\psi}$, so that equation (2.50) becomes

$$\frac{d}{d\bar{z}}(|A|\, e^{i\psi}) =< e^{-i\theta} > \tag{2.51}$$

$$e^{i\psi}\left(\frac{d\,|A|}{d\bar{z}} + i\,|A|\,\frac{d\psi}{d\bar{z}}\right) =< e^{-i\theta} > \tag{2.52}$$

$$\frac{d\,|A|}{d\bar{z}} + i\,|A|\,\frac{d\psi}{d\bar{z}} =< e^{-i(\theta+\psi)} > \tag{2.53}$$

and the real and imaginary parts of both sides can be equated to conveniently give the rate of change of the amplitude and phase of the field as

$$\frac{d\,|A|}{d\bar{z}} =< \cos(\theta+\psi) > \tag{2.54}$$

$$\frac{d\psi}{d\bar{z}} = -\frac{1}{|A|} < \sin(\theta+\psi) > \tag{2.55}$$

Initially, when the electrons enter the undulator they will be distributed evenly in phase, and, as explained in the previous section, and seen here in equation (2.54), will give no overall gain to the field. From equation (2.22) and figure 2.4, which showed how the electrons bunch in a resonant interaction over many undulator periods, one can infer that that the electrons will bunch at $\theta = \dfrac{3\pi}{2}$, which, from equation (2.54), is a point in phase corresponding to zero amplification, but positive phase growth in equation (2.55). The phase changes the condition necessary for amplification in (2.54), and the bunching begins to amplify the field. The stronger field then bunches the electrons more tightly, which in turn drives the phase and magnitude of the field in a positive feedback loop.

This is the onset of an instability which gives rise to an exponential amplification of the field, and is now explored through a linear analysis of equations (2.48)-(2.50).

2.2 Linear Analysis

The system is manipulated by examining around the initial values i.e. at a small pertubation from the initial state. So in general, if f is a function of x,

$$f(x) = f_0 + f_1(x) \tag{2.56}$$

where f_0 is the initial value of the system, and $f_1(x) \ll 1$ is the small pertubation.

Initial values of the scaled field envelope, electron energy and phase are:

$$A(\bar{z}) = A_0 \tag{2.57}$$

$$p_j(\bar{z}) = p_{0j} = \delta \tag{2.58}$$

$$\theta_j(\bar{z}) = \theta_{0j} + \delta\bar{z} \tag{2.59}$$

where δ is the initial detuning on the electron energy. If $\delta = 0$ then the electrons are injected at the resonant energy.

Throughout the linear analysis dot notation is used when convenient to signify the derivative with respect to $\bar{z}$ i.e. for variable x

$$\dot{x} = \frac{dx}{d\bar{z}} \tag{2.60}$$

2.2.1 Linearization of 1D FEL equations

Here the 1D FEL equations (2.48)-(2.50) are linearized using the notation above to give three linear coupled differential equations.

Linearization of $\dot{A}$

Looking at equation (2.50) and using condition (2.59) and pertubation (2.56),

$$\dot{A} =< e^{-i(\theta_0+\delta\bar{z}+\theta_1)} > \tag{2.61}$$

The small pertubation on the phase has been defined as $|\theta_1| \ll 1$, and $e^x \approx 1 + x$ when $x \ll 1$, so

$$\dot{A} =< e^{-i(\theta_0+\delta\bar{z})}(1 - i\theta_1) > \tag{2.62}$$

$$\dot{A} =< e^{-i(\theta_0+\delta\bar{z})} > - < i\theta_1 e^{-i(\theta_0+\delta\bar{z})} > \tag{2.63}$$

It is assumed that $< e^{-i(\theta_0+\delta\bar{z})} >= e^{-i\delta\bar{z}} < e^{-i\theta_0} >= 0$, as the electrons are assumed distributed uniformly in phase between $(0 : 2\pi]$.

$$\dot{A} =- < i\theta_1 e^{-i(\theta_0+\delta\bar{z})} > \tag{2.64}$$

$$\dot{A} =b \tag{2.65}$$

where

$$b = - < i\theta_1 e^{-i(\theta_0+\delta\bar{z})} > \tag{2.66}$$

Linearization of $\dot{p_j}$

Now taking equation (2.49), and again linearizing around initial conditions

$$\dot{p_j} = -(Ae^{i(\theta_{0j}+\delta\bar{z})}(1 + i\theta_{1j}) + A^* e^{-i(\theta_{0j}+\delta\bar{z})}(1 - i\theta_{1j})) \tag{2.67}$$

As A and $|\theta_{1j}| \ll 1$, 2^{nd} order terms can be ignored. Multiplying throughout by $e^{-i(\theta_{0j}+\delta\bar{z})}$, and remembering $p_j = \delta + p_{1j}$ and δ is a constant,

$$e^{-i(\theta_{0j}+\delta\bar{z})}\dot{p_{1j}} = -(A + A^* e^{-2i(\theta_{0j}+\delta\bar{z})}) \tag{2.68}$$

Averaging gives

$$< e^{-i(\theta_0+\delta\bar{z})}\dot{p_1} >=- < A > - < A^* e^{-2i(\theta_0+\delta\bar{z})} > \tag{2.69}$$

$$e^{-i\delta\bar{z}} < e^{-i\theta_0}\dot{p_1} >=- < A > -A^* e^{-2i\delta\bar{z}} < e^{-2i\theta_0} > \tag{2.70}$$

$$e^{-i\delta\bar{z}} < e^{-i\theta_0}\dot{p_1} >=- < A > \tag{2.71}$$

Now, defining a new variable P as

$$P =< p_1 e^{-i(\theta_0+\delta\bar{z})} > \tag{2.72}$$

Differentiating then rearranging gives

$$\dot{P} = < \dot{p_1} e^{-i(\theta_0+\delta\bar{z})} > - < i\delta p_1 e^{-i(\theta_0+\delta\bar{z})} > \tag{2.73}$$

$$\dot{P} =e^{-i\delta\bar{z}} < e^{-i\theta_0}\dot{p_1} > -i\delta P \tag{2.74}$$

$$e^{-i\delta\bar{z}} < e^{-i\theta_0}\dot{p_1} >=\dot{P} + i\delta P \tag{2.75}$$

Substituting (2.75) into (2.71) gives the linearized equation for the electron energy

$$\dot{P} + i\delta P = - < A > \tag{2.76}$$

$$\dot{P} = - A - i\delta P \tag{2.77}$$

Linearization of $\dot{\theta_j}$

Taking equation (2.48), and linearizing around initial conditions gives

$$\frac{d}{d\bar{z}}(\theta_{0j} + \theta_{1j} + \delta\bar{z}) = p_{1j} + \delta \tag{2.78}$$

$$\dot{\theta_{1j}} + \delta = p_{1j} + \delta \tag{2.79}$$

$$\dot{\theta_{1j}} = p_{1j} \tag{2.80}$$

Multiplying through by $ie^{-i(\theta_{0j}+\delta\bar{z})}$ and averaging,

$$< \dot{\theta_1} i e^{-i(\theta_{0j}+\delta\bar{z})} > = < p_1 i e^{-i(\theta_{0j}+\delta\bar{z})} > \tag{2.81}$$

Differentiating equation (2.66)

$$\dot{b} = - < i\dot{\theta_1} e^{-i(\theta_0+\delta\bar{z})} > - < \delta\theta_1 e^{-i(\theta_0+\delta\bar{z})} > \tag{2.82}$$

$$\dot{b} = - < i\dot{\theta_1} e^{-i(\theta_0+\delta\bar{z})} > - i\delta b \tag{2.83}$$

$$< i\dot{\theta_1} e^{-i(\theta_0+\delta\bar{z})} > = - \dot{b} - i\delta b \tag{2.84}$$

Substituting (2.84) and (2.72) into (2.81) gives the linearized equation of the electron bunching

$$-\dot{b} - i\delta b = iP \tag{2.85}$$

$$\dot{b} = - iP - i\delta b \tag{2.86}$$

Final Form of Linearised Equations

The 3 coupled linear differential equations are now

$$\dot{b} = - iP - i\delta b \tag{2.87}$$

$$\dot{P} = - A - i\delta P \tag{2.88}$$

$$\dot{A} = b \tag{2.89}$$

where $b = - < i\theta_1 e^{-i(\theta_0+\delta\bar{z})} >$ and $P =< p_1 e^{-i(\theta_0+\delta\bar{z})} >$ measure the electron bunching at different points in phase space.

2.2.2 Linear Analysis

Laplace Transforms of Linearized Equations

The coupled linear differential equations (2.87)-(2.89) can be solved using Laplace transforms. The Laplace transform L from $x \to s$ of the differential of a function $f(x)$ is

$$L_{x\to s}\frac{df(x)}{dx} = s\acute{f}(s) - f(x_0) \tag{2.90}$$

Performing the Laplace transform from $\bar{z} \to s$ on equations (2.87)-(2.89) one obtains

$$s\acute{b} = -i\acute{P} - i\delta\acute{b} + b_0 \tag{2.91}$$

$$s\acute{P} = -\acute{A} - i\delta\acute{P} + P_0 \tag{2.92}$$

$$s\acute{A} = \acute{b} + A_0 \tag{2.93}$$

Rearranging (2.92) for $\acute{P}$ and substituting into (2.91), then rearranging for $\acute{b}$ and substituting into (2.93),

$$s\acute{A} - \frac{i\acute{A}}{(s+i\delta)^2} = \frac{b_0}{s+i\delta} - \frac{iP_0}{(s+i\delta)^2} + A_0 \tag{2.94}$$

Putting the RHS all over a common denominator and expressing in terms of $\acute{A}$ gives

$$\acute{A} = \frac{(s+i\delta)^2 A_0 + (s+i\delta)b_0 - iP_0}{s^3 + 2i\delta s^2 - s\delta^2 - i} \tag{2.95}$$

Then the following 2 substitutions are performed:

$$s = q - i\delta \tag{2.96}$$

$$q = ip \tag{2.97}$$

So the equation becomes

$$\acute{A} = \frac{-iP_0 + b_0 ip - A_0 p^2}{-ip^3 + i\delta p^2 - i} \tag{2.98}$$

$$\acute{A} = \frac{P_0 - pb_0 - ip^2 A_0}{p^3 - \delta p^2 + 1} \tag{2.99}$$

A solution for A may be obtained through the inverse Laplace transform. If

$$\acute{A} = f(s) \tag{2.100}$$

then the inverse Laplace transform is

$$A = \frac{1}{2\pi i} \int_{\gamma - i\infty}^{\gamma + i\infty} e^{s\bar{z}} f(s) ds \tag{2.101}$$

Performing the substitutions from $s \to p$, $ds = dq = idp$ and $e^{s\bar{z}} = e^{(q-i\delta)\bar{z}} = e^{i\bar{z}(p-\delta)}$, and the limits change from $s = \gamma - i\infty$ and $s = \gamma + i\infty$ to $p = i\gamma - \infty$ and $p = i\gamma + \infty$. Hence equation (2.101) becomes

$$A = \frac{1}{2\pi i} \int_{i\gamma - \infty}^{i\gamma + \infty} ie^{iz(p-\delta)} f(p) dp \tag{2.102}$$

$$A = \frac{1}{2\pi i} \int_{i\gamma - \infty}^{i\gamma + \infty} ie^{iz(p-\delta)} \frac{P_0 - pb_0 - ip^2 A_0}{p^3 - \delta p^2 + 1} dp \tag{2.103}$$

Integration Method

The integral in equation (2.103) can be solved using residue integration. If

$$f(\bar{z}) = \frac{p(\bar{z})}{q(\bar{z})} \tag{2.104}$$

then a pole is found at the points where $q(\bar{z}) = 0$. The residue $a_{\bar{z}_0}$ of a pole $\bar{z}_0$ of $f(\bar{z})$ is given by

$$\lim_{\bar{z} \to \bar{z}_0} [(\bar{z} - \bar{z}_0) f(\bar{z})] \tag{2.105}$$

For an integral

$$I = \oint f(\bar{z}) d\bar{z}, \tag{2.106}$$

where, again

$$f(\bar{z}) = \frac{p(\bar{z})}{q(\bar{z})}, \tag{2.107}$$

the integral is given by $2\pi i \times$ sum of the residues $a_{\bar{z}_0}$ at the poles contained within the circular path of integration.

Looking at the integral in equation (2.101),

$$I = \int_{\gamma - i\infty}^{\gamma + i\infty} e^{s\bar{z}} f(s) ds \tag{2.108}$$

Choosing a value of γ so that the line $s = \gamma$ is to the right of all the poles of $f(s)$, a circular path of integration can be created by drawing a semi-circle from $s = \gamma - i\infty$ to $s = \gamma + i\infty$, as in figure 2.5(a).

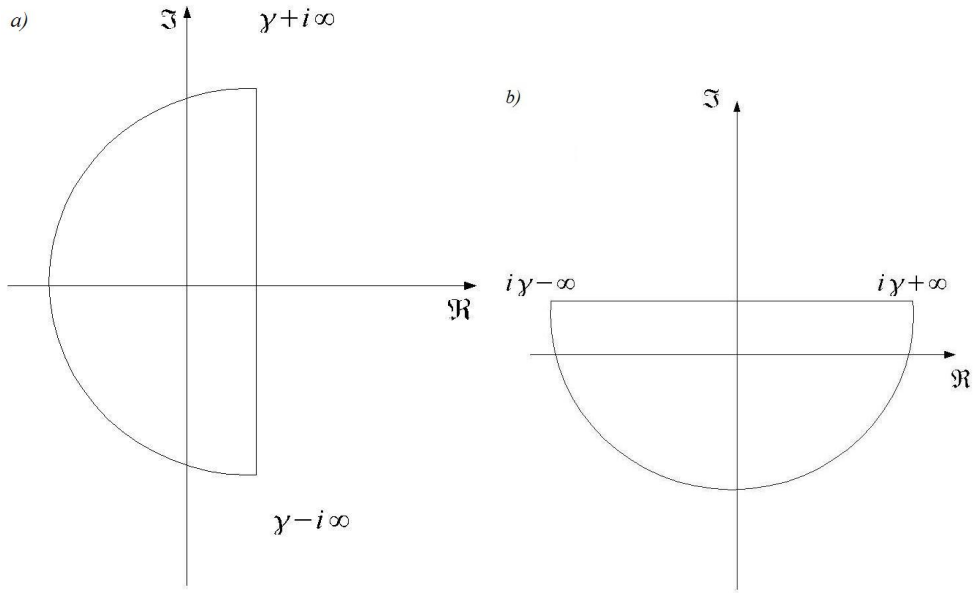

Figure 2.5: Diagram showing the creation of the closed integration paths for integrating(a) eq. (2.108) and (b) eq. (2.110)

It can thus be shown that

$$\int_{\gamma - i\infty}^{\gamma + i\infty} e^{s\bar{z}} f(s) ds = \oint e^{s\bar{z}} f(s) ds \tag{2.109}$$

where the circular integration path encloses all the poles of $f(\bar{z})$. After applying the transformation from $s \to p$, the limits of integration change and there is a shift in the complex plane over the region of integration. However, the principle is just the same, creating a closed integration path as illustrated in fig. 2.5(b).

The solution for A becomes eq. (2.102), which, applying the residue integration theorem, becomes

$$A = \frac{1}{2\pi i} \int_{i\gamma-\infty}^{i\gamma+\infty} ie^{i\bar{z}(p-\delta)} f(p) dp \tag{2.110}$$

$$A = \frac{1}{2\pi i} \times 2\pi i \sum Res[ie^{i\bar{z}(p-\delta)} f(p)] \tag{2.111}$$

$$A = \sum Res[ie^{i\bar{z}(p-\delta)} f(p)] \tag{2.112}$$

So to solve eq. (2.112), the poles and their associated residues must be found. Looking at equation (2.103), the poles will be found when

$$p^3 - \delta p^2 + 1 = 0 \tag{2.113}$$

Solution when $\delta = 0$

If $\delta = 0$ then the electrons are injected into the wiggler at the resonant energy γ_r defined in equation (2.36) i.e. the initial average electron energy is such that the electron phase remains constant with respect to the ponderomotive field. Therefore, as illustrated in figure 2.4, half the electrons will gain energy and half will lose energy, so there is no net gain in the system at first. However as $\bar{z}$ increases, as explained in section 2.1.2, the energy differences imposed by the field on the electrons will cause the electrons to start bunching on the scale of a radiation wavelength, driving the radiation phase (according to equation 2.55), in turn driving the magnitude of the field according to equation (2.54). The area where the electrons provide exponential gain to the field is known as the high gain regime.

When $\delta = 0$, then

$$A = \frac{1}{2\pi i} \int_{i\gamma-\infty}^{i\gamma+\infty} ie^{i\bar{z}p} \frac{P_0 - pb_0 - ip^2 A_0}{p^3 + 1} dp \tag{2.114}$$

and the poles occur when

$$p^3 + 1 = 0 \tag{2.115}$$

So poles are

$$p_1 = -1 \tag{2.116}$$

$$p_2 = \frac{1}{2} + \frac{\sqrt{3}}{2} \tag{2.117}$$

$$p_3 = \frac{1}{2} - \frac{\sqrt{3}}{2} \tag{2.118}$$

Using equation (2.105), the residue a_{p_1} where $p = -1$

$$a_{p_1} = \lim_{p \to -1} \left[(p+1) i e^{i\bar{z}p} \frac{P_0 - b_0 p - A_0 i p^2}{(p+1)(p - (\frac{1}{2} + \frac{\sqrt{3}}{2}i)(p - (\frac{1}{2} - \frac{\sqrt{3}}{2}i)} \right] \tag{2.119}$$

$$a_{p_1} = \frac{i}{3} e^{-i\bar{z}} (P_0 + b_0 - i A_0) \tag{2.120}$$

Residue a_{p_2} at $p = \frac{1}{2} + \frac{\sqrt{3}}{2}i$

$$a_{p_2} = \lim_{p \to \frac{1}{2} + \frac{\sqrt{3}}{2}i} \left[(p - (\frac{1}{2} + \frac{\sqrt{3}}{2}i)) i e^{i\bar{z}p} \frac{P_0 - b_0 p - A_0 i p^2}{(p+1)(p - (\frac{1}{2} + \frac{\sqrt{3}}{2}i)(p - (\frac{1}{2} - \frac{\sqrt{3}}{2}i)} \right] \tag{2.121}$$

$$a_{p_2} = \frac{-i e^{-\frac{\bar{z}}{2}(\sqrt{3} - i)} (2P_0 - (1 + \sqrt{3}i) b_0 + (\sqrt{3} + i) A_0)}{3(1 - \sqrt{3}i)} \tag{2.122}$$

Residue a_{p_3} at $p = \frac{1}{2} - \frac{\sqrt{3}}{2}i$

$$a_{p_3} = \lim_{p \to \frac{1}{2} + \frac{\sqrt{3}}{2}i} \left[(p - (\frac{1}{2} + \frac{\sqrt{3}}{2}i)) i e^{i\bar{z}p} \frac{P_0 - b_0 p - A_0 i p^2}{(p+1)(p - (\frac{1}{2} + \frac{\sqrt{3}}{2}i)(p - (\frac{1}{2} - \frac{\sqrt{3}}{2}i)} \right] \tag{2.123}$$

$$a_{p_3} = \frac{-i e^{\frac{\bar{z}}{2}(\sqrt{3} + i)} (2P_0 - (1 - \sqrt{3}i) b_0 + (-\sqrt{3} + i) A_0)}{3(1 + \sqrt{3}i)} \tag{2.124}$$

Adding the residues together gives

$$A = Be^{-i\bar{z}} + Ce^{\frac{-\bar{z}}{2}(\sqrt{3}-i)} + De^{\frac{\bar{z}}{2}(\sqrt{3}+i)} \tag{2.125}$$

where

$$B = \frac{i}{3}(P_0 + b_0 - iA_0) \tag{2.126}$$

$$C = \frac{-i(2P_0 - (1+\sqrt{3}i)b_0 + (\sqrt{3}+i)A_0)}{3(1-\sqrt{3}i)} \tag{2.127}$$

$$D = \frac{-i(2P_0 - (1-\sqrt{3}i)b_0 + (-\sqrt{3}+i)A_0)}{3(1+\sqrt{3}i)} \tag{2.128}$$

Looking at (2.125), there is an exponentially increasing, exponentially decreasing and oscillatory term in the equation.

To further examine the behaviour of the system when $\delta = 0$, how the system depends on each parameter is examined. The equations are simplified by writing them in terms of the roots, defined in equations (2.116) - (2.118). The complex denominator in C and D is removed by multiplying the top and bottom of each by their complex conjugate. Re-expressing in this way one obtains

$$B = -\frac{i}{3}(p_1P_0 + p_1b_0 + iA_0) \tag{2.129}$$

$$C = -\frac{i}{3}(p_2P_0 + p_3b_0 + iA_0) \tag{2.130}$$

$$D = -\frac{i}{3}(p_3P_0 + p_2b_0 + iA_0) \tag{2.131}$$

and

$$B^* = \frac{i}{3}(p_1P_0 + p_1b_0 - iA_0) \tag{2.132}$$

$$C^* = \frac{i}{3}(p_3P_0 + p_2b_0 - iA_0) \tag{2.133}$$

$$D^* = \frac{i}{3}(p_2P_0 + p_3b_0 - iA_0) \tag{2.134}$$

When examining the system's dependance on the initial values, the other parameters are set = 0. So when varying P_0, $b_0 = 0$ and $A_0 = 0$, and so forth.

The behaviour we wish to examine is that of the scaled intensity $|A|^2$, so

$$\begin{aligned}|A|^2 = BB^*e^0 + CB^*e^{-\frac{\bar{z}}{2}(\sqrt{3}-3i)} + DB^*e^{\frac{\bar{z}}{2}(\sqrt{3}+3i)} \\ +BC^*e^{-\frac{\bar{z}}{2}(\sqrt{3}+3i)} + CC^*e^{-\sqrt{3}\bar{z}} + DC^*e^0 \\ +BD^*e^{\frac{\bar{z}}{2}(\sqrt{3}-3i)} + CD^*e^0 + DD^*e^{\sqrt{3}z}\end{aligned} \tag{2.135}$$

To examine the scaled intensity's dependance on the initial condition P_0 only, let $b_0 = 0$ and $A_0 = 0$, so intensity becomes

$$|A|^2 = \frac{P_0^2}{9}\left[e^{\sqrt{3}\bar{z}} + e^{-\sqrt{3}\bar{z}} - e^{\frac{\sqrt{3}\bar{z}}{2}}(\cos(\frac{3\bar{z}}{2}) + \sqrt{3}\sin(\frac{3\bar{z}}{2})) - e^{-\frac{\sqrt{3}\bar{z}}{2}}(\cos(\frac{3\bar{z}}{2}) - \sqrt{3}\sin(\frac{3\bar{z}}{2}))\right] \tag{2.136}$$

Similarly, showing the dependance on the initial bunching b_0 only (and thus letting $P_0 = 0$ and $A_0 = 0$),

$$|A|^2 = \frac{b_0^2}{9}\left[e^{\sqrt{3}\bar{z}} + e^{-\sqrt{3}\bar{z}} - e^{-\frac{\sqrt{3}\bar{z}}{2}}(\cos(\frac{3\bar{z}}{2}) + \sqrt{3}\sin(\frac{3\bar{z}}{2})) - e^{\frac{\sqrt{3}\bar{z}}{2}}(\cos(\frac{3\bar{z}}{2}) - \sqrt{3}\sin(\frac{3\bar{z}}{2}))\right] \tag{2.137}$$

And examining the dependance only on A_0

$$|A|^2 = \frac{A_0^2}{9}\left[3 + e^{\sqrt{3}\bar{z}} + e^{-\sqrt{3}\bar{z}} + 2e^{\frac{\sqrt{3}\bar{z}}{2}}\cos(\frac{3\bar{z}}{2}) + 2e^{\frac{-\sqrt{3}\bar{z}}{2}}\cos(\frac{3\bar{z}}{2})\right] \tag{2.138}$$

The computational maths program MATLAB was used to plot equations (2.136) - (2.138).

Looking at all three equations it is expected that at high values of $\bar{z}$, $|A|^2 \to e^{\sqrt{3}\bar{z}}$. This is the exponential instability of the FEL described physically in section 2.1.2, allowing it to amplify an initial field by several orders of magnitiude, in the high gain regime. Indeed, it is noted in figure 2.6 that the respective plots converge for $\bar{z} \geq 3$. Furthermore, the gradient of this line on the natural logarithm scale is $\sqrt{3}$, as expected from the equations.

On the plot examining equation (2.138), the initial value for the scaled intensity $|A|^2$, that is $|A(\bar{z}_0)|^2 = |A_0|^2$, corresponds to a small initial seed field which has been injected into the wiggler with the electrons. There is an interval in $\bar{z}$ in which $|A|^2 = |A_0|^2$, which will be identified in the next section as the low-gain

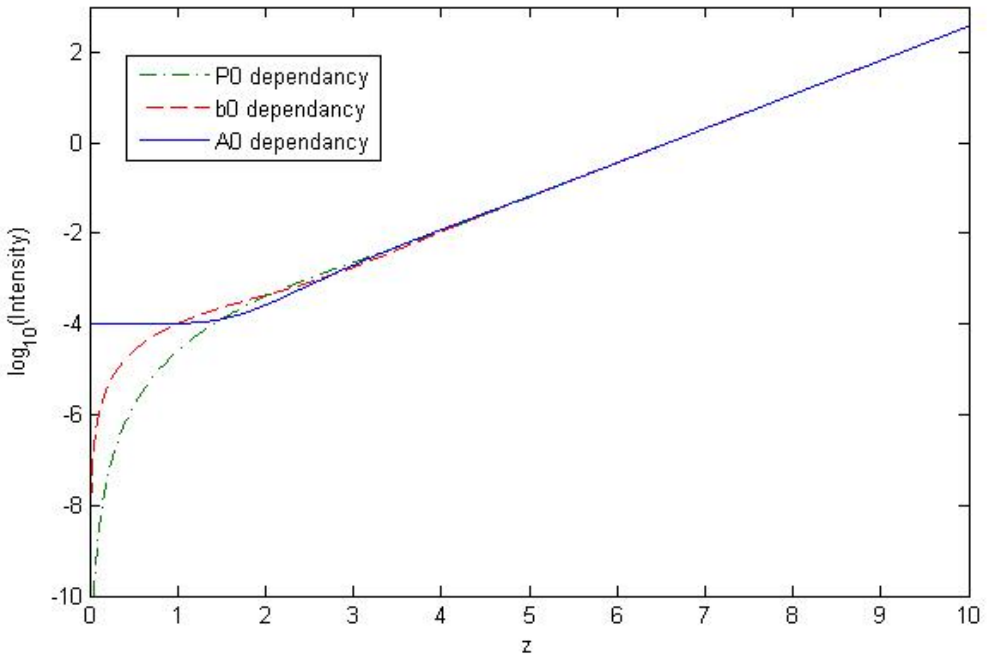

Figure 2.6: Graph of $\ln(|A|^2)$ vs $\bar{z}$ for $\delta = 0$ from $\bar{z} = 0 \rightarrow 10$, examining the dependancies outlined above. In each plot, the value of the dependant variable b_0, P_0 or $A_0 = 10^{-4}$

regime. As will be shown, there is no amplification present in the low gain regime for $\delta = 0$. The exponential or high gain regime begins at $\bar{z} \approx 2$, and it is clearly observed that the field intensity is experiencing exponential amplification with increasing $\bar{z}$.

In the plots of equations (2.136) and (2.137), the intensities begin at 0 as there is no seed field to amplify in these cases. In both these cases the electrons generate and subsequently amplify a field, due to the initial bunching in b_0 or P_0.

Solution when $\delta \neq 0$

MATLAB was used to find the poles of equation (2.103), and to calculate the residues at these poles for different values of δ. Shown below are plots of how the detuning affects the gain of the FEL for different values of $\bar{z}$, where the gain is

defined as

$$G = \frac{|A|^2 - |A_0|^2}{|A_0|^2} \tag{2.139}$$

Figure 2.7 *a*) is the well known Madey gain curve [27], at $\bar{z} = 0.5$ (low gain), with $b_0, P_0 = 0$, showing no gain if the electrons are injected at resonance. There is small positive gain if the electrons are injected with energy slightly above the resonant energy (positive detuning), and negative gain with an energy slightly below resonance (negative detuning). This occurs when the electrons bunch slightly but do not significantly drive the phase of the field. In that case, at zero-detuning, from equation (2.54), the electrons will only give positive amplification by bunching at $\theta = 0/2\pi$. Again, at zero-detuning, from equation (2.22), the electrons will bunch around $\theta = 3\pi/2$ and there will be no gain, as the radiation phase has not been driven. By giving the electrons a small energy kick, a small positive detuning, the electrons will bunch at $0/2\pi$ and the field envelope will be amplified. This low-gain regime is utilized in cavity FEL's, where the undulator is enclosed by mirrors, and the radiation is reflected back and forth to interact with a fresh beam of electrons on each pass, and the radiation builds up through many successive passes.

As $\bar{z}$ increases the system moves forward into the high gain regime (defined in the solution where $\delta = 0$), and a narrow peak emerges at $\delta = 0$, as the radiation phase is driven, described in equation (2.55). As $\bar{z}$ continues to increase the gain peak at $\delta = 0$ becomes larger and narrower, see figures 2.7 *b*) and *c*). Again, this was explained in section 2.1.2 as the bunching driving the phase of the radiation field, triggering a positive feedback loop which results in amplification at the resonant energy.

The initial bunching parameters b_0 and P_0 affect the results in different ways. They are a measure of the bunching around different points in the ponderomotive phase θ. Positive P_0 corresponds to the initial bunching around $\theta = 0/2\pi$, negative P_0 gives the bunching around $\theta = \pi$. Positive and negative b_0 give the initial bunching around $\theta = \frac{3\pi}{2}$ and $\frac{\pi}{2}$, respectively. In particular, if a seed field is present, a positive b_0 will drive the radiation phase much quicker (from equation

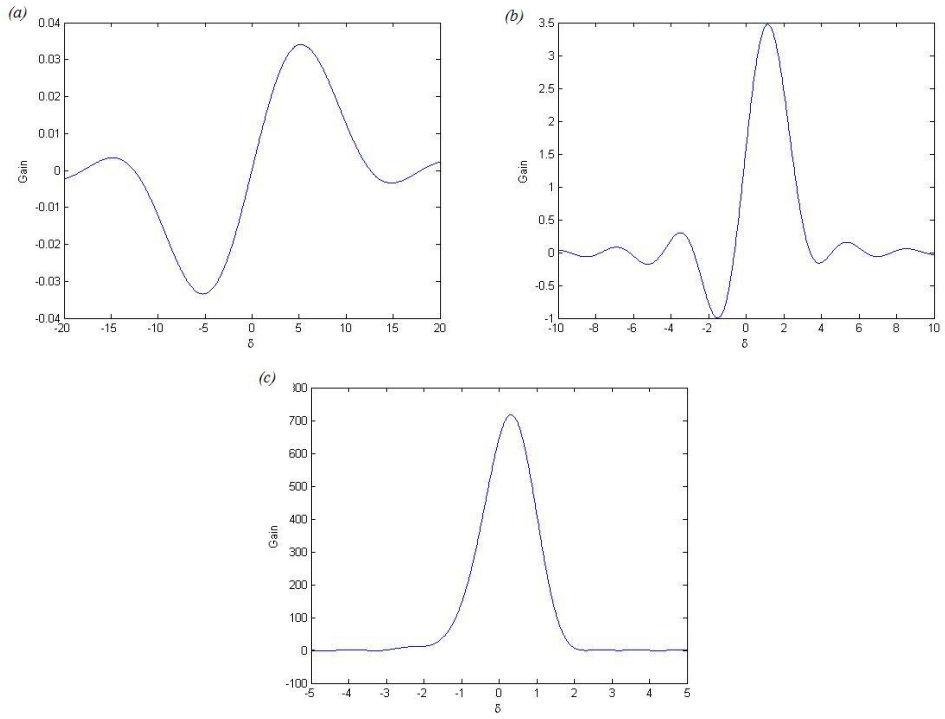

Figure 2.7: Plots showing how the gain curve changes as $\bar{z}$ increases for $|A_0| = 10^{-4}$ and $b_0, P_0 = 0$. In (a) $\bar{z} = 0.5$, (b) $\bar{z} = 2$ and (c) $\bar{z} = 5$.

(2.55)), leading to a quicker transition into the high gain regime.

The exponential amplification continues to saturation. Saturation occurs when the radiation field has extracted enough energy from the electron beam so that it is no longer resonant, and it begins to reabsorb the field energy. As the electrons gain energy they will become resonant again, and the intensity then becomes oscillatory. To try and hold off saturation and increase the efficiency of the interaction the undulator can be tapered [29]. Remembering that the equation for the resonant energy (2.36) shows that it varies with the undulator parameter $\bar{a}_w$, a tapered undulator is one which varies $\bar{a}_w$ to keep the electrons resonant as they lose energy.

2.3 Slippage and 3D Effects

The previous section illustrated mathematically the exponential instability in the FEL. According to the analysis, the process can startup from a small initial bunching in the beam. This is important since there are no seeds or appropriate mirrors available at short (hard X-ray) wavelengths, so it is not possible to use a low gain oscillator FEL. It was proposed in [28] that small random fluctations on the individual electron positions and energy inherent in the pulse will give a small random non-zero bunching from which the high gain FEL process can begin. This process is known as SASE (Self Amplified Spontaneous Emission). A single pass, high gain configuration is thus the method used to generate high power X-ray radiation from an FEL.

The analysis in the previous section was performed in the steady state, which, although it allows one to examine the FEL instability, does not take into account the slippage of the radiation field over the electron beam. Slippage is of fundamental importance in SASE. Taking into account an electron beam with a finite longitudinal length, the electron beam can be represented by many averaged longitudinal regions of equal length, called electron beam slices. Each slice possesses its own averaged bunching parameter, arising from the electrons contained within it. The electrons in each slice are contained in a cyclic phase space. Initially, different (averaged) regions of the electron beam will possess a different, small random bunching parameter as a result of the noise in the electron beam. The radiation generated in each of these sections will slip forward and be ampified as they slip over different regions upstream. The longitudinal pulse structure will therefore be largely uncorrelated, and as the radiation slips over the electron pulse different regions of amplified radiation will develop independently. An important concept here is the cooperation length, l_c defined as

$$l_c = \frac{\lambda_r}{4\pi\rho}, \tag{2.140}$$

which gives the relative slippage of the radiation through the electron beam in one gain length [30]. According to the analysis, each independent region evolves with separation $\approx 2\pi l_c$, within which a temporally coherent spike emerges. This

results in a radiation output with relatively poor temporal coherence but full transverse coherence, with large fluctations in the shot-to-shot output [31].

The FEL parameter ρ governs many of the effects and criteria necessary for successful operation. The electron beam energy spread σ_γ and the radiation bandwidth at saturation are both $\approx \rho$. The amplification will be significantly reduced if the initial beam energy spread $\sigma_\gamma \gtrsim \rho$. The saturation power is $\sim \rho P_e$, where P_e is the initial power of the electron pulse: so ρ is the efficiency of the FEL interaction, typically $10^{-2} \rightarrow 10^{-4}$.

Diffraction and electron beam emittance can also potentially spoil the interaction [32]. The field diffraction reduces the coupling with the electrons if the field diffracts significantly outside of the transverse beam area. Likewise, the electron beam transverse velocity spread will cause decoupling if the electron beam travels outside of the transverse radiation area, so the electron beam may need focusing during propagation along the undulator. The emittance, the area in the transverse phase space occupied by the electrons, induces an effective longitudinal energy spread in addition to the 1D energy spread [33]. This modifies the energy spread requirement slightly, so that for lasing $\Delta_\gamma < \rho$, where $\Delta_\gamma = \sqrt{\sigma_\gamma^2 + \sigma_\epsilon^2}$ is the total energy spread due to both the longitudinal energy spread and the effective energy spread from the beam emittance.

2.4 Limitations of Theory

The most widely used FEL codes(see e.g. GENESIS 1.3 [21], FAST [22], and GINGER [20]) perform the period averaging and SVEA as outlined in section 2.1.2. In general, it is the equations for the steady state system which are numerically solved. If slippage is to be included i.e. including the effects of a finite length electron beam, then the electron beam is represented by many self-contained electron phase-space slices, which independently solve the steady state FEL model, see figure 2.8. Each beam slice simulates an electron phase-space with periodic boundary conditions. To simulate the slippage, the radiation field is shifted along to the next slice in sequence after calculation. This artificial method of simulating

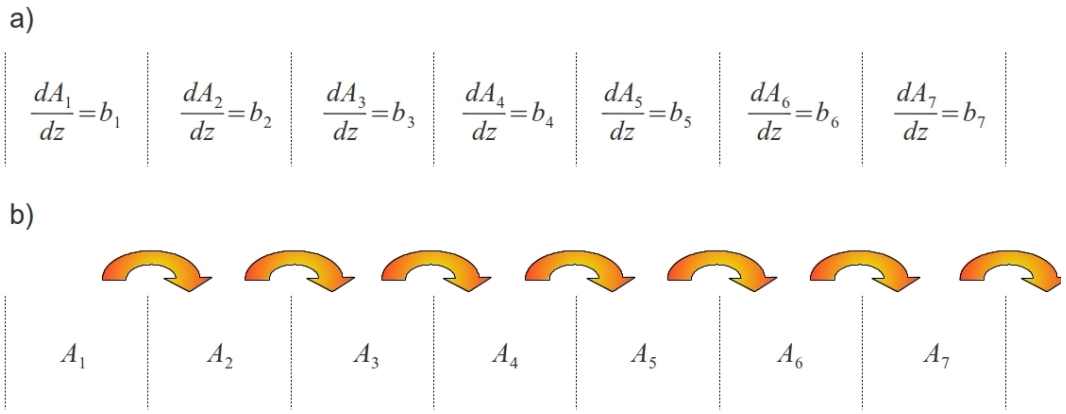

Figure 2.8: Figure illustrating how slippage is simulated in an averaged FEL code. Each electron slice calculates its own independent value of A, and then passes it on to the next slice. The electrons within each slice then interact with that portion of the field, amplify it, then pass it on. Each slice contains an electron distribution which is averaged over to give the bunching parameter b.

slippage is nevertheless evidently very successful. The codes have been extensively benchmarked against experiment and found to give excellent agreement (see, for example, [16], which compares Genesis simulations with measurements from the LCLS).

The disadvantages are that the codes cannot describe the field amplification from variations occuring within an averaged period. This means that they cannot simulate coherent radiation arising from quickly varying current gradients in the pulse, called Coherent Spontaneous Emission (CSE). As the electron beam slices exist in a self-contained cyclic phase space, electrons cannot be exchanged between them. This is especially problematic when simulating short electron pulses, if the energy changes imposed by the FEL interaction cause electrons to travel from one end of the pulse to the other, or if there is a chirp in the pulse, in which case a small electron pulse's size will change significantly with respect to the original bunch length.

Some promising new schemes to improve the temporal coherence are the use of HHG (High Harmonic Gain) seeds [34] produced in gas jets, and EEHG (Echo-Enabled Harmonic Generation) [35]. The HHG seed has a rapidly varying tempo-

ral structure as it contains many harmonics, and so it may be invalid to describe it using the SVEA. The EEHG scheme requires that electrons undergo large changes in longitudinal position, which may violate the period averaging. The restriction on the bandwidth increases with higher harmonics, so proposals which require modelling up to high harmonic numbers will become difficult to model in an averaged code [25]. The mode-locked FEL [36] produces output with a frequency distribution with features similar to a spectral comb (modulated by the FEL spectral distribution), which may violate the SVEA. As yet more exotic methods are proposed to improve temporal coherence, the limit of the SVEA FEL model may begin to break down. Laser plasma accelerators, a promising driver of compact, so-called table-top FEL's [37], produce very short electron bunches on the order of a few resonant wavelengths long. If these are to drive FEL's it would seem inevitable that an unaveraged code would be required to properly describe it.

A number of 1D codes exist which do not perform the period averaging, see for example [38], [39] and [40]. The code presented in this thesis is the first unaveraged code in 3D, exhibiting diffraction and transverse emittance effects, as well as a fully longitudinal electron beam and a quickly oscillating envelope. The advantages are, of course, an enhanced resolution of the FEL, including a self consistent modelling of the full radiation spectrum and polarization. The disadvantages are an increased memory requirement and process time. The next chapter details the theory of this new 3D unaveraged model.

Chapter 3

Analytic Model

A theory and numerical model for the Free Electron Laser was previously developed in [41] which described a helical undulator FEL. The lack of limiting assumptions in the theory meant that it could describe situations in 3D which had previously been unexplored. That theoretical model is now extended to describe an undulator with variable polarization.

In the first section the mathematical definitions and assumptions in the system are presented and explained or justified. Then in the subsequent sections the derivation of the working equations for the numerical model are presented in full.

3.1 Definitions

3.1.1 Undulator and Radiation Field

An undulator with a variable polarization is defined

$$\mathbf{B}_w = \frac{B_{w0}}{2}(\hat{\mathbf{f}}e^{-ik_w z} + c.c.) \tag{3.1}$$

where $k_w = \dfrac{2\pi}{\lambda_w}$ is the wiggler wavenumber and

$$\hat{\mathbf{f}} = f_x\hat{\mathbf{x}} + f_y i\hat{\mathbf{y}} \tag{3.2}$$

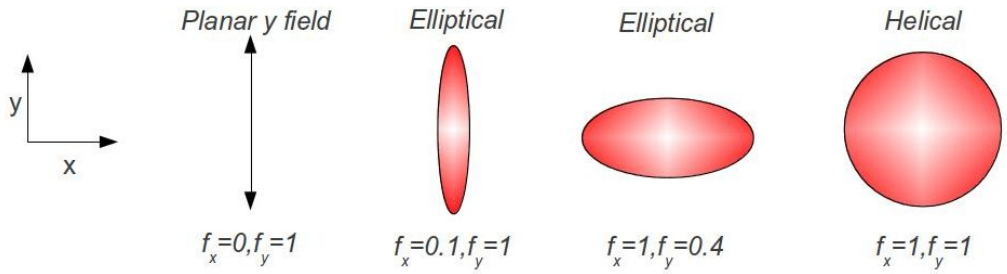

Figure 3.1: The undulator polarization is controlled by f_x and f_y as above.

is an unnormalised basis vector for the undulator. The variables $f_{x,y}$ control the relative magnitudes of the magnetic field in x and y, expressed as fractions of the peak magnetic field B_{w0}. This is illustrated in figure 3.1. Note that there is a fixed phase relationship between the x and y magnetic fields. Only the magnitudes of the field can be altered.

Note that the basis vector $\hat{\mathbf{f}}$ is not normalised. Writing (3.1) in trigonometric form to explicitly show the x and y fields gives

$$\mathbf{B}_w = B_{w0}(\hat{\mathbf{x}} f_x \cos(k_w z) + \hat{\mathbf{y}} f_y \sin(k_w z)) \tag{3.3}$$

This means that a planar undulator for instance may be defined with $f_x = 1$ and $f_y = 0$, and a helical with $f_x = 1$ and $f_y = 1$. It is felt that the undulator definition is more intuitive in this way, as opposed to using a normalised expression. In this unnormalised form either f_x or f_y must $= 1$ for a given wiggler polarization.

The RMS magnetic field is then

$$B_w^{RMS} = \frac{B_{w0}}{\sqrt{2}} \sqrt{f_x^2 + f_y^2} \tag{3.4}$$

and the RMS undulator parameter $\bar{a}_w$ is defined using the RMS undulator field

$$\bar{a}_w = \frac{e B_w^{RMS}}{mck_w} \tag{3.5}$$

The electromagnetic field is composed of a complex envelope $\xi_0(x, y, z, t)$ and a fast oscillatory exponential term, and takes the form

$$\mathbf{E}(x, y, z, t) = \frac{1}{\sqrt{2}} (\hat{e}\xi_0(x, y, z, t) e^{i(kz - \omega t)} + c.c.) \tag{3.6}$$

where

$$\hat{\mathbf{e}} \equiv \frac{1}{\sqrt{2}}(\hat{\mathbf{x}} + i\hat{\mathbf{y}}) \tag{3.7}$$

is a normalized vector basis for a circular polarized field.

Projecting the field described in equation (3.6) over $\hat{\mathbf{e}}^*$ gives

$$E_x - iE_y = \xi_0 e^{i(kz-\omega t)} \tag{3.8}$$

A new term $E_\perp$, the perpendicular field, is then defined so that

$$E_\perp \equiv E_x - iE_y = \xi_0 e^{i(kz-\omega t)} \tag{3.9}$$

and the radiation field vector can be expressed as

$$\mathbf{E}(x, y, z, t) = \frac{1}{\sqrt{2}}(\hat{\mathbf{e}}E_\perp + c.c.) \tag{3.10}$$

3.1.2 FEL Parameters and Scaled Variables

The FEL interaction is solved using the 3D coupled Maxwell-Lorentz equations, which are

$$\nabla^2\mathbf{E} - \frac{1}{c^2}\frac{\partial^2\mathbf{E}}{\partial t^2} = \mu_0\frac{\partial\mathbf{J}}{\partial t} + \frac{1}{\epsilon_0}\nabla\rho \tag{3.11}$$

$$\mathbf{F} = \frac{d\mathbf{p}_j}{dt} = -e(\mathbf{E} + \frac{\mathbf{p}_j}{\gamma_j m} \times \mathbf{B}) \tag{3.12}$$

Here, the Compton limit is assumed in which the space charge term $\nabla\rho$, where for this equation only ρ is the charge density, may be neglected and is done so from now on.

The change in energy of the electrons is described by:

$$\frac{d\gamma_j}{dt} = -\frac{e}{mc}\beta_j \cdot \mathbf{E} \tag{3.13}$$

The Pierce parameter describes the strength or efficiency of the FEL interaction and is given by

$$\rho \equiv \frac{1}{\gamma_r}\left(\frac{\bar{a}_w\omega_p}{4ck_w}\right)^{\frac{2}{3}} \tag{3.14}$$

where

$$\omega_p = \sqrt{\frac{e^2 n_p}{\epsilon_0 m}} \tag{3.15}$$

is the non-relativistic plasma frequency, and n_p the peak electron density.

In the derivation, the variables are scaled to dimensionless quantities consistent with the notation used in the 1D steady state model in section 2.1.2 and [27]. A list of the scaled variables, their mathematical definition, and description is given in the table in figure 3.2

The scaled variables are used as it allows one to see easily how the various important characteristics relate to one another. So one unit in $\bar{z}$ is one exponential gain length, and one unit in $\bar{z}_2$ is the cooperation length, and one resonant wavelength in $\bar{z}_2$ (and also one wiggler period in $\bar{z}$) is $4\pi\rho$. The saturation value for the intensity is $|A|^2 \approx 1$.

3.1.3 Approximations

The Paraxial approximation is applied to the system which assumes small angles from the z axis, meaning that $\frac{\partial}{\partial t} \approx c\frac{\partial}{\partial z}$ for the radiation field and $\frac{d}{dt} \approx \bar{v}_z \frac{d}{dz}$ for the electrons, where $\bar{v}_z$ is the average velocity of the electron beam in the z direction.

As discussed in section 2.1.2, rather than make the Slowly Varying Envelope Approximation, which would restrict the available frequency content to wavelengths around the resonant frequency, instead only the backwards wave is neglected via the approximation

$$\left| \left(\frac{\partial}{\partial z} + \frac{1}{c}\frac{\partial}{\partial t} \right) E_\perp \right| \ll \left| \frac{1}{c}\frac{\partial}{\partial t} E_\perp \right| \tag{3.16}$$

which in the scaled notation is

$$\left| \frac{\partial E_\perp}{\partial \bar{z}} \right| \ll \left| \frac{2\bar{\beta}_z}{1-\bar{\beta}_z} \frac{\partial E_\perp}{\partial \bar{z}_2} \right| \tag{3.17}$$

This approximation, expressed in this form, shows the radiation envelope is varying slowly in $\bar{z}$ with respect to the radiation field rate of change in $\bar{z}_2$. This

Variable	Mathematical Definition	Description
$\bar{z}$	$\frac{z}{l_g} = 2k_w\rho z$	Scaled propagation distance
$\bar{z}_2$	$\frac{(ct-z)}{l_c} = 2k\rho z$	Scaled time coordinate
l_g	$\frac{\lambda_w}{4\pi\rho}$	Exponential gain length
l_c	$\frac{\lambda_r}{4\pi\rho}$	Cooperation length
$E_\perp$	$E_x - iE_y$	Perpendicular radiation field
$p_\perp$	$p_x - ip_y$	Perpendicular electron momentum
$A_\perp$	$\frac{e\sqrt{f_x^2+f_y^2}}{\sqrt{2}mc\omega_p\sqrt{\gamma_r\rho}}E_\perp$	Scaled perpendicular field
A	$\frac{e\sqrt{f_x^2+f_y^2}}{\sqrt{2}mc\omega_p\sqrt{\gamma_r\rho}}\xi_0$	Scaled field envelope
η	$\frac{1-\beta_z}{\bar{\beta}_z}$	Scaled average z velocity of electrons
p_{2j}	$\frac{1}{\eta}\frac{1-\beta_{zj}}{\beta_{zj}}$	Scaled instantaneous energy
$\bar{p}_\perp$	$\frac{p_\perp}{mc}$	Scaled perpendicular electron momentum
$\bar{x}$	$\frac{x}{\sqrt{l_g l_c}}$	Scaled x coordinate
$\bar{y}$	$\frac{y}{\sqrt{l_g l_c}}$	Scaled y coordinate

Figure 3.2: Table describing the scaled notation. The final working equations for the code will be expressed in terms of these variable.

means, in the $\bar{z}_2$ or time frame, the field envelope can be described by complex structures and even model discontinuities. The restriction is on the growth or gain of these (potentially) complex structures as the field propogates through the wiggler in $\bar{z}$. Furthermore, the factor in equation (3.17) $\frac{2\bar{\beta}_z}{1-\bar{\beta}_z} \gg 1$ in the FEL (the electron beam is relativistic), so the condition is not anticipated to be violated.

The consequences of this can be seen directly from the Maxwell equation

$$\nabla \times \mathbf{E} = -\frac{\partial \mathbf{B}_f}{\partial t} \tag{3.18}$$

$$\Rightarrow \frac{\partial E_x}{\partial z} = -\frac{\partial B_{fy}}{\partial t} \tag{3.19}$$

$$\frac{\partial E_y}{\partial z} = \frac{\partial B_{fx}}{\partial t} \tag{3.20}$$

Changing to scaled variables $(\bar{z}, \bar{z}_2)$ gives

$$\left(\frac{\partial}{\partial \bar{z}} - \frac{\bar{\beta}_z}{1-\bar{\beta}_z}\frac{\partial}{\partial \bar{z}_2}\right) E_x = -c\frac{\bar{\beta}_z}{1-\bar{\beta}_z}\frac{\partial B_y}{\partial \bar{z}_2} \tag{3.21}$$

$$\left(\frac{\partial}{\partial \bar{z}} - \frac{\bar{\beta}_z}{1-\bar{\beta}_z}\frac{\partial}{\partial \bar{z}_2}\right) E_y = c\frac{\bar{\beta}_z}{1-\bar{\beta}_z}\frac{\partial B_x}{\partial \bar{z}_2} \tag{3.22}$$

Here the approximation, in the form (3.17), can easily be applied, and it is seen that

$$E_x \approx cB_y \tag{3.23}$$

$$E_y \approx -cB_x \tag{3.24}$$

The Poynting vector is then

$$\mathbf{S} = \frac{1}{\mu_0}\mathbf{E} \times \mathbf{B} \tag{3.25}$$

$$= \frac{1}{\mu_0}(E_x B_y - E_y B_x) \tag{3.26}$$

$$= \frac{|E_\perp|^2}{\mu_0 c} \tag{3.27}$$

meaning that the approximation is equivalent to electromagnetic radiation travelling in the forward (positive $\bar{z}$) direction only being modelled.

The magnetic component of the radiation field is then:

$$\mathbf{B}_f = -\frac{i}{\sqrt{2}c}\left(\hat{\mathbf{e}}E_\perp - c.c.\right) \tag{3.28}$$

So the full combined undulator and radiation magnetic field vector is

$$\mathbf{B} = \frac{B_w}{2}(\hat{\mathbf{f}}e^{-ik_w z} + c.c.) - \frac{i}{\sqrt{2}c}\left(\hat{\mathbf{e}}E_\perp - c.c.\right) \tag{3.29}$$

3.1.4 Field Polarization

The general elliptical wiggler field defined for use in the code can be varied from a linear to helical polarization, and the electron beam evolves in accordance with the supplied wiggler polarization. To complete the model, the field, including its polarization, must evolve consistently with the electron evolution.

It is shown here how the electromagnetic field can be considered elliptically polarized, as the envelope and phase are functions of both $\bar{z}$ and $\bar{z}_2$.

The electromagnetic field is defined in its basic general form as equation (3.6) which, re-expressed in the scaled notation is

$$\mathbf{A}(\bar{x},\bar{y},\bar{z},\bar{z}_2) = \frac{1}{\sqrt{2}}\left(\hat{\mathbf{e}}A(\bar{x},\bar{y},\bar{z},\bar{z}_2)e^{-i(\bar{z}_2/2\rho)} + c.c.\right) \tag{3.30}$$

where $A(\bar{x},\bar{y},\bar{z},\bar{z}_2)$ describes a complex envelope at the resonant wavelength.

A scaled perpendicular field may be written

$$A_\perp = A\exp(-i(\bar{z}_2/2\rho)) = A_x - iA_y \tag{3.31}$$

where A_x and A_y are the scaled fields in $\bar{x}$ and $\bar{y}$.

Expanding the complex envelope A into its magnitude $|A|$ and phase ψ gives

$$A_x = |A|\cos(\bar{z}_2 - \psi) \tag{3.32}$$

$$A_y = |A|\sin(\bar{z}_2 - \psi) \tag{3.33}$$

i.e. the fields in x and y have a fixed phase difference. This description is capable of modelling any elliptical polarization. Polarization changes are achieved by varying the envelope parameters $|A|$ and ψ, which are functions of $\bar{z}$ and $\bar{z}_2$. To

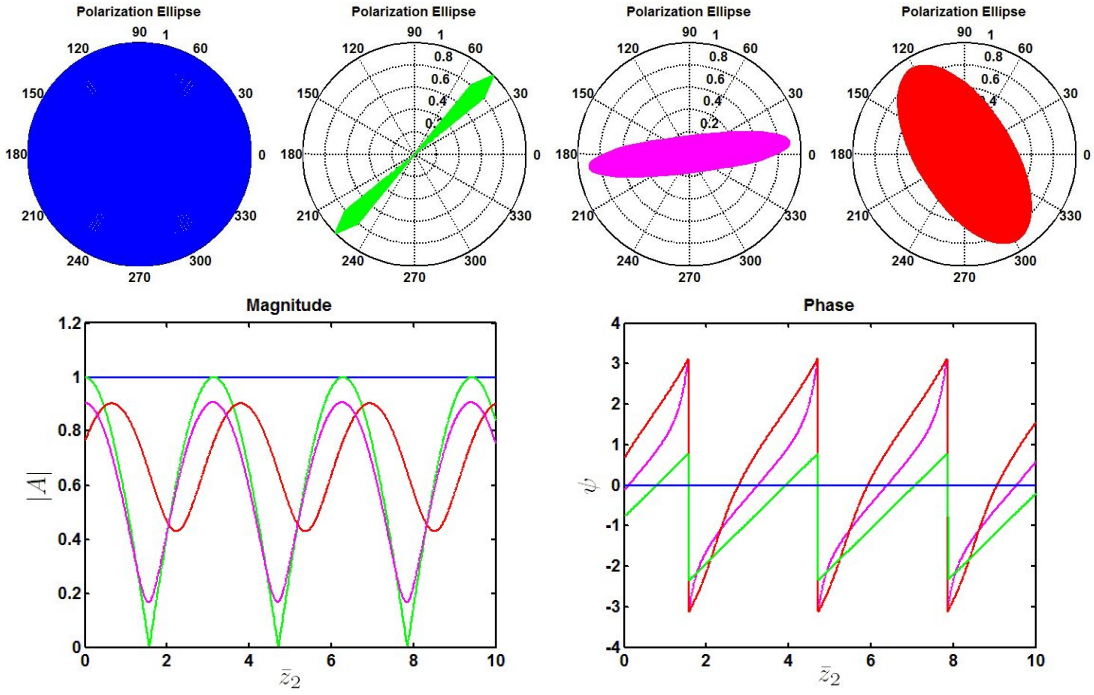

Figure 3.3: The above plots show how the phase and magnitude of the envelope can vary to achieve different polarizations.

obtain the complex envelope for the desired polarization we can first rearrange (3.31) into

$$A = A_\perp \exp(i(\bar{z}_2/2\rho)) \tag{3.34}$$

$$= (A_x - iA_y)(\cos(\bar{z}_2/2\rho) + i\sin(\bar{z}_2/2\rho)) \tag{3.35}$$

$$Re(A) = A_x \cos(\bar{z}_2/2\rho) + A_y \sin(\bar{z}_2/2\rho) \tag{3.36}$$

$$Im(A) = A_x \sin(\bar{z}_2/2\rho) - A_y \cos(\bar{z}_2/2\rho) \tag{3.37}$$

and so the magnitude

$$|A| = \sqrt{Re(A)^2 + Im(A)^2} \tag{3.38}$$

$$= \sqrt{(A_x \cos(\bar{z}_2/2\rho) + A_y \sin(\bar{z}_2/2\rho))^2 + (A_x \sin(\bar{z}_2/2\rho) + A_y \cos(\bar{z}_2/2\rho))^2} \tag{3.39}$$

$$= \sqrt{A_x^2(\cos^2(\bar{z}_2/2\rho) + \sin^2(\bar{z}_2/2\rho)) + A_y^2(\sin^2(\bar{z}_2/2\rho) + \cos^2(\bar{z}_2/2\rho))} \tag{3.40}$$

$$= \sqrt{A_x^2 + A_y^2} \tag{3.41}$$

and the phase

$$\tan\psi = \left(\frac{Im(A)}{Re(A)}\right) \tag{3.42}$$

$$\tan\psi = \left(\frac{A_x \sin(\bar{z}_2/2\rho) - A_y \cos(\bar{z}_2/2\rho)}{A_x \cos(\bar{z}_2/2\rho) + A_y \sin(\bar{z}_2/2\rho)}\right) \tag{3.43}$$

So for a simple linear polarization in x, for example, define a resonant wave $A_x = \cos(\bar{z}_2/2\rho)$ and $A_y = 0$ giving $|A| = |\cos(\bar{z}_2/2\rho)|$ and $\psi = \arctan(\tan(\bar{z}_2/2\rho))$. Examples of different field polarizations and the envelope parameters required to describe them are shown in figures 3.3. The plots were produced using Matlab by simply evaluating the analytic expressions given above for a desired field in $\bar{x}$ and $\bar{y}$.

3.1.5 Outline Of Derivation

In the next section the final working equations are derived in detail, from the starting points of the previous sections. First the electron equations are derived, and then the field equation.

For the transverse forces on the electrons, the equations are manipulated so that they may be expressed in terms of the scaled variables. The equation for the scaled longitudinal momentum of the electrons is an equation which combines both the variation in the longitudinal momentum and the energy exchange with the electromagnetic field. The field equation is derived with the backwards wave neglected as in section 3.1.3

3.2 Electron Equations

3.2.1 Transverse Electron Momentum

Starting from the Lorentz force equation for the jth electron

$$\mathbf{F}_j = \frac{d\mathbf{p}_j}{dt} = -e(\mathbf{E}_j + \frac{\mathbf{p}_j}{\gamma_j m} \times \mathbf{B}_j), \tag{3.44}$$

Transforming the independent variable from $t \rightarrow z$ so that $\frac{d}{dt} = c\beta_{zj}\frac{d}{dz}$, changing then to the scaled independent variable $\bar{z} = 2k_w\rho z$ and dependent $\bar{z}_{2j} = 2k_w\rho\frac{\bar{\beta}_{zj}}{1-\bar{\beta}_{zj}}(ct_j - z)$ so that $\frac{d}{d\bar{z}} = 2k_w\rho\frac{d}{dz}$, $\frac{\bar{z}_{2j}}{2\rho} = -(kz - \omega t_j)$ and $\frac{\bar{z}}{2\rho} = k_w z$ and projecting over $\hat{\mathbf{e}}^*$ gives

$$\frac{1}{\sqrt{2}}\frac{dp_{\perp j}}{d\bar{z}} = -\frac{e}{2\sqrt{2}k_w\rho c\beta_{zj}}\Big[E_{\perp j} - \frac{p_{zj}}{\gamma_j m}(B_{yj} + iB_{xj})\Big] \tag{3.45}$$

Here $E_{\perp j} = E(\bar{x}_j, \bar{y}_j, \bar{z}_{2j}, \bar{z})$.

The combined undulator and radiation magnetic field is described in equation (3.29), and from this

$$B_{xj} = B_{wo}f_x\cos(\bar{z}/2\rho) - \frac{E_{yj}}{c} \tag{3.46}$$

$$B_{yj} = B_{w0}f_x\sin(\bar{z}/2\rho) + \frac{E_{xj}}{c}. \tag{3.47}$$

And so in equation (3.45)

$$\begin{aligned}\frac{dp_{\perp j}}{d\bar{z}} = -\frac{e}{2k_w\rho c\beta_{zj}}\Big[E_{\perp j} - \frac{p_{zj}}{\gamma_j m}(B_{w0}f_y\sin(\bar{z}/2\rho) + \frac{E_{xj}}{c} \\ + i(B_w f_x\cos(\bar{z}/2\rho) - \frac{E_{yj}}{c}))\Big]\end{aligned} \tag{3.48}$$

$$\begin{aligned}\Rightarrow \frac{dp_{\perp j}}{d\bar{z}} = -\frac{e}{2k_w\rho c\beta_{zj}}\Big[E_{\perp j} - \frac{p_{zj}}{\gamma_j m}(B_{w0}(f_y\sin(\bar{z}/2\rho) + if_x\cos(\bar{z}/2\rho)) + \\ \frac{1}{c}(E_{xj} - iE_{yj}))\Big]\end{aligned} \tag{3.49}$$

Remembering $E_\perp = E_x - iE_y$, and defining a new complex term G describing the undulator field such that

$$G = f_x\cos(\bar{z}/2\rho) + if_y\sin(\bar{z}/2\rho), \tag{3.50}$$

equation (3.49) becomes

$$\frac{dp_{\perp j}}{d\bar{z}} = -\frac{e}{2k_w\rho c\beta_{zj}}\Big[E_{\perp j} - \frac{p_{zj}}{\gamma_j m}(iB_{w0}G^* + \frac{E_{\perp j}}{c})\Big] \tag{3.51}$$

Taking the factor of $1/c\beta_{zj}$ inside the brackets the equation becomes

$$\frac{dp_{\perp j}}{d\bar{z}} = -\frac{e}{2k_w\rho}\Big[\frac{E_{\perp j}}{c\beta_{zj}} - \frac{p_{zj}}{\gamma_j mc\beta_{zj}}(iB_{w0}G^* + \frac{E_{\perp j}}{c})\Big] \tag{3.52}$$

$$\frac{dp_{\perp j}}{d\bar{z}} = -\frac{e}{2k_w\rho}\Big[\frac{E_{\perp j}}{c\beta_{zj}} - iB_{w0}G^* - \frac{E_{\perp j}}{c}\Big] \tag{3.53}$$

$$\frac{dp_{\perp j}}{d\bar{z}} = \frac{e}{2k_w\rho}\Big[iB_{w0}G^* + \frac{E_{\perp j}}{c}(1 - \frac{1}{\beta_{zj}})\Big] \tag{3.54}$$

From the definition of p_{2j},

$$\eta p_{2j} = \frac{1-\beta_{zj}}{\beta_{zj}} = \frac{1}{\beta_{zj}} - 1, \tag{3.55}$$

changing to the scaled $\bar{p}_\perp = p_\perp/mc$, and using the definition of $\bar{a}_w$ in equation (3.5),

$$\frac{d\bar{p}_{\perp j}}{d\bar{z}} = \frac{1}{2\rho}\Big(\frac{\sqrt{2}\bar{a}_w}{\sqrt{f_x^2+f_y^2}}iG^* - \frac{e\eta p_{2j}E_{\perp j}}{mc^2k_w}\Big) \tag{3.56}$$

Finally, scaling to $A_\perp$ using the definition in table 3.2, and rearranging the definition of ρ in equation (3.14) to obtain an expression for the plasma frequency,

$$\omega_p = \frac{4ck_w(\gamma_r\rho)^{3/2}}{\bar{a}_w} \tag{3.57}$$

so that

$$\frac{e}{mc^2k_w}E_\perp = \frac{4\sqrt{2}\gamma_r^2\rho^2}{\sqrt{f_x^2+f_y^2}\bar{a}_w}, \tag{3.58}$$

the equation becomes

$$\frac{d\bar{p}_{\perp j}}{d\bar{z}} = \frac{1}{2\rho}\Big(\frac{\sqrt{2}\bar{a}_w}{\sqrt{f_x^2+f_y^2}}iG^* - \frac{4\sqrt{2}\gamma_r^2\rho^2\eta p_{2j}}{\sqrt{f_x^2+f_y^2}\bar{a}_w}A_{\perp j}\Big) \tag{3.59}$$

$$\frac{d\bar{p}_{\perp j}}{d\bar{z}} = \frac{\bar{a}_w}{\sqrt{2(f_x^2+f_y^2)}\rho}\Big(iG^* - \Big(\frac{2\gamma_r\rho}{\bar{a}_w}\Big)^2\eta p_{2j}A_{\perp j}\Big) \tag{3.60}$$

Focusing Effects on the Transverse Electron Motion

The finite electron beam emittance in x and y can result in decoupling between the beam and radiation, which diminishes or eliminates the field amplification. To counteract this, the electron beam may be focused in the transverse directions. In lower energy FEL's, the natural focusing provided by the undulator can be sufficient to confine the electron beam to a desired transverse area. The natural focusing arises from the off-axis magnetic field of the wiggler, which up till now has not been taken into account. Close to the z axis it can be approximated as a constant, linear focusing channel super-imposed upon the normal wiggle motion [42], taken simply as

$$\frac{d^2x}{dz^2} = -k_{\beta n}^2 x, \frac{d^2y}{dz^2} = -k_{\beta n}^2 y \tag{3.61}$$

It is seen that the electron beam will undergo an additional oscillation, called the betatron oscillation, with wavenumber $k_{\beta n}$, the natural betatron wavenumber, which is much smaller than k_w. Natural focusing in a planar wiggler can be achieved in both transverse directions by using curved pole faces [42].

In higher energy FEL's, the beam is focused by external quadrupoles, usually in a configuration known as a FODO lattice [32]. The quadrupoles are inserted periodically between undulator sections. Each undulator-quadrupole section is known as a FODO cell, and many such cells comprise the lattice. Assuming the the FODO cell length is smaller than both the betatron wavelength and the gain length, it may also be approximated as a linear focusing channel. Strictly speaking, the betatron wavenumber varies across the length of the FODO cell, with the strength of the focusing dipping in the middle, but the deviation from the mean focusing strength is assumed to be small.

It is possible to "match" the electron beam transverse area to the focusing channel [42], by choosing the initial transverse beam parameters such that a constant beam radius in the transverse plane is achieved. The electrons will then oscillate within this constant beam envelope with period $2\pi/k_\beta$, with different magnitudes and phases.

The focusing described in the theory here is the natural focusing of the helical undulator, and is artificially strengthened or relaxed, if desired, by use of a focusing factor, to achieve the correct betatron oscillation.

It is assumed that a uniform focusing channel exists in both $\bar{x}$ and $\bar{y}$ for any values of $f_{x,y}$. This provides a restoring force which results in electron oscillations within a beam envelope, given by the maximum amplitudes of the electron oscillations within the beam. In a helical undulator the betatron wavenumber can be approximated as

$$k_{\beta n} = \frac{\bar{a}_w k_w}{\sqrt{2}\gamma} \tag{3.62}$$

The factor of $\sqrt{2}$ is now replaced by a general focusing factor f [43], to alter the focusing strength, so that the focusing channel is now described as [33]

$$\frac{d^2 x_j}{dz^2} = -\frac{\bar{a}_w^2 k_w^2}{f^2 \gamma_j^2} x_j, \tag{3.63}$$

where $k_\beta = \dfrac{\bar{a}_w k_w}{f\gamma}$ is the new betatron wavenumber.

Expressing (3.63) in terms of $\bar{p}_{xj} = \dfrac{\gamma_j}{c}\dfrac{dx_j}{dt} = \gamma_j \beta_{zj} \dfrac{dx_j}{dz}$ gives

$$\frac{d\bar{p}_{xj}}{dz} = \gamma \beta_{zj} (-k_\beta^2 x_j) \tag{3.64}$$

and changing the independent variable to $\bar{z}$

$$\frac{d\bar{p}_{xj}}{d\bar{z}} = \frac{\gamma_j \beta_{zj}}{2k_w \rho} (-k_\beta^2 x_j) \tag{3.65}$$

and changing to the scaled $\bar{x}$ via the table in figure 3.2 (so that $x = \sqrt{l_g l_c}\bar{x}$),

$$\frac{d\bar{p}_{xj}}{d\bar{z}} = -\frac{\gamma_j \beta_{zj}}{2k_w \rho} k_\beta^2 \sqrt{l_g l_c}\bar{x}_j \tag{3.66}$$

$$\frac{d\bar{p}_{xj}}{d\bar{z}} = -\frac{\gamma_j \beta_{zj}}{2k_w \rho} \frac{\bar{a}_w^2 k_w^2}{f^2 \gamma_j^2} \sqrt{l_g l_c}\bar{x}_j \tag{3.67}$$

$$\frac{d\bar{p}_{xj}}{d\bar{z}} = -\frac{\beta_{zj} \bar{a}_w^2 k_w}{2f^2 \gamma_j \rho} \frac{1}{2\rho\sqrt{k_w k}} \bar{x}_j \tag{3.68}$$

$$\frac{d\bar{p}_{xj}}{d\bar{z}} = -\frac{\beta_{zj} \bar{a}_w^2}{4f^2 \gamma_j \rho^2} \sqrt{\frac{k_w}{k}} \bar{x}_j \tag{3.69}$$

$$\frac{d\bar{p}_{xj}}{d\bar{z}} = -\frac{\beta_{zj} \bar{a}_w^2 \sqrt{\eta}}{4f^2 \gamma_j \rho^2} \bar{x}_j \tag{3.70}$$

$$\tag{3.71}$$

Similarly for y,

$$\frac{d\bar{p}_{yj}}{d\bar{z}} = -\frac{\beta_{zj} \bar{a}_w^2 \sqrt{\eta}}{4f^2 \gamma_j \rho^2} \bar{y}_j \tag{3.72}$$

So the full transverse momentum equation, including focusing effects, is

$$\frac{d\bar{p}_{\perp j}}{d\bar{z}} = \frac{\bar{a}_w}{\sqrt{2(f_x^2 + f_y^2)}\rho} \left(iG^* - \left(\frac{2\gamma_r \rho}{\bar{a}_w} \right)^2 \eta p_{2j} A_{\perp j} \right) - \frac{\beta_{zj} \bar{a}_w^2 \sqrt{\eta}}{4f^2 \gamma_j \rho^2} (\bar{x}_j - i\bar{y}_j) \tag{3.73}$$

Recalling the betatron wavenumber in equation (3.62), and scaling to the scaled betatron wavenumber $\bar{k}_\beta$ in the propagation distance $\bar{z}$,

$$\bar{k}_\beta = l_g k_\beta \tag{3.74}$$

$$\bar{k}_\beta = \frac{1}{2k_w \rho} \frac{\bar{a}_w k_w}{f\gamma} \tag{3.75}$$

$$\bar{k}_\beta = \frac{\bar{a}_w}{2f\rho\gamma} \tag{3.76}$$

$$\Rightarrow f\bar{k}_\beta = \frac{\bar{a}_w}{2\rho\gamma} \tag{3.77}$$

So the transverse momentum equation is then

$$\frac{d\bar{p}_{\perp j}}{d\bar{z}} = \frac{\bar{a}_w}{\sqrt{2(f_x^2 + f_y^2)}\rho} \left(iG^* - \frac{\eta p_{2j}}{f^2 \bar{k}_\beta^2} A_{\perp j} \right) - \gamma_j \beta_{zj} \bar{k}_\beta^2 \sqrt{\eta} (\bar{x}_j - i\bar{y}_j) \tag{3.78}$$

Matched Beam

The definition of the transverse emittance is

$$\epsilon = r_x r_{x'} \tag{3.79}$$

where $x' = \dfrac{dx}{dz}$. The normalised emittance is $\epsilon_n = \gamma_r \epsilon$.

For a matched beam, with individual electrons oscillating with wavenumber k_β, $r_{x'} = k_\beta r_x$, so the matched transverse radius is given by

$$r_x = \sqrt{\frac{\epsilon_n}{\gamma_r k_\beta}} \tag{3.80}$$

For the transverse beam dynamics a scaled emittance $\bar{\epsilon}$ is introduced such that

$$\bar{\epsilon} = \frac{\epsilon}{2\rho l_c} \tag{3.81}$$

Scaling the transverse coordinates with $\bar{r}_x = \dfrac{r_x}{\sqrt{l_g l_c}}$, and using definitions (3.74) and (3.81), equation (3.80) becomes

$$\sqrt{l_g l_c}\bar{r}_x = \sqrt{\frac{\gamma_r \epsilon}{\gamma_r k_\beta}} \tag{3.82}$$

$$\bar{r}_x = \sqrt{\frac{\epsilon}{l_c \bar{k}_\beta}} \tag{3.83}$$

$$\bar{r}_x = \sqrt{\frac{2\rho\bar{\epsilon}}{\bar{k}_\beta}}. \tag{3.84}$$

The undulator wavelength in $\bar{z}$ (and the resonant wavelength in $\bar{z}_2$) is $\bar{k}_w = \dfrac{1}{2\rho}$, so

$$\bar{r}_x = \sqrt{\frac{\bar{\epsilon}}{\bar{k}_w \bar{k}_\beta}}. \tag{3.85}$$

To find the matched $\bar{r}_{px}$, one must first of all relate $\bar{p}$ to $\dfrac{dx}{dz}$, which is achieved in the following by approximating γ_j by the resonant energy γ_r, $\dfrac{d}{dt}$ by $c\dfrac{d}{dz}$, and

remembering that $\bar{p}_x = \dfrac{p_x}{mc}$,

$$p_{xj} = \gamma_j m \frac{dx}{dt} \tag{3.86}$$

$$p_{xj} \approx \gamma_r mc \frac{dx}{dz} \tag{3.87}$$

$$\Rightarrow \bar{p}_{xj} \approx \gamma_r \frac{dx}{dz}. \tag{3.88}$$

Therefore, $\bar{r}_{px} = \gamma_r r_{x'}$. So rearranging the emittance definition (3.79):

$$\sigma_{x'} = \frac{\epsilon}{\sigma_x} \tag{3.89}$$

and then scaling to $\bar{x}$, and using equations (3.89), (3.77) and (3.81)

$$\bar{r}_{px} = \frac{\gamma_r \epsilon}{\sqrt{l_g l_c} r_{\bar{x}}} \tag{3.90}$$

$$\bar{r}_{px} = \frac{2\rho l_c \gamma_r \bar{\epsilon}}{\sqrt{l_g l_c} r_{\bar{x}}} \tag{3.91}$$

$$\bar{r}_{px} = \sqrt{l_c l_g} \frac{\bar{a}_w \bar{\epsilon}}{f \bar{k}_\beta r_{\bar{x}}} \tag{3.92}$$

$$\bar{r}_{px} = \frac{\bar{a}_w \sqrt{\eta} \bar{\epsilon}}{f \bar{k}_\beta r_{\bar{x}}} \tag{3.93}$$

The same matching is performed in the $\bar{y}$ direction, so

$$\bar{r}_y = \sqrt{\frac{\bar{\epsilon}}{\bar{k}_w \bar{k}_\beta}} \tag{3.94}$$

$$\bar{r}_{py} = \frac{\bar{a}_w \sqrt{\eta} \bar{\epsilon}}{f \bar{k}_\beta r_{\bar{y}}} \tag{3.95}$$

3.2.2 Longitudinal Electron Momentum

Now the equation for p_2, the scaled momentum in the $\bar{z}_2$ frame, is derived. Starting with the z component of the Lorentz eq (3.12)

$$\frac{dp_{zj}}{d\bar{z}} = -\frac{e}{2k_w \rho c \beta_{zj}} \left(\frac{\mathbf{p}_j}{\gamma_j m} \times \mathbf{B}_j\right)_{\bar{z}} \tag{3.96}$$

The cross product is

$$
\begin{aligned}
&(\mathbf{p}\times\mathbf{B})_z && (3.97)\\
=&p_xB_y - p_yB_x && (3.98)\\
=&p_x\left(B_wf_y\sin(\bar{z}/2\rho)+\frac{1}{2c}\left(E_\perp+c.c.\right)\right) && (3.99)\\
&-p_y\left(B_wf_x\cos(\bar{z}/2\rho)-\frac{i}{2c}\left(E_\perp-c.c.\right)\right)\\
=&\frac{1}{2}(p_\perp+p_\perp^*)\left(B_{w0}f_y\sin(\bar{z}/2\rho)+\frac{1}{2c}\left(E_\perp+c.c.\right)\right) && (3.100)\\
&-\frac{i}{2}(p_\perp-p_\perp^*)\left(B_wf_x\cos(\bar{z}/2\rho)-\frac{i}{2c}\left(E_\perp-c.c.\right)\right)\\
=&\frac{p_\perp}{2}\left(\frac{E_\perp^*}{c}+B_wf_y\sin(\bar{z}/2\rho)-iB_wf_x\cos(\bar{z}/2\rho)\right) && (3.101)\\
&+\frac{p_\perp^*}{2}\left(\frac{E_\perp}{c}+B_wf_y\sin(\bar{z}/2\rho)+iB_wf_x\cos(\bar{z}/2\rho)\right)
\end{aligned}
$$

Substituting back into equation (3.96), and using the definition of G from equation (3.50) gives

$$\frac{dp_{zj}}{d\bar{z}} = -\frac{e}{4k_w\rho\gamma_j mc\beta_{zj}}\left[p_{\perp j}\left(\frac{E_{\perp j}^*}{c}-iB_wG\right)+c.c.\right] \qquad (3.102)$$

This gives the changes in longitudinal electron momentum in the undulator due to the combined magnetic field of the undulator and radiation. To include the energy change due to coupling to the electric component of the radiation field, one can see from the definition of momentum that

$$
\begin{aligned}
\frac{dp_{zj}}{d\bar{z}} &= \frac{d}{d\bar{z}}(\gamma_j mc\beta_{zj}) && (3.103)\\
&= mc\gamma_j\frac{d\beta_{zj}}{d\bar{z}}+mc\beta_{zj}\frac{d\gamma_j}{d\bar{z}} && (3.104)
\end{aligned}
$$

Equation (3.102) can be equated with equation (3.104), but first the variation

in energy can be found by using the expression derived in equation (2.17),

$$\frac{d\gamma_j}{d\bar{z}} = -\frac{e}{2k_w c^2 m\rho\beta zj}\beta_j \cdot \mathbf{E}_j \tag{3.105}$$

$$\beta_j \cdot \mathbf{E}_j = \frac{\mathbf{p}_j}{\gamma_j mc} \cdot \mathbf{E}_j \tag{3.106}$$

$$= \frac{1}{\gamma_j mc}(p_{xj}E_{xj} + p_{yj}E_{yj}) \tag{3.107}$$

$$= \frac{1}{\gamma_j mc}(\frac{1}{2}(p_{\perp j} + p^*_{\perp j})\frac{1}{2}(E_{\perp j} + E^*_{\perp j}) + \frac{i}{2}(p_{\perp j} - p^*_{\perp j})\frac{i}{2}(E_{\perp j} - E^*_{\perp j})) \tag{3.108}$$

$$= \frac{1}{2\gamma_j mc}(p_{\perp j}E^*_{\perp j} + p^*_{\perp j}E_{\perp j}) \tag{3.109}$$

$$\Rightarrow \frac{d\gamma_j}{d\bar{z}} = -\frac{e}{4k_w\rho\gamma_j m^2c^3\beta_{zj}}(p_{\perp j}E^*_{\perp j} + p^*_{\perp j}E_{\perp j}) \tag{3.110}$$

and substituting this back into (3.104) gives

$$\frac{dp_{zj}}{d\bar{z}} = \gamma_j mc\frac{d\beta_{zj}}{d\bar{z}} - \frac{e}{4k_w\rho\gamma_j mc^2}(p_{\perp j}E^*_{\perp j} + p^*_{\perp j}E_{\perp j}) \tag{3.111}$$

Now equation (3.102) can be equated to equation (3.111) to give

$$\gamma_j\frac{d\beta_{zj}}{d\bar{z}} - \frac{e}{4k_w\rho\gamma_j m^2c^3}(p_{\perp j}E^*_{\perp j} + p^*_{\perp j}E_{\perp j}) = -\frac{e}{4k_w\rho\gamma_j m^2c^3\beta_{zj}}\left[p_{\perp j}\left(E^*_{\perp j} - icB_wG\right) + c.c.\right] \tag{3.112}$$

$$\Rightarrow \frac{d\beta_{zj}}{d\bar{z}} = \frac{e}{4k_w m^2c^3\rho\gamma_j^2}\Big[(1 - \frac{1}{\beta_{zj}})(p_\perp E^*_{\perp j} + p^*_{\perp j}E_{\perp j}) + \frac{iB_wc}{\beta_{zj}}(p_{\perp j}G - p^*_{\perp j}G^*)\Big] \tag{3.113}$$

$$\Rightarrow \frac{d\beta_{zj}}{d\bar{z}} = -\frac{e}{4k_w m^2c^3\rho\gamma_j^2}\Big[(\frac{1}{\beta_{zj}} - 1)(p_\perp E^*_{\perp j} + p^*_{\perp j}E_{\perp j}) - \frac{iB_wc}{\beta_{zj}}(p_{\perp j}G - p^*_{\perp j}G^*)\Big] \tag{3.114}$$

$\frac{dp_{2j}}{d\bar{z}} = -\frac{1}{\eta\beta_{zj}^2}\frac{d\beta_{zj}}{d\bar{z}}$, so

$$\begin{aligned}\frac{dp_{2j}}{d\bar{z}} =& \frac{1}{\eta\beta_{zj}^2}\frac{e}{4k_w m^2c^3\rho\gamma_j^2}\Big[(\frac{1}{\beta_{zj}}-1)(p_\perp E_{\perp j}^* + p_{\perp j}^* E_{\perp j}) \\ & - \frac{iB_w c}{\beta_{zj}}(p_{\perp j}G - p_{\perp j}^* G^*)\Big] \end{aligned} \tag{3.115}$$

Scaling the transverse momentum, $\bar{p}_\perp = \frac{p_\perp}{mc}$, so

$$\begin{aligned}\frac{dp_{2j}}{d\bar{z}} =& \frac{1}{\eta\beta_{zj}^2}\frac{e}{4k_w mc^2\rho\gamma_j^2}\Big[(\frac{1}{\beta_{zj}}-1)(\bar{p}_\perp E_{\perp j}^* + \bar{p}_{\perp j}^* E_{\perp j}) \\ & - \frac{iB_w c}{\beta_{zj}}(\bar{p}_{\perp j}G - \bar{p}_{\perp j}^* G^*)\Big]. \end{aligned} \tag{3.116}$$

Scaling the transverse envelope using equation (3.58), and remembering equation (3.5) for the definition of $\bar{a}_w$,

$$\begin{aligned}\frac{dp_{2j}}{d\bar{z}} =& \frac{1}{\eta\beta_{zj}^2}\frac{1}{4\rho\gamma_j^2}\Big[(\frac{1}{\beta_{zj}}-1)\frac{4\sqrt{2}\gamma_r^2\rho^2}{\bar{a}_w\sqrt{f_x^2+f_y^2}}(\bar{p}_\perp A_{\perp j}^* + \bar{p}_{\perp j}^* A_{\perp j}) \\ & - \frac{i}{\beta_{zj}}\frac{\sqrt{2}\bar{a}_w}{\sqrt{f_x^2+f_y^2}}(\bar{p}_{\perp j}G - \bar{p}_{\perp j}^* G^*)\Big] \end{aligned} \tag{3.117}$$

$$\begin{aligned}\frac{dp_{2j}}{d\bar{z}} =& \frac{1}{\eta\beta_{zj}^2}\frac{1}{4\rho\gamma_j^2}\frac{\sqrt{2}\bar{a}_w}{\sqrt{f_x^2+f_y^2}}\Big[(\frac{1}{\beta_{zj}}-1)\left(\frac{4\gamma_r^2\rho^2}{\bar{a}_w^2}\right)(\bar{p}_\perp A_{\perp j}^* + \bar{p}_{\perp j}^* A_{\perp j}) \\ & - \frac{i}{\beta_{zj}}(\bar{p}_{\perp j}G - \bar{p}_{\perp j}^* G^*)\Big] \end{aligned} \tag{3.118}$$

To simplfy the derivation in terms of the scaled variables, first, from the

definition of the relativistic factor one can find

$$\frac{1}{\gamma_j^2} = 1 - \beta_j^2 \tag{3.119}$$

$$\frac{1}{\gamma_j^2} = 1 - \beta_{zj}^2 - (\beta_{xj}^2 + \beta_{yj}^2) \tag{3.120}$$

$$\frac{1}{\gamma_j^2} = 1 - \beta_{zj}^2 - \frac{1}{\gamma_j^2 m^2 c^2}(p_{xj}^2 + p_{yj}^2) \tag{3.121}$$

$$\frac{1}{\gamma_j^2} = 1 - \beta_{zj}^2 - \frac{1}{\gamma_j^2 m^2 c^2}|p_{\perp j}|^2 \tag{3.122}$$

$$\frac{1}{\gamma_j^2} = 1 - \beta_{zj}^2 - \frac{1}{\gamma_j^2}|\bar{p}_{\perp j}|^2 \tag{3.123}$$

$$\Rightarrow \frac{1}{\gamma_j^2} = \frac{1 - \beta_{zj}^2}{1 + |\bar{p}_{\perp j}|^2} \tag{3.124}$$

Next, from (3.55),

$$\frac{1}{\beta_{zj}} = 1 + \eta p_{2j} \tag{3.125}$$

and

$$\frac{1 - \beta_{zj}^2}{\beta_{zj}^2} = \eta p_{2j}(\eta p_{2j} + 2). \tag{3.126}$$

Putting equations (3.124), (3.125) and (3.126) into equation (3.118), and also using the expression for the scaled transverse wavenumber in equation (3.76), gives the final form of the p_2 equation as

$$\frac{dp_{2j}}{d\bar{z}} = \frac{1}{4\rho}\frac{\sqrt{2}\bar{a}_w}{\sqrt{f_x^2 + f_y^2}}\left(\frac{p_{2j}(\eta p_{2j} + 2)}{1 + |\bar{p}_{\perp j}|^2}\right)\Big[\frac{\eta p_{2j}}{f\bar{k}_\beta}(\bar{p}_\perp A_{\perp j}^* + \bar{p}_{\perp j}^* A_{\perp j}) - i(\eta p_{2j} + 1)(\bar{p}_{\perp j} G - \bar{p}_{\perp j}^* G^*)\Big] \tag{3.127}$$

3.2.3 Electron Axial Coordinates

Longitudinal Position

The definition of $\bar{z}_2$ is

$$\bar{z}_2 = \frac{ct - z}{l_c} \tag{3.128}$$

and the position in $\bar{z}_2$ of the j^{th} electron is

$$\bar{z}_{2j} = 2k_r\rho(ct_j - z) \tag{3.129}$$

Differentiating with respect to z gives

$$\frac{d\bar{z}_{2j}}{dz} = 2k_r\rho(c\frac{dt_j}{dz} - 1) \tag{3.130}$$

$$\frac{d\bar{z}_{2j}}{dz} = 2k_r\rho(\frac{1}{\beta_{zj}} - 1) \tag{3.131}$$

and scaling the differential to $\bar{z}$ gives

$$2k_w\rho\frac{d\bar{z}_{2j}}{d\bar{z}} = 2k_r\rho(\frac{1}{\beta_{zj}} - 1) \tag{3.132}$$

$$\frac{d\bar{z}_{2j}}{d\bar{z}} = \frac{k_r}{k_w}(\frac{1-\beta_{zj}}{\beta_{zj}}) \tag{3.133}$$

$$\frac{d\bar{z}_{2j}}{d\bar{z}} = \frac{1}{\eta}(\frac{1-\beta_{zj}}{\beta_{zj}}) \tag{3.134}$$

$$\frac{d\bar{z}_{2j}}{d\bar{z}} = p_{2j} \tag{3.135}$$

So it is seen that p_{2j} is the rate of change of electron position in the $\bar{z}_2$ frame.

Transverse Coordinates

The momentum in x of the j^{th} electron is defined as

$$p_{xj} = \gamma_j m v_{xj} \tag{3.136}$$

and in scaled units

$$\bar{p}_{xj} = \frac{\gamma_j m v_{xj}}{mc} \tag{3.137}$$

$$\bar{p}_{xj} = \frac{\gamma_j v_{xj}}{c} \tag{3.138}$$

$$\bar{p}_{xj} = \gamma_j\frac{1}{c}\frac{dx_j}{dt} \tag{3.139}$$

and changing the independent variable to z and then scaling to $\bar{z}$

$$\frac{dx_j}{d\bar{z}} = \frac{\bar{p}_{xj}}{2k_w\rho\beta_{zj}\gamma_j} \tag{3.140}$$

Scaling the transverse coordinate x to $\bar{x} = \dfrac{x}{\sqrt{l_g l_c}}$ gives

$$\frac{d\bar{x}_j}{d\bar{z}} = \frac{2\rho\sqrt{k_w k}\bar{p}_{xj}}{2k_w\rho\beta_{zj}\gamma_j} \tag{3.141}$$

$$\frac{d\bar{x}_j}{d\bar{z}} = \frac{\bar{p}_{xj}}{\sqrt{\eta}\beta_{zj}\gamma_j} \tag{3.142}$$

To get to an expression involving p_{2j} instead of γ_j and β_{zj} remember that from the definition of p_{2j}

$$\eta p_{2j} = \frac{1-\beta_{zj}}{\beta_{zj}} \tag{3.143}$$

$$\eta p_{2j} = \frac{1}{\beta_{zj}} - 1 \tag{3.144}$$

$$\frac{1}{\beta_{zj}} = \eta p_{2j} + 1 \tag{3.145}$$

$$\beta_{zj} = \frac{1}{1+\eta p_{2j}} \tag{3.146}$$

Also remember that from the definition of γ_j, in equation (3.124),

$$\frac{1}{\gamma_j^2} = \frac{1-\beta_{zj}^2}{(1+|\bar{p}_{\perp j}|^2)} \tag{3.147}$$

and using (3.146) gives for the numerator of the RHS

$$1-\beta_{zj}^2 = 1 - \left(\frac{1}{1+\eta p_{2j}}\right)^2 \tag{3.148}$$

$$= \frac{(1+\eta p_{2j})^2 - 1}{(1+\eta p_{2j})^2} \tag{3.149}$$

$$= \frac{(1+2\eta p_{2j}+\eta^2 p_{2j}^2) - 1}{(1+\eta p_{2j})^2} \tag{3.150}$$

$$1-\beta_{zj}^2 = \frac{\eta p_{2j}(2+\eta p_{2j})}{(1+\eta p_{2j})^2} \tag{3.151}$$

and using (3.151) in (3.147)

$$\frac{1}{\gamma_j^2} = \frac{\eta p_{2j}(\eta p_{2j}+2)}{(1+|\bar{p}_{\perp j}|^2)(1+\eta p_{2j})^2} \tag{3.152}$$

so that in (3.142), substituting in (3.152) and (3.146),

$$\frac{d\bar{x}_j}{d\bar{z}} = (1+\eta p_{2j})\sqrt{\frac{\eta p_{2j}(\eta p_{2j}+2)}{(1+|\bar{p}_{\perp j}|^2)(1+\eta p_{2j})^2}}\frac{1}{\sqrt{\eta}}\bar{p}_{xj} \tag{3.153}$$

$$\frac{d\bar{x}_j}{d\bar{z}} = \sqrt{\frac{p_{2j}(\eta p_{2j}+2)}{(1+|\bar{p}_{\perp j}|^2)}}\bar{p}_{xj} \tag{3.154}$$

and similarly for $\bar{y}$

$$\frac{d\bar{y}_j}{d\bar{z}} = \sqrt{\frac{p_{2j}(\eta p_{2j}+2)}{(1+|\bar{p}_{\perp j}|^2)}}\bar{p}_{yj} \tag{3.155}$$

3.2.4 Initial Conditions

For a numerical solution the initial electron beam coordinates must be supplied. These are now derived analytically for an initial position along the undulator $\bar{z}$ in the absence of a radiation field.

Initial $\bar{p}_\perp$ conditions

For the initial $\bar{p}_\perp$ condition, ignore the field coupling and focusing terms in (3.224) by forcing $A_\perp = 0$, and integrating over $\bar{z}$ gives

$$\bar{p}_{\perp j0} = \frac{\sqrt{2}}{(f_x^2+f_y^2)^{\frac{1}{2}}}(\bar{a}_w f_x i\sin(\frac{\bar{z}}{2\rho}) - \bar{a}_w f_y\cos(\frac{\bar{z}}{2\rho})) \tag{3.156}$$

So initial conditions for $\bar{p}_\perp$ are

$$\Re(\bar{p}_{\perp j0}) = -\frac{\sqrt{2}\bar{a}_w}{(f_x^2+f_y^2)^{\frac{1}{2}}}f_y\cos(\frac{\bar{z}}{2\rho}) \tag{3.157}$$

$$\Im(\bar{p}_{\perp j0}) = \frac{\sqrt{2}\bar{a}_w}{(f_x^2+f_y^2)^{\frac{1}{2}}}f_x\sin(\frac{\bar{z}}{2\rho}) \tag{3.158}$$

Initial p_2 condition

The definition of p_{2j} is

$$p_{2j} = \frac{1}{\eta}\frac{1-\beta_{zj}}{\beta_{zj}} \tag{3.159}$$

From equation (3.156),

$$|\bar{p}_{\perp j0}|^2 = \bar{p}_{\perp j0}\bar{p}^*_{\perp j0} \tag{3.160}$$

$$|\bar{p}_{\perp j0}|^2 = \frac{2}{f_x^2+f_y^2}\bar{a}_w^2(f_x^2\sin^2(\frac{\bar{z}}{2\rho}) + f_y^2\cos^2(\frac{\bar{z}}{2\rho})) \tag{3.161}$$

We can find β_{zj0} from (3.124)

$$\gamma_{j0}^{-2} = \frac{1-\beta_{zj0}^2}{1+|\bar{p}_{\perp j0}|^2} \tag{3.162}$$

$$\Rightarrow \beta_{zj0} = \sqrt{1-\gamma_{j0}^{-2}(1+|\bar{p}_{\perp j0}|^2)} \tag{3.163}$$

$$\beta_{zj0} = \sqrt{1-\gamma_{j0}^{-2}(1+\frac{2}{f_x^2+f_y^2}\bar{a}_w^2(f_x^2\sin^2(\frac{\bar{z}}{2\rho}) + f_y^2\cos^2(\frac{\bar{z}}{2\rho})))} \tag{3.164}$$

To calculate η use

$$\eta = \frac{1-\bar{\beta}_z}{\bar{\beta}_z} \tag{3.165}$$

where $\bar{\beta}_z$ is β_{zj} averaged along the undulator for a resonant electron given by, from equation (3.164),

$$\bar{\beta}_z = \sqrt{1-\gamma_j^{-2}(1+\frac{2}{f_x^2+f_y^2}\bar{a}_w^2(\frac{f_x^2}{2}+\frac{f_y^2}{2}))} \tag{3.166}$$

$$\bar{\beta}_z = \sqrt{1-\gamma_j^{-2}(1+\bar{a}_w^2)} \tag{3.167}$$

The initial p_{2j} can then be calulated from

$$\eta p_{2j0} = \frac{1-\beta_{zj0}}{\beta_{zj0}} \tag{3.168}$$

$$p_{2j0} = \frac{1}{\eta}\frac{1-\beta_{zj0}}{\beta_{zj0}} \tag{3.169}$$

where β_{zj0} is given by eqn (3.164).

Intitial Transverse Coordinates

Returning to the equation for the transverse $\bar{x}$ coordinate in the form (3.142), inserting initial values (the initial conditions for the transverse momentum from

eqns (3.157) and (3.158)), and integrating over $\bar{z}$,

$$\bar{x}_{j0} = \int \frac{\bar{p}_{x0j}}{\sqrt{\eta}\beta_{zj0}\gamma_{j0}} d\bar{z} \tag{3.170}$$

$$\bar{x}_{j0} = -\frac{1}{\sqrt{\eta}\beta_{zj0}\gamma_{j0}} \frac{\sqrt{2}\bar{a}_w}{(f_x^2 + f_y^2)^{\frac{1}{2}}} f_y \int \cos(\frac{\bar{z}}{2\rho}) d\bar{z} \tag{3.171}$$

$$\bar{x}_{j0} = -\frac{1}{\sqrt{\eta}\beta_{zj0}\gamma_{j0}} \frac{\sqrt{2}\bar{a}_w}{(f_x^2 + f_y^2)^{\frac{1}{2}}} f_y 2\rho \sin(\frac{\bar{z}}{2\rho}) \tag{3.172}$$

$$\bar{x}_{j0} = -\frac{2\sqrt{2}\bar{a}_w\rho}{\sqrt{\eta}\beta_{zj0}\gamma_{j0}(f_x^2 + f_y^2)^{\frac{1}{2}}} f_y \sin(\frac{\bar{z}}{2\rho}) \tag{3.173}$$

and using (3.152) and (3.146) gives

$$\bar{x}_{j0} = -\frac{2\sqrt{2}\bar{a}_w\rho}{(f_x^2 + f_y^2)^{\frac{1}{2}}} \sqrt{\frac{p_{2j0}(\eta p_{2j0} + 2)}{(1 + |\bar{p}_{\perp j0}|^2)}} f_y \sin(\frac{\bar{z}}{2\rho}) \tag{3.174}$$

and similarly for $\bar{y}$

$$\bar{y}_{j0} = \frac{2\sqrt{2}\bar{a}_w\rho}{(f_x^2 + f_y^2)^{\frac{1}{2}}} \sqrt{\frac{p_{2j0}(\eta p_{2j0} + 2)}{(1 + |\bar{p}_{\perp j0}|^2)}} f_x \cos(\frac{\bar{z}}{2\rho}) \tag{3.175}$$

3.3 The Field Equation

The field evolution in the FEL is described by the 3D Maxwell equation in the absence of space charge, given in equation (3.11). In the Compton limit and with the paraxial approximation, the current density $\mathbf{J} = \mathbf{J}_\perp$ where $\mathbf{J}_\perp = J_x\hat{\mathbf{x}} + J_y\hat{\mathbf{y}}$ is the transverse current density, which from N electrons is

$$\mathbf{J}_\perp = -\frac{e}{m} \sum_{j=1}^{N} \frac{\mathbf{p}_{\perp j}}{\gamma_j} \delta^3(x_j, y_j, z_j) \tag{3.176}$$

where $\mathbf{p}_\perp = p_x\hat{\mathbf{x}} + p_y\hat{\mathbf{y}}$ is the perpendicular momentum vector.

Therefore equation (3.11) becomes

$$\nabla^2\mathbf{E} - \frac{1}{c^2}\frac{\partial^2\mathbf{E}}{\partial t^2} = -\frac{\mu_0 e}{m} \sum_{j=1}^{N} \frac{\mathbf{p}_{\perp j}}{\gamma_j} \delta^3(x_j, y_j, z_j) \tag{3.177}$$

where $\delta^3(x_j, y_j, z_j) = \delta(x - x_j(t))\delta(y - y_j(t))\delta(z - z_j(t))$. Obviously only a transverse field with vectors in the x and y dimensions (travelling in the z direction) will arise from this. So projecting the wave equation (3.177) onto $\hat{\mathbf{e}}^*$ gives:

$$\left(\nabla^2 - \frac{1}{c^2}\frac{\partial^2}{\partial t^2}\right) E_\perp = -\frac{\mu_0 e}{m}\sum_{j=1}^{N}\frac{p_{\perp j}}{\gamma_j}\delta^3(x_j, y_j, z_j) \tag{3.178}$$

where $E_\perp = \xi_0 e^{i(kz-\omega t)} = E_x - iE_y$ is the transverse field. Similarly $p_{\perp j} = p_{xj} - ip_{yj}$ is the perpendicular momentum of the jth electron projected over $\hat{\mathbf{e}}^*$.

Defining the independent variables $\bar{z} = 2k_w\rho z$ and $\bar{z}_2 = 2k_w\rho\bar{\beta}_z(ct - z)/(1 - \bar{\beta}_z)$, so that $\frac{\partial}{\partial z} = 2k_w\rho(\frac{\partial}{\partial \bar{z}} - \frac{\bar{\beta}_z}{1-\beta_z}\frac{\partial}{\partial \bar{z}_2})$, $\frac{1}{c}\frac{\partial}{\partial t} = 2k_w\rho\frac{\bar{\beta}_z}{1-\beta_z}\frac{\partial}{\partial \bar{z}_2}$ and $kz - \omega t = -\frac{\bar{z}_2}{2\rho}$, the LHS of (3.178) becomes

$$\frac{\partial^2 E_\perp}{\partial x^2} + \frac{\partial^2 E_\perp}{\partial y^2} + \frac{\partial^2 E_\perp}{\partial z^2} - \frac{1}{c^2}\frac{\partial^2 E_\perp}{\partial t^2} \tag{3.179}$$

$$= \frac{\partial^2 E_\perp}{\partial x^2} + \frac{\partial^2 E_\perp}{\partial y^2} + \left(\frac{\partial}{\partial z} + \frac{1}{c}\frac{\partial}{\partial t}\right)\left(\frac{\partial}{\partial z} - \frac{1}{c}\frac{\partial}{\partial t}\right) E_\perp \tag{3.180}$$

$$= \frac{\partial^2 E_\perp}{\partial x^2} + \frac{\partial^2 E_\perp}{\partial y^2} + \left(2k_w\rho(\frac{\partial}{\partial \bar{z}} - \frac{\bar{\beta}_z}{1-\beta_z}\frac{\partial}{\partial \bar{z}_2}) + 2k_w\rho\frac{\bar{\beta}_z}{1-\beta_z}\frac{\partial}{\partial \bar{z}_2}\right)$$
$$\left(2k_w\rho(\frac{\partial}{\partial \bar{z}} - \frac{\bar{\beta}_z}{1-\beta_z}\frac{\partial}{\partial \bar{z}_2}) - 2k_w\rho\frac{\bar{\beta}_z}{1-\beta_z}\frac{\partial}{\partial \bar{z}_2}\right) E_\perp \tag{3.181}$$

$$= \nabla_\perp^2 E_\perp + (2k_w\rho)^2\left(\frac{\partial}{\partial \bar{z}}\left(\frac{\partial}{\partial \bar{z}} - \frac{2\bar{\beta}_z}{1-\beta_z}\frac{\partial}{\partial \bar{z}_2}\right)\right) E_\perp \tag{3.182}$$

Changing the delta function from $z \to t \to \bar{z}_2$ [41],

$$\delta(z - \bar{z}_j) = \frac{1}{\beta_{zj}} 2k_w\rho\frac{\bar{\beta}_z}{1-\bar{\beta}_z}\delta(\bar{z}_2 - \bar{z}_{2j}) \tag{3.183}$$

and applying the scaling from $z, t \to \bar{z}, \bar{z}_2$ to the rest of the RHS of equation (3.178) gives

$$-\frac{\mu_0 e}{m}\frac{\partial}{\partial t}\sum_{j=1}^{N}\frac{p_{\perp j}}{\gamma_j}\delta(x - x_j)\delta(y - y_j)\delta(t - t_j) \tag{3.184}$$

$$= -\frac{\mu_0 e}{m}(2ck_w\rho\frac{\bar{\beta}_z}{1-\beta_z})\frac{\partial}{\partial \bar{z}_2}$$
$$\sum_{j=1}^{N}\frac{p_{\perp j}}{\gamma_j}\frac{1}{\beta_{zj}} 2k_w\rho\frac{\bar{\beta}_z}{1-\bar{\beta}_z}\delta(x - x_j)\delta(y - y_j)\delta(\bar{z}_2 - \bar{z}_{2j}) \tag{3.185}$$

and the full field equation is now:

$$\nabla_{\perp}^2 E_{\perp} + (2k_w\rho)^2 \left(\frac{\partial}{\partial \bar{z}} \left(\frac{\partial}{\partial \bar{z}} - \frac{2\bar{\beta}_z}{1-\beta_z} \frac{\partial}{\partial \bar{z}_2} \right) \right) E_{\perp} =$$
$$- \frac{e}{\epsilon_0 mc} 4k_w^2 \rho^2 \Big(\frac{\bar{\beta}_z}{1-\bar{\beta}_z} \Big)^2 \frac{\partial}{\partial \bar{z}_2} \sum_{j=1}^{N} \frac{p_{\perp j}}{\beta_{zj}\gamma_j} \delta^3(x_j, y_j, \bar{z}_{2j}) \tag{3.186}$$

$$\Rightarrow \frac{1}{(2k_w\rho)^2} \nabla_{\perp}^2 E_{\perp} + \left(\frac{\partial}{\partial \bar{z}} \left(\frac{\partial}{\partial \bar{z}} - \frac{2\bar{\beta}_z}{1-\bar{\beta}_z} \frac{\partial}{\partial \bar{z}_2} \right) \right) E_{\perp} =$$
$$- \frac{e}{\epsilon_0 mc} \Big(\frac{\bar{\beta}_z}{1-\bar{\beta}_z} \Big)^2 \frac{\partial}{\partial \bar{z}_2} \sum_{j=1}^{N} \frac{p_{\perp j}}{\beta_{zj}\gamma_j} \delta^3(x_j, y_j, \bar{z}_{2j}) \tag{3.187}$$

Neglecting the backwards wave by applying the approximation in section 3.1.3, which is

$$\left| \frac{\partial E_{\perp}}{\partial \bar{z}} \right| \ll \left| \frac{\bar{\beta}_z}{1-\bar{\beta}_z} \frac{\partial E_{\perp}}{\partial \bar{z}_2} \right| \tag{3.188}$$

gives

$$\frac{1}{(2k_w\rho)^2} \nabla_{\perp}^2 E_{\perp} - \frac{2\bar{\beta}_z}{1-\beta_z} \frac{\partial^2}{\partial \bar{z} \partial \bar{z}_2} E_{\perp} =$$
$$- \frac{e}{\epsilon_0 mc} \Big(\frac{\bar{\beta}_z}{1-\bar{\beta}_z} \Big)^2 \frac{\partial}{\partial \bar{z}_2} \sum_{j=1}^{N} \frac{p_{\perp j}}{\beta_{zj}\gamma_j} \delta^3(x_j, y_j, \bar{z}_{2j}) \tag{3.189}$$

Factoring $\dfrac{\bar{\beta}_z}{1-\bar{\beta}_z}$,

$$\frac{1}{(2k_w\rho)^2} \frac{1-\bar{\beta}_z}{\bar{\beta}_z} \nabla_{\perp}^2 E_{\perp} - \frac{2\partial^2}{\partial \bar{z} \partial \bar{z}_2} E_{\perp} =$$
$$- \frac{e}{\epsilon_0 mc} \frac{\bar{\beta}_z}{1-\bar{\beta}_z} \frac{\partial}{\partial \bar{z}_2} \sum_{j=1}^{N} \frac{p_{\perp j}}{\beta_{zj}\gamma_j} \delta^3(x_j, y_j, \bar{z}_{2j}) \tag{3.190}$$

and applying the resonance condition, $\dfrac{1-\bar{\beta}_z}{\bar{\beta}_z} = \dfrac{\lambda_r}{\lambda_w} = \dfrac{k_w}{k_r}$,

$$\frac{1}{4k_w k_r \rho^2} \nabla_{\perp}^2 E_{\perp} - \frac{2\partial^2}{\partial \bar{z} \partial \bar{z}_2} E_{\perp} =$$
$$- \frac{e}{\epsilon_0 mc} \frac{\bar{\beta}_z}{1-\bar{\beta}_z} \frac{\partial}{\partial \bar{z}_2} \sum_{j=1}^{N} \frac{p_{\perp j}}{\beta_{zj}\gamma_j} \delta^3(x_j, y_j, \bar{z}_{2j}) \tag{3.191}$$

Scaling x by $\bar{x} = \dfrac{x}{\sqrt{l_g l_c}}$ (and the same for y), and remembering $l_g = \dfrac{1}{2k_w\rho}$ and $l_c = \dfrac{1}{2k_r\rho}$,

$$\begin{aligned} LHS =& \frac{1}{4k_w k_r \rho^2}\left(\frac{\partial^2}{\partial x^2} + \frac{\partial^2}{\partial y^2}\right) E_\perp - \frac{2\partial^2}{\partial \bar{z}\partial \bar{z}_2} E_\perp \\ =& \frac{1}{4k_w k_r \rho^2}\frac{1}{l_g l_c}\left(\frac{\partial^2}{\partial \bar{x}^2} + \frac{\partial^2}{\partial \bar{y}^2}\right) E_\perp - \frac{2\partial^2}{\partial \bar{z}\partial \bar{z}_2} E_\perp \\ =& \frac{1}{4k_w k_r \rho^2} 4k_w k_r \rho^2 \left(\frac{\partial^2}{\partial \bar{x}^2} + \frac{\partial^2}{\partial \bar{y}^2}\right) E_\perp - \frac{2\partial^2}{\partial \bar{z}\partial \bar{z}_2} E_\perp \\ =& \left(\frac{\partial^2}{\partial \bar{x}^2} + \frac{\partial^2}{\partial \bar{y}^2}\right) E_\perp - \frac{2\partial^2}{\partial \bar{z}\partial \bar{z}_2} E_\perp \end{aligned} \tag{3.192}$$

and the RHS

$$= - \frac{e}{\epsilon_0 mc}\frac{\bar{\beta}_z}{1-\bar{\beta}_z}\frac{\partial}{\partial \bar{z}_2}\sum_{j=1}^{N}\frac{p_{\perp j}}{\beta_{zj}\gamma_j}\frac{1}{l_g l_c}\delta^3(\bar{x}_j, \bar{y}_j, \bar{z}_{2j}) \tag{3.193}$$

as $\delta(x - x_j) = \dfrac{1}{\sqrt{l_g l_c}}\delta(\bar{x} - \bar{x}_j)$.

So the full equation is now:

$$\begin{aligned} &\left(\frac{\partial^2}{\partial \bar{x}^2} + \frac{\partial^2}{\partial \bar{y}^2}\right) E_\perp - \frac{2\partial^2}{\partial \bar{z}\partial \bar{z}_2} E_\perp = \\ &- \frac{e}{\epsilon_0 mc}\frac{\bar{\beta}_z}{1-\bar{\beta}_z}\frac{1}{l_g l_c}\frac{\partial}{\partial \bar{z}_2}\sum_{j=1}^{N}\frac{p_{\perp j}}{\beta_{zj}\gamma_j}\delta^3(\bar{x}_j, \bar{y}_j, \bar{z}_{2j}) \end{aligned} \tag{3.194}$$

Further scaling, $\bar{p}_\perp = \dfrac{p_\perp}{mc}$ and $\eta = \dfrac{1-\bar{\beta}_z}{\bar{\beta}_z}$, seen in the table in figure 3.2, and $\dfrac{1}{\gamma_j} = \left(\dfrac{1-\beta_{zj}^2}{1+|\bar{p}_{\perp j}|^2}\right)^{\frac{1}{2}}$ which was derived in equation (3.124), so that

$$\frac{1}{\beta_{zj}\gamma_j} = \left(\frac{1-\beta_{zj}^2}{\beta_{zj}^2(1+|\bar{p}_{\perp j}|^2)}\right)^{\frac{1}{2}} \tag{3.195}$$

$$\Rightarrow \frac{1}{\beta_{zj}\gamma_j} = \left(\frac{1}{(1+|\bar{p}_{\perp j}|^2)}\left(\frac{1}{\beta_{zj}^2} - 1\right)\right)^{\frac{1}{2}} \tag{3.196}$$

Now

$$\eta p_{2j} = \frac{1-\beta_{zj}}{\beta_{zj}} \tag{3.197}$$

$$\eta p_{2j} = \frac{1}{\beta_{zj}} - 1 \tag{3.198}$$

$$\frac{1}{\beta_{zj}} = \eta p_{2j} + 1 \tag{3.199}$$

so that in (3.196)

$$\frac{1}{\beta_{zj}\gamma_j} = \left(\frac{1}{(1+|\bar{p}_{\perp j}|^2)} \left((\eta p_{2j}+1)^2 - 1 \right) \right)^{\frac{1}{2}} \tag{3.200}$$

$$\Rightarrow \frac{1}{\beta_{zj}\gamma_j} = \left(\frac{1}{(1+|\bar{p}_{\perp j}|^2)} \left((\eta^2 p_{2j}^2 + 2\eta p_{2j} + 1) - 1 \right) \right)^{\frac{1}{2}} \tag{3.201}$$

$$\Rightarrow \frac{1}{\beta_{zj}\gamma_j} = \left(\frac{1}{(1+|\bar{p}_{\perp j}|^2)} \left(\eta p_{2j}(\eta p_{2j}+2) \right) \right)^{\frac{1}{2}} \tag{3.202}$$

Simpifying (3.194) gives

$$\left(\frac{\partial^2}{\partial \bar{x}^2} + \frac{\partial^2}{\partial \bar{y}^2} \right) E_\perp - \frac{2\partial^2}{\partial \bar{z} \partial \bar{z}_2} E_\perp =$$
$$- \frac{e}{\epsilon_0 \eta l_g l_c} \frac{\partial}{\partial \bar{z}_2} \sum_{j=1}^{N} \frac{\bar{p}_{\perp j}}{\sqrt{1+|\bar{p}_{\perp j}|}} \sqrt{\eta p_{2j}(\eta p_{2j}+2)} \delta^3(\bar{x}_j, \bar{y}_j, \bar{z}_{2j}) \tag{3.203}$$

Scaling from $E_\perp \rightarrow A_\perp$ by using the definition in figure 3.2,

$$A_\perp = \frac{e\sqrt{f_x^2 + f_y^2}}{\sqrt{2} mc\omega_p \sqrt{\gamma_r \rho}} E_\perp \tag{3.204}$$

gives

$$\left(\frac{\partial^2}{\partial \bar{x}^2} + \frac{\partial^2}{\partial \bar{y}^2} \right) A_\perp - \frac{2\partial^2}{\partial \bar{z} \partial \bar{z}_2} A_\perp =$$
$$- \sqrt{\frac{f_x^2 + f_y^2}{2}} \frac{e^2}{\epsilon_0 \eta l_g l_c mc\omega_p \sqrt{\gamma_r \rho}} \frac{\partial}{\partial \bar{z}_2} \sum_{j=1}^{N} \frac{\bar{p}_{\perp j}}{\sqrt{1+|\bar{p}_{\perp j}|}} \sqrt{\eta p_{2j}(\eta p_{2j}+2)} \delta^3(\bar{x}_j, \bar{y}_j, \bar{z}_{2j}) \tag{3.205}$$

Using the definition of ρ, which is

$$\rho = \frac{1}{\gamma_r}\left(\frac{\bar{a}_w\omega_p}{4ck_w}\right)^{2/3} \tag{3.206}$$

and and rearranging for

$$\omega_p = \frac{4ck_w(\gamma_r\rho)^{3/2}}{\bar{a}_w} \tag{3.207}$$

and also

$$\frac{1}{\gamma_r\rho} = \left(\frac{4ck_w}{\omega_p\bar{a}_w}\right)^{2/3} \tag{3.208}$$

$$\frac{1}{\gamma_r^3\rho^3} = \left(\frac{4ck_w}{\omega_p\bar{a}_w}\right)^{2} \tag{3.209}$$

$$\frac{1}{\gamma_r^2\rho^2} = \gamma_r\rho\left(\frac{4ck_w}{\omega_p\bar{a}_w}\right)^{2} \tag{3.210}$$

$$\tag{3.211}$$

Substituting into the field equation (3.205) gives

$$\left(\frac{\partial^2}{\partial\bar{x}^2}+\frac{\partial^2}{\partial\bar{y}^2}\right)A_\perp - \frac{2\partial^2}{\partial\bar{z}\partial\bar{z}_2}A_\perp = -\sqrt{\frac{f_x^2+f_y^2}{2}}\frac{e^2}{\epsilon_0\eta l_g l_c mc}\frac{\bar{a}_w}{4ck_w(\gamma_r\rho)^2}\times$$
$$\frac{\partial}{\partial\bar{z}_2}\sum_{j=1}^{N}\frac{\bar{p}_{\perp j}}{\sqrt{1+|\bar{p}_{\perp j}|}}\sqrt{\eta p_{2j}(\eta p_{2j}+2)}\delta^3(\bar{x}_j,\bar{y}_j,\bar{z}_{2j}) \tag{3.212}$$

$$\Rightarrow\left(\frac{\partial^2}{\partial\bar{x}^2}+\frac{\partial^2}{\partial\bar{y}^2}\right)A_\perp - \frac{2\partial^2}{\partial\bar{z}\partial\bar{z}_2}A_\perp = -\sqrt{\frac{f_x^2+f_y^2}{2}}\frac{e^2}{\epsilon_0\eta l_g l_c mc}\gamma_r\rho\frac{4ck_w}{\omega_p^2\bar{a}_w}\times$$
$$\frac{\partial}{\partial\bar{z}_2}\sum_{j=1}^{N}\frac{\bar{p}_{\perp j}}{\sqrt{1+|\bar{p}_{\perp j}|}}\sqrt{\eta p_{2j}(\eta p_{2j}+2)}\delta^3(\bar{x}_j,\bar{y}_j,\bar{z}_{2j}) \tag{3.213}$$

Now substitute for the plasma frequency

$$\frac{1}{\omega_p} = \sqrt{\frac{\epsilon_0 m}{e^2 n_p}}, \tag{3.214}$$

where n_p is the peak electron number density, then

$$\left(\frac{\partial^2}{\partial\bar{x}^2}+\frac{\partial^2}{\partial\bar{y}^2}\right)A_\perp-\frac{2\partial^2}{\partial\bar{z}\partial\bar{z}_2}A_\perp=-\sqrt{\frac{f_x^2+f_y^2}{2}}\frac{e^2}{\epsilon_0\eta l_g l_c mc}\gamma_r\rho\frac{4ck_w}{\bar{a}_w}\frac{\epsilon_0 m}{e^2 n_p}\times$$
$$\frac{\partial}{\partial\bar{z}_2}\sum_{j=1}^{N}\frac{\bar{p}_{\perp j}}{\sqrt{1+|\bar{p}_{\perp j}|}}\sqrt{\eta p_{2j}(\eta p_{2j}+2)}\delta^3(\bar{x}_j,\bar{y}_j,\bar{z}_{2j}) \tag{3.215}$$

$$\Rightarrow\left(\frac{\partial^2}{\partial\bar{x}^2}+\frac{\partial^2}{\partial\bar{y}^2}\right)A_\perp-\frac{2\partial^2}{\partial\bar{z}\partial\bar{z}_2}A_\perp=-\sqrt{\frac{f_x^2+f_y^2}{2}}\frac{4k_w\gamma_r\rho}{\eta l_g l_c\bar{a}_w n_p}\times$$
$$\frac{\partial}{\partial\bar{z}_2}\sum_{j=1}^{N}\frac{\bar{p}_{\perp j}}{\sqrt{1+|\bar{p}_{\perp j}|}}\sqrt{\eta p_{2j}(\eta p_{2j}+2)}\delta^3(\bar{x}_j,\bar{y}_j,\bar{z}_{2j}) \tag{3.216}$$

Introducing the scaled electron density, which is defined from the scaling of $\bar{x}$, $\bar{y}$ and $\bar{z}_2$,

$$\bar{n}_p=l_g l_c^2 n_p \tag{3.217}$$

gives:

$$\left(\frac{\partial^2}{\partial\bar{x}^2}+\frac{\partial^2}{\partial\bar{y}^2}\right)A_\perp-\frac{2\partial^2}{\partial\bar{z}\partial\bar{z}_2}A_\perp=$$
$$-\sqrt{\frac{f_x^2+f_y^2}{2}}\frac{4k_w\gamma_r\rho l_g l_c^2}{\eta l_g l_c\bar{a}_w\bar{n}_p}\frac{\partial}{\partial\bar{z}_2}\sum_{j=1}^{N}\frac{\bar{p}_{\perp j}}{\sqrt{1+|\bar{p}_{\perp j}|}}\sqrt{\eta p_{2j}(\eta p_{2j}+2)}\delta^3(\bar{x}_j,\bar{y}_j,\bar{z}_{2j}) \tag{3.218}$$

$$\left(\frac{\partial^2}{\partial\bar{x}^2}+\frac{\partial^2}{\partial\bar{y}^2}\right)A_\perp-\frac{2\partial^2}{\partial\bar{z}\partial\bar{z}_2}A_\perp=$$
$$-\sqrt{\frac{f_x^2+f_y^2}{2}}\frac{4k_w\gamma_r\rho l_c}{\eta\bar{a}_w\bar{n}_p}\frac{\partial}{\partial\bar{z}_2}\sum_{j=1}^{N}\frac{\bar{p}_{\perp j}}{\sqrt{1+|\bar{p}_{\perp j}|}}\sqrt{\eta p_{2j}(\eta p_{2j}+2)}\delta^3(\bar{x}_j,\bar{y}_j,\bar{z}_{2j}) \tag{3.219}$$

$$\left(\frac{\partial^2}{\partial\bar{x}^2}+\frac{\partial^2}{\partial\bar{y}^2}\right)A_\perp-\frac{2\partial^2}{\partial\bar{z}\partial\bar{z}_2}A_\perp=$$
$$-\sqrt{\frac{f_x^2+f_y^2}{2}}\frac{4k_w\gamma_r\rho}{\eta\bar{a}_w\bar{n}_p 2\rho k}\frac{\partial}{\partial\bar{z}_2}\sum_{j=1}^{N}\frac{\bar{p}_{\perp j}}{\sqrt{1+|\bar{p}_{\perp j}|}}\sqrt{\eta p_{2j}(\eta p_{2j}+2)}\delta^3(\bar{x}_j,\bar{y}_j,\bar{z}_{2j}) \tag{3.220}$$

$$\left(\frac{\partial^2}{\partial\bar{x}^2}+\frac{\partial^2}{\partial\bar{y}^2}\right)A_\perp-\frac{2\partial^2}{\partial\bar{z}\partial\bar{z}_2}A_\perp=$$
$$-\sqrt{\frac{f_x^2+f_y^2}{2}}\frac{2\gamma_r}{\bar{a}_w\bar{n}_p}\frac{1}{\eta}\frac{k_w}{k}\frac{\partial}{\partial\bar{z}_2}\sum_{j=1}^{N}\frac{\bar{p}_{\perp j}}{\sqrt{1+|\bar{p}_{\perp j}|}}\sqrt{\eta p_{2j}(\eta p_{2j}+2)}\delta^3(\bar{x}_j,\bar{y}_j,\bar{z}_{2j}) \tag{3.221}$$

$$\Rightarrow\left(\frac{\partial^2}{\partial\bar{x}^2}+\frac{\partial^2}{\partial\bar{y}^2}\right)A_\perp-\frac{2\partial^2}{\partial\bar{z}\partial\bar{z}_2}A_\perp=$$
$$-\sqrt{\frac{f_x^2+f_y^2}{2}}\frac{2\gamma_r}{\bar{a}_w\bar{n}_p}\frac{\partial}{\partial\bar{z}_2}\sum_{j=1}^{N}\frac{\bar{p}_{\perp j}}{\sqrt{1+|\bar{p}_{\perp j}|}}\sqrt{\eta p_{2j}(\eta p_{2j}+2)}\delta^3(\bar{x}_j,\bar{y}_j,\bar{z}_{2j}) \tag{3.222}$$

3.4 Final Equations

To summarize, the final set of scaled working equations describing the FEL interaction are then

$$\left(\frac{\partial^2}{\partial\bar{x}^2}+\frac{\partial^2}{\partial\bar{y}^2}\right)A_\perp-\frac{2\partial^2}{\partial\bar{z}\partial\bar{z}_2}A_\perp= -\frac{2\gamma_r}{a_w\bar{n}_p}\frac{\partial}{\partial\bar{z}_2}\sum_{j=1}^{N}\frac{\bar{p}_{\perp j}\sqrt{\eta p_{2j}(\eta p_{2j}+2)}}{\sqrt{1+|\bar{p}_{\perp j}|}}\delta^3(\bar{x}_j,\bar{y}_j,\bar{z}_{2j}) \tag{3.223}$$

$$\frac{d\bar{p}_{\perp j}}{d\bar{z}}=\frac{a_w}{2\rho}\Big(iG^*-\frac{\eta p_{2j}}{f^2\bar{k}_\beta^2}A_{\perp j}\Big)+F_j \tag{3.224}$$

$$\frac{dp_{2j}}{d\bar{z}}=\frac{a_w}{4\rho}\left(\frac{p_{2j}(\eta p_{2j}+2)}{1+|\bar{p}_{\perp j}|^2}\right)\Big[\frac{\eta p_{2j}}{f^2\bar{k}_\beta^2}(\bar{p}_\perp E^*_{\perp j}+\bar{p}^*_{\perp j}E_{\perp j}) -i(\eta p_{2j}+1)(\bar{p}_{\perp j}G-\bar{p}^*_{\perp j}G^*)\Big] \tag{3.225}$$

$$\frac{d\bar{z}_{2j}}{d\bar{z}}=p_{2j} \tag{3.226}$$

$$\frac{d\bar{x}_j}{d\bar{z}}=\sqrt{\frac{p_{2j}(2+\eta p_{2j})}{1+|\bar{p}_{\perp j}|^2}}\Re(\bar{p}_{\perp j}) \tag{3.227}$$

$$\frac{d\bar{y}_j}{d\bar{z}}=-\sqrt{\frac{p_{2j}(2+\eta p_{2j})}{1+|\bar{p}_{\perp j}|^2}}\Im(\bar{p}_{\perp j}) \tag{3.228}$$

where $F_j=-\gamma_j\beta_{zj}\bar{k}_\beta^2\sqrt{\eta}(\bar{x}_j-i\bar{y}_j)$ is the focusing term. The peak undulator parameter $a_w=\dfrac{\sqrt{2}\bar{a}_w}{\sqrt{f_x^2+f_y^2}}$ is now used in the equations to get rid of the factors of $\sqrt{f_x^2+f_y^2}$ common to the $A_\perp, p_\perp$ and p_2 equations. The delta function is once again represented by $\delta^3(\bar{x}_j,\bar{y}_j,\bar{z}_{2j})=\delta(\bar{x}-\bar{x}_j)\delta(\bar{y}-\bar{y}_j)\delta(\bar{z}_2-\bar{z}_{2j})$ for brevity.

The working equations are now subjected to analysis to allow them to be solved numerically.

Chapter 4

Numerical Solution

4.1 Introduction

To solve the equations numerically, a number of further changes to the equations derived in the last chapter must be made. The electron beam is discretised into electron macro-particles each representing many electrons. The field is discretised into a finite number of nodes.

The field equation is solved by use of the split-step Fourier method [44], which splits each step forward in $\bar{z}$ into two half-steps: the first step deals with field diffraction only; in the second, the field is driven by the source term in the absence of diffraction. The electron equations are driven by the field source term using the 4^{th} order Runge-Kutta (RK4) method.

4.2 Numerical Field Solution

The field equation is written as

$$2\frac{\partial^2 A_\perp}{\partial\bar{z}\partial\bar{z}_2} = \frac{\partial^2 A_\perp}{\partial\bar{x}^2} + \frac{\partial^2 A_\perp}{\partial\bar{y}^2} + \frac{2\gamma_r}{a_w\bar{n}_p}\frac{\partial}{\partial\bar{z}_2}\sum_{j=1}^{N}\frac{\bar{p}_{\perp j}(\eta p_{2j}(\eta p_{2j}+2))^{1/2}}{(1+|\bar{p}_{\perp j}|^2)^{1/2}}\delta^3(\bar{x}_j,\bar{y}_j,\bar{z}_{2j}) \tag{4.1}$$

$$2\frac{\partial^2 A_\perp}{\partial\bar{z}\partial\bar{z}_2} = D + S \tag{4.2}$$

where $D = \frac{\partial^2 A_\perp}{\partial \bar{x}^2} + \frac{\partial^2 A_\perp}{\partial \bar{y}^2}$ is the diffraction term and S is the source term. This can be solved numerically by solving the diffraction and source terms separately within one full numerical integration step. This technique is the Split Step Fourier Method, and is a form of operator splitting.

First of all, the diffraction term is solved by letting the source term = 0, so

$$2\frac{\partial^2 A_\perp}{\partial \bar{z} \partial \bar{z}_2} = D \tag{4.3}$$

and then the source term is solved by

$$2\frac{\partial^2 A_\perp}{\partial \bar{z} \partial \bar{z}_2} = S \tag{4.4}$$

The following outlines these two steps in detail.

4.2.1 Field Diffraction

The diffraction equation is

$$2\frac{\partial^2 A_\perp}{\partial \bar{z} \partial \bar{z}_2} = \frac{\partial^2 A_\perp}{\partial \bar{x}^2} + \frac{\partial^2 A_\perp}{\partial \bar{y}^2} \tag{4.5}$$

which can be solved using Fourier transforms.

Fourier transforming $A_\perp(\bar{x}, \bar{y}, \bar{z}, \bar{z}_2) \rightarrow A'_\perp(k_x, k_y, \bar{z}, \bar{z}_2)$ in $\bar{x}$ and $\bar{y}$ so that $\frac{\partial}{\partial \bar{x}} \rightarrow ik_x$ and $\frac{\partial}{\partial \bar{y}} \rightarrow ik_y$ gives

$$2\frac{\partial^2 A'_\perp}{\partial \bar{z} \partial \bar{z}_2} = -(k_x^2 + k_y^2) A'_\perp \tag{4.6}$$

Then, similarly, transforming from $A'_{\perp}(k_x, k_y, \bar{z}, \bar{z}_2) \rightarrow \tilde{A}_{\perp}(k_x, k_y, \bar{z}, k_{z2})$ gives

$$2ik_{z2}\frac{\partial \tilde{A}_{\perp}}{\partial \bar{z}} = -(k_x^2 + k_y^2)\tilde{A}_{\perp} \tag{4.7}$$

$$\frac{\partial \tilde{A}_{\perp}}{\partial \bar{z}} = \frac{-(k_x^2 + k_y^2)}{2ik_{z2}}\tilde{A}_{\perp} \tag{4.8}$$

$$\frac{\partial \tilde{A}_{\perp}}{\partial \bar{z}} = \frac{i(k_x^2 + k_y^2)}{2k_{z2}}\tilde{A}_{\perp} \tag{4.9}$$

$$\frac{\partial \tilde{A}_{\perp}}{\tilde{A}_{\perp}} = \frac{i(k_x^2 + k_y^2)}{2k_{z2}}\partial \bar{z} \tag{4.10}$$

$$\int \frac{1}{\tilde{A}_{\perp}} d\tilde{A}_{\perp} = \int \frac{i(k_x^2 + k_y^2)}{2k_{z2}} d\bar{z} \tag{4.11}$$

$$\ln \tilde{A}_{\perp} = \frac{i(k_x^2 + k_y^2)}{2k_{z2}}\bar{z} + \ln \tilde{A}_{\perp 0} \tag{4.12}$$

Replacing the propagation distance $\bar{z}$ with the step size h gives

$$\tilde{A}_{\perp}(k_x, k_y, k_{z2}, \bar{z} + h) = \tilde{A}_{\perp}(k_x, k_y, k_{z2}, \bar{z}) \exp\left(\frac{ih(k_x^2 + k_y^2)}{2k_{z2}}\right) \tag{4.13}$$

This is the solution for the diffraction step.

4.2.2 Field Source Term

The field equation driven by the electron source is:

$$2\frac{\partial^2 A_{\perp}}{\partial \bar{z} \partial \bar{z}_2} = \frac{2\gamma_r}{a_w \bar{n}_p}\frac{\partial}{\partial \bar{z}_2}\sum_{j=1}^{N}\frac{\bar{p}_{\perp j}(\eta p_{2j}(\eta p_{2j} + 2))^{1/2}}{(1 + |\bar{p}_{\perp j}|^2)^{1/2}}\delta^3(\bar{x}_j, \bar{y}_j, \bar{z}_{2j}) \tag{4.14}$$

This can be expressed as

$$\frac{\partial}{\partial \bar{z}_2}\left[\frac{\partial A_{\perp}}{\partial \bar{z}} - \frac{\gamma_r}{a_w \bar{n}_p}\sum_{j=1}^{N}\frac{\bar{p}_{\perp j}(\eta p_{2j}(\eta p_{2j} + 2))^{1/2}}{(1 + |\bar{p}_{\perp j}|^2)^{1/2}}\delta^3(\bar{x}_j, \bar{y}_j, \bar{z}_{2j})\right] = 0 \tag{4.15}$$

The solution to the bracketed term must in a general form be a function of $\bar{z}$ plus a constant. Due to energy conservation, the solution must $= 0$ so that

$$\frac{\partial A_{\perp}}{\partial \bar{z}} = \frac{\gamma_r}{a_w \bar{n}_p}\sum_{j=1}^{N}\frac{\bar{p}_{\perp j}(\eta p_{2j}(\eta p_{2j} + 2))^{1/2}}{(1 + |\bar{p}_{\perp j}|^2)^{1/2}}\delta^3(\bar{x}_j, \bar{y}_j, \bar{z}_{2j}) \tag{4.16}$$

The sum in (4.16) is still over the N electrons in the pulse. This is now simplified to allow a sum over a number of macroparticles N_m with $N_m \ll N$. The electron beam is discretised in 6 dimensions (3 spatial and 3 momentum).

Electron Beam Discretisation

There are N real electrons in the system, which are to be represented by $N_m \ll N$ macro-electrons. In total the beam is sampled in 6 dimensions, 3 spatial $(\bar{x}, \bar{y}, \bar{z}_2)$ and 3 momenta $(\bar{p}_x, \bar{p}_y, p_{z2})$. The sampling is performed and the noise added statistically according to the algorithm of [45].

Each macroelectron represents N_k real electrons which collectively have a mean position and momentum equal to the position and momentum of the macroparticle.

This is achieved in equation (4.16) by replacing the sum over the real electrons with a sum over the macroelectrons,

$$\sum_{j=1}^{N} f(\mathbf{x}_j, \mathbf{p}_j) = \sum_{k=1}^{N_m} \sum_{i=1}^{N_k} f(\mathbf{x}_{k,i}, \mathbf{p}_{k,i}) \tag{4.17}$$

where f is a function of the particle coordinates in phase space. The first sum on the RHS is over the N_m macroelectrons, and the second sum is over the N_k real electrons represented by the k^{th} macroparticle.

As the position-momentum coordinate of each macroparticle is the mean of the real electrons it represents, it can be said that

$$\sum_{j=1}^{N} f(\mathbf{x}_j, \mathbf{p}_j) = \sum_{k=1}^{N_m} N_k f(\mathbf{x}_k, \mathbf{p}_k) \tag{4.18}$$

The peak electron density $\bar{n}_p$ multiplied by a volume element V_k of the electron beam which the kth macroelectron represents gives the number of electrons in the most dense electron beam element. Defining a weighting factor χ_k such that $0 \leq \chi_k \leq 1$ means that the number of electrons N_k represented by the kth macroelectron can be defined as

$$N_k = \chi_k \bar{n}_p V_k \tag{4.19}$$

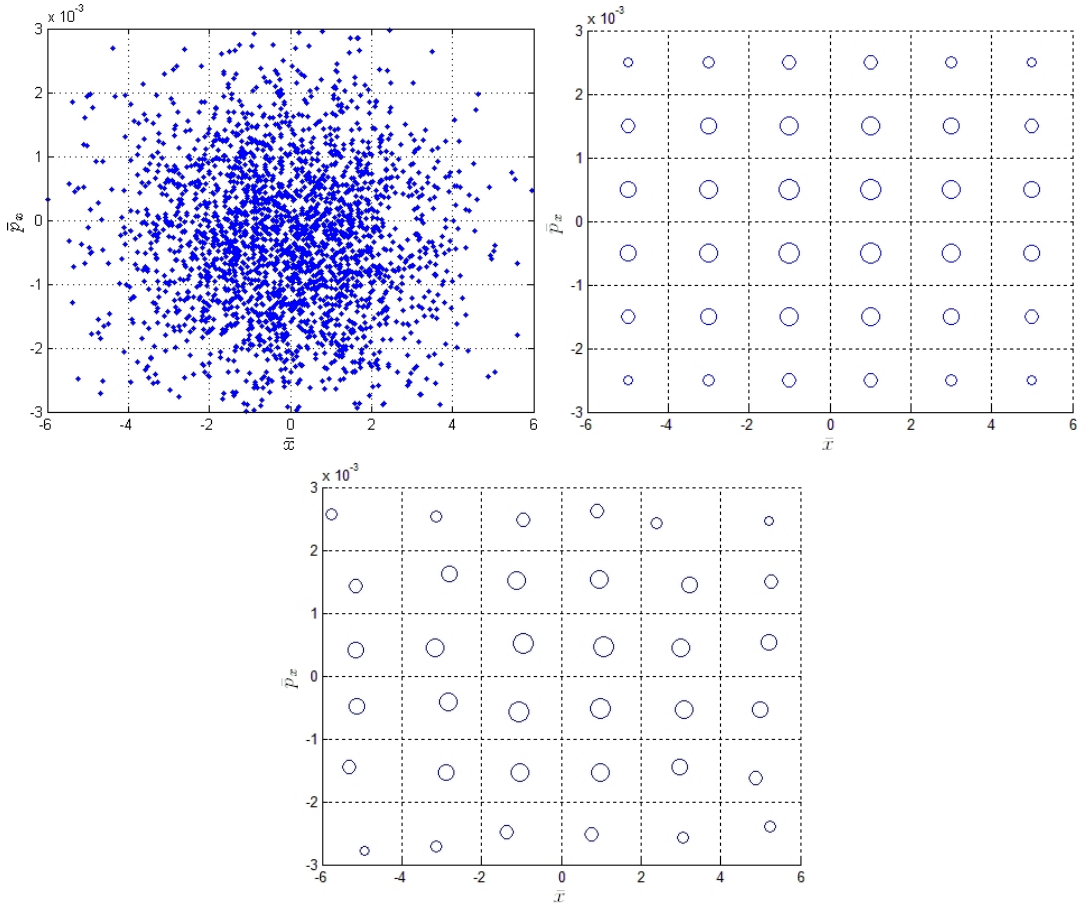

Figure 4.1: A series of plots showing the electron beam discretization process. The top left plot shows the real electrons in x vs p_x. The second plot shows the initial distribution of macroparticles. The bottom plot show the final result with noise added.

where the weighting factor χ_k can be given the desired distribution, with a peak value of 1, in $\mathbf{x}$ and $\mathbf{p}$.

The discretization process is shown for a Gaussian distribution in figure 4.1. The top left shows a typical electron distribution in phase space. The electrons have a Gaussian distribution in x and p_x, with noise. To discretize this, an equi-spaced grid is overlayed, shown with dashed lines. Each element has dimensions Δx by Δp_x. Into the center of each grid element a macro-particle is placed which will represent all the real electrons within that element.

To generate the macro-electrons in the code, first the distribution of weighted

χ values are created. Each macroparticle's χ value is the fraction of electrons it represents compared to the element with the most electrons. In this case it is wished that a Gaussian distribution is modelled, so the χ values are assigned with a Gaussian distribution in x and p_x. The plot on the top right shows the macro-particles initialized in the center of their grid element, and their size is proportional to their χ weighting factor. The noise is then added by Poisson statistics [45], so the "larger" macroelectrons are varied less than those representing a smaller number of real electrons. The noise is added to both the χ value and the position in x and p_x. The noise has been added in the bottom plot. Note that this illustration is in the $\bar{x}$ phase space of one direction. In the code the same process occurs in all 3 ordinates, which is to say, a 6-dimensional phase space.

Using (4.18) and (4.19), the driven field equation (4.16) becomes

$$\frac{\partial A_\perp}{\partial \bar{z}} = \frac{\gamma_r}{a_w} \sum_{k=1}^{N_m} \bar{\chi}_k \frac{\bar{p}_{\perp k}(\eta p_{2k}(\eta p_{2k}+2))^{1/2}}{(1+|\bar{p}_{\perp k}|^2)^{1/2}} \delta^3(\bar{x}_k, \bar{y}_k, \bar{z}_{2k}) \tag{4.20}$$

where $\bar{\chi}_k = \chi_k V_k$.

The electrons have been discretised, and now the field must represented by a finite number of sample points.

Field Discretisation

The field can be represented by a 3-dimensional grid with a linear interpolant. Two different methods to solve this were attempted. A solution involving Fourier transforms, presented in [46] and included in appendix A, solved the source term in Fourier space, and led to a relatively easy method of parallelization of the numerical integration. This method was limited, however, by the large number of calculations needed: every electron must interact with every node in Fourier space. With a 3-dimensional field and 6-dimensional electron beam, the number of calculations is prohibitive. For example, a relatively small system may have $64 \times 64 \times 2000$ field nodes in $\bar{x}, \bar{y}$ and $\bar{z}_2$, and $20 \times 20 \times 1000 \times 7 \times 7 \times 7$ electrons in $\bar{x}, \bar{y}, \bar{z}_2, \bar{p}_x, \bar{p}_y$ and p_{z2}, respectively, giving around 10^{15} electron-field interactions,

each of which involves multiple calculations. The large number of calculations prohibits the practical use of this method, even with a well parallelized code using a large number of processors.

Instead, a solution using the Finite Element Method (FEM) developed in [41] is used, while retaining the beneficial parallel distribution of the Fourier method of [46] and appendix A. The Finite Element solution was revisited as in it each electron only interacts with the 8 field nodes which surround it in 3D space. The number of interactions is then greatly reduced to the number of macro-electrons $N_m \times 8$.

The FEM is implemented in the field source term by replacing the field $A_\perp$ with a sum over elements

$$A_\perp(\bar{x}, \bar{y}, \bar{z}, \bar{z}_2) = \sum_m a_m(\bar{z}) \Lambda_m(\bar{x}, \bar{y}, \bar{z}_2) \tag{4.21}$$

where a_m is a new unknown at each node and Λ is a series of interpolation functions L_i,

$$\Lambda_m = \left(\sum_{n=1}^{8} L_i \right)_m , \tag{4.22}$$

and L_i are linear interpolants given in the table in figure 4.2. These could also be replaced by higher order interpolation functions. Equation (4.21) separates the $\bar{z}$ and $\bar{x}, \bar{y}, \bar{z}_2$ dependancies in the field into two functions. By multiplying the interpolation functions into both sides of eqn (4.20) and integrating over $\bar{x}, \bar{y}$ and $\bar{z}_2$ conveniently removes the delta function, as $\int f(x)\delta(x - x_j)dx = f(x_j)$, so that

$$\int \{\Lambda_m\} \lfloor \Lambda_m \rfloor \frac{\partial a_m}{\partial \bar{z}} dV = \int \frac{\gamma_r}{a_w} \sum_{k=1}^{N_m} \bar{\chi}_k \frac{\bar{p}_{\perp j}(\eta p_{2k}(\eta p_{2k} + 2))^{1/2}}{(1 + |\bar{p}_{\perp k}|^2)^{1/2}} \times \delta^3(\bar{x}_j, \bar{y}_j, \bar{z}_{2j}) \{\Lambda_m\} \, dV \tag{4.23}$$

$$\Rightarrow [K] \frac{\partial a_m}{\partial \bar{z}} = \frac{\gamma_r}{a_w} \sum_{k=1}^{N_m} \bar{\chi}_k \frac{\bar{p}_{\perp j}(\eta p_{2j}(\eta p_{2j} + 2))^{1/2}}{(1 + |\bar{p}_{\perp j}|^2)^{1/2}} (\Lambda_m)_k \tag{4.24}$$

L_n	Definition
L_1	$\left(1-\frac{\bar{x}}{\Delta\bar{x}}\right)\left(1-\frac{\bar{y}}{\Delta\bar{y}}\right)\left(1-\frac{\bar{z}_2}{\Delta\bar{z}_2}\right)$
L_2	$\left(\frac{\bar{x}}{\Delta\bar{x}}\right)\left(1-\frac{\bar{y}}{\Delta\bar{y}}\right)\left(1-\frac{\bar{z}_2}{\Delta\bar{z}_2}\right)$
L_3	$\left(1-\frac{\bar{x}}{\Delta\bar{x}}\right)\left(\frac{\bar{y}}{\Delta\bar{y}}\right)\left(1-\frac{\bar{z}_2}{\Delta\bar{z}_2}\right)$
L_4	$\left(\frac{\bar{x}}{\Delta\bar{x}}\right)\left(\frac{\bar{y}}{\Delta\bar{y}}\right)\left(1-\frac{\bar{z}_2}{\Delta\bar{z}_2}\right)$
L_5	$\left(1-\frac{\bar{x}}{\Delta\bar{x}}\right)\left(1-\frac{\bar{y}}{\Delta\bar{y}}\right)\left(\frac{\bar{z}_2}{\Delta\bar{z}_2}\right)$
L_6	$\left(\frac{\bar{x}}{\Delta\bar{x}}\right)\left(1-\frac{\bar{y}}{\Delta\bar{y}}\right)\left(\frac{\bar{z}_2}{\Delta\bar{z}_2}\right)$
L_7	$\left(1-\frac{\bar{x}}{\Delta\bar{x}}\right)\left(\frac{\bar{y}}{\Delta\bar{y}}\right)\left(\frac{\bar{z}_2}{\Delta\bar{z}_2}\right)$
L_8	$\left(\frac{\bar{x}}{\Delta\bar{x}}\right)\left(\frac{\bar{y}}{\Delta\bar{y}}\right)\left(\frac{\bar{z}_2}{\Delta\bar{z}_2}\right)$

Figure 4.2: Table of linear interpolants for the 3D field elements.

where K is known as the stiffness matrix, given by

$$[K] = \int \{\Lambda_m\} \lfloor \Lambda_m \rfloor \, d\bar{x} d\bar{y} d\bar{z}_2. \tag{4.25}$$

This equation can now be solved with the use of a standard linear solver. K is a large, sparse matrix, so one can take advantage of sparse solvers. K is also a singular matrix, and so boundary conditions must be applied to make the solution valid. The boundary condition applied here is that the matrix values corresponding to the nodes at $\bar{z}_2 = 0$ must $= 0$, as the electrons cannot propagate there: they cannot travel faster than the speed of light c, so in the $\bar{z}_2$ coordinate system, which is the radiation frame, they must always propagate in the negative $\bar{z}_2$ direction.

The linear interpolants are also used to sample the field experienced by each electron in the electron equations.

4.3 Transverse Electron Beam Distribution

The electron distribution in $\bar{x}$ and $\bar{y}$ is assumed to be Gaussian. However, the method of matching the beam in [33] upon which the method in section 3.2.1 was expanded uses a "hard-edged" emittance. Figure 4.3 illustrates the problem in the transverse electron phase space $\bar{x}$ vs $\bar{p}_x$. The red ellipse is the hard-edged emittance, with major and minor axes $2r_{\bar{x}}, 2r_{\bar{p}x}$, and will be the path taken by the outermost electron(s) in a matched beam. The electrons are to be initialized on a rectangular grid, shown in blue, so that the outermost electrons on the corners then follow the path outlined by the hard-edged emittance. Since it is assumed to be Gaussian, the rectangular beam area is of length $6\sigma_{\bar{x}}, 6\sigma_{\bar{p}x}$, where $\sigma_{\bar{x}}$ and $\sigma_{\bar{p}x}$ are the standard deviations of the Gaussian in $\bar{x}$ and $\bar{p}_x$ respectively. This greatly reduces the emittance - which for a Gaussian is $\propto \sigma_x \sigma_{px}$ - from the hard-edged emittance.

To solve this, the hard-edged emittance $\bar{\epsilon}_h$ and the maximum radii $r_{\bar{x}m}$ and $r_{\bar{p}xm}$ are introduced. The rectangular area in the ellipse which covers the largest area has length $r_{\bar{x}m}/\sqrt{2}, r_{\bar{p}xm}/\sqrt{2}$. It can then be inferred that

$$\sigma_{\bar{x}} = \frac{r_{\bar{x}}}{3\sqrt{2}}, \sigma_{\bar{p}x} = \frac{r_{\bar{p}x}}{3\sqrt{2}} \tag{4.26}$$

Therefore the hard-edged emittance is $\bar{\epsilon}_h = 18\bar{\epsilon}$, and the maximum radii, from equations (3.85) and (3.93),

$$r_{\bar{x}m} = \sqrt{\frac{\bar{\epsilon}_h}{\bar{k}_w \bar{k}_\beta}} \tag{4.27}$$

$$r_{\bar{p}xm} = \frac{\bar{a}_w \sqrt{\eta} \bar{\epsilon}_h}{f \bar{k}_\beta r_{\bar{x}}} \tag{4.28}$$

From this a matched beam is initialized with a Gaussian charge distribution in the transverse plane and a corresponding scaled emittance $\bar{\epsilon}$.

4.4 Parallelization

Since the system of equations is not averaged over a radiation wavelength, as with other codes, the sampling period must be sufficiently small to resolve the

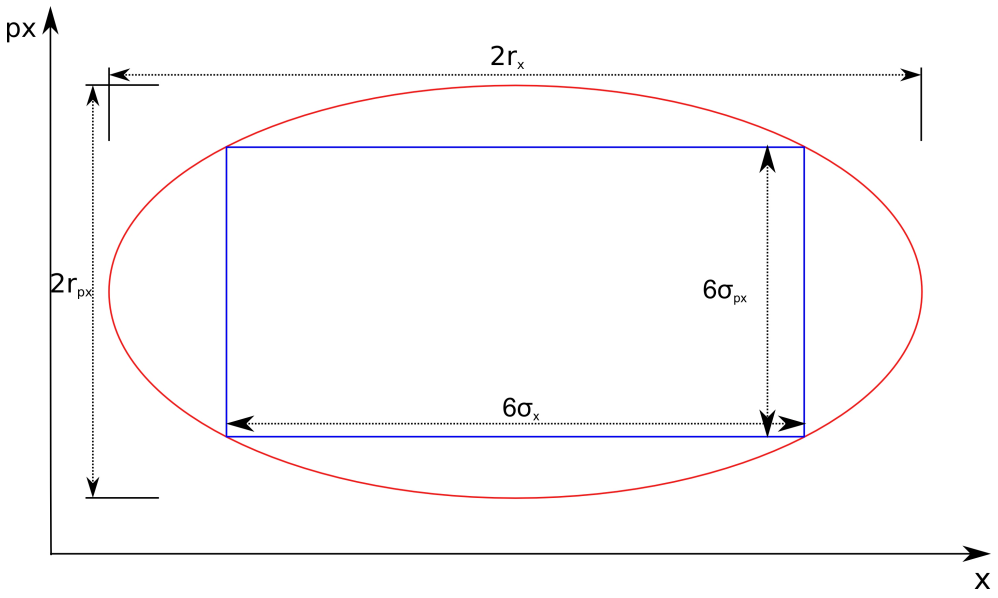

Figure 4.3: Plot of the emittance, $\bar{x}$ vs $\bar{p}_x$. The red line represents a "hard-edged" emittance which is used for beam matching. The red ellipse is therefore the maximum radius of the electrons in the phase space. The blue rectangle indicates the area the macroelectrons are initialized onto, so the outermost electrons at the corners rotate around the ellipse. Imposing a Gaussian of width 6σ onto this square distribution, however, will result in a smaller real emittance, which $= \bar{\sigma}_x \bar{\sigma}_{px}$, than the hard edged emittance shown in red given by the maximum radii.

resonant wavelength of the FEL and any shorter wavelengths such as higher harmonics which are required to be modelled. Furthermore, the electron beam is fully longitudinal and the electrons are not confined to any cyclic phase space. Because of this, the memory and computation requirements are considerable, and the simulations must be run on a parallel machine to distribute the memory.

It is known [47] that the communication of data between processors reduces the performance enhancement from using more processors. Designing a distributed memory code which solves this 4 dimensional FEL system and scales well with the processor number poses an interesting problem in that there are two systems (radiation + electrons) which are constantly shifting in time with respect to one another due to the slippage of the field over the electrons.

An electron must interact with the local field nodes surrounding it, and the field nodes must be driven by any electrons immediately nearby. However, the electrons slip behind the radiation field with each step. If both systems are evenly distributed across processors, this will require a huge amount of inter-process communication, which will hamper the perfomance of the code for large processor numbers. Furthermore, the rate at which the field slips ahead of the electrons is not a constant in an unaveraged system - the equations allow the electron to have a rapid change in energy within one radiation period e.g. for very high radiation fields. So in general it is not possible to predict the relative positions of electrons in advance.

One approach is to pick one of the systems, either the field or electrons, distribute it evenly across processors and fix this distribution. The data distribution for the other system must be calculated at each step and will be shifted around the processors as required. If the field is chosen as the fixed distribution, the electron variables will be shifted between processors. However, this leads to a poor spread of the computational load, as the electrons can only generate, amplify, and interact with the field finite elements which immediately surrounds them. This is especially true for short electron bunches, which is one of the areas an unaveraged code is particularly useful - the electrons in the bunch will only be distributed over a small percentage of the processors available at any one time.

Those processors will be doing all the work to drive the field.

Taking the opposite approach, by distributing the electron data uniformly across the processors, the computational load is well spread in the source step. However, it is desirable to uniformly distribute the field nodes across processors for the diffractive half-step. The two approaches are illustrated in figure 4.4.

In the compromise algorithm presented here, the electrons are distributed uniformly across $\bar{z}_2$ in memory, and a full copy of the field is kept on each processor. This is justified by considering the relative memory sizes for a typical FEL system: each electron has 6 dimensions and the number of electrons can potentially be a few orders of magnitude larger than the number of field nodes; the field has only 3 dimensions. Clearly, the priority is to distribute the electrons in memory. In addition, there is a large sparse stiffness matrix to store in memory, typically ≈ 27 times the size of the field. This is generated and stored in a uniform processor distribution. In this method, the source term is solved in parallel, and a processor does not have to calculate which nodes it needs for the electrons it possesses and obtain them from the relevant processor. This is because the processor already has all the field information stored locally. The diffraction step is easily solved in parallel, as each processor selects a segment of the field to solve from the locally available field array. Likewise for the stiffness matrix calculation. However when calculating the RHS of the source term, in equation (4.24), this cannot be solved without communication between processors. Each processor calulates its own values for the driving term on the RHS from the electrons it possesses, and these values must be added to corresponding values of the RHS from all other processors.

The linear solver used to solve the field source term stiffness matrix equation (4.24) is SuperLU_DIST [48, 49] and the Fourier transforms needed for the field diffraction solution are performed by FFTW 2.1.5 [50]. This is an earlier version of FFTW and is used as it supports MPI routines.

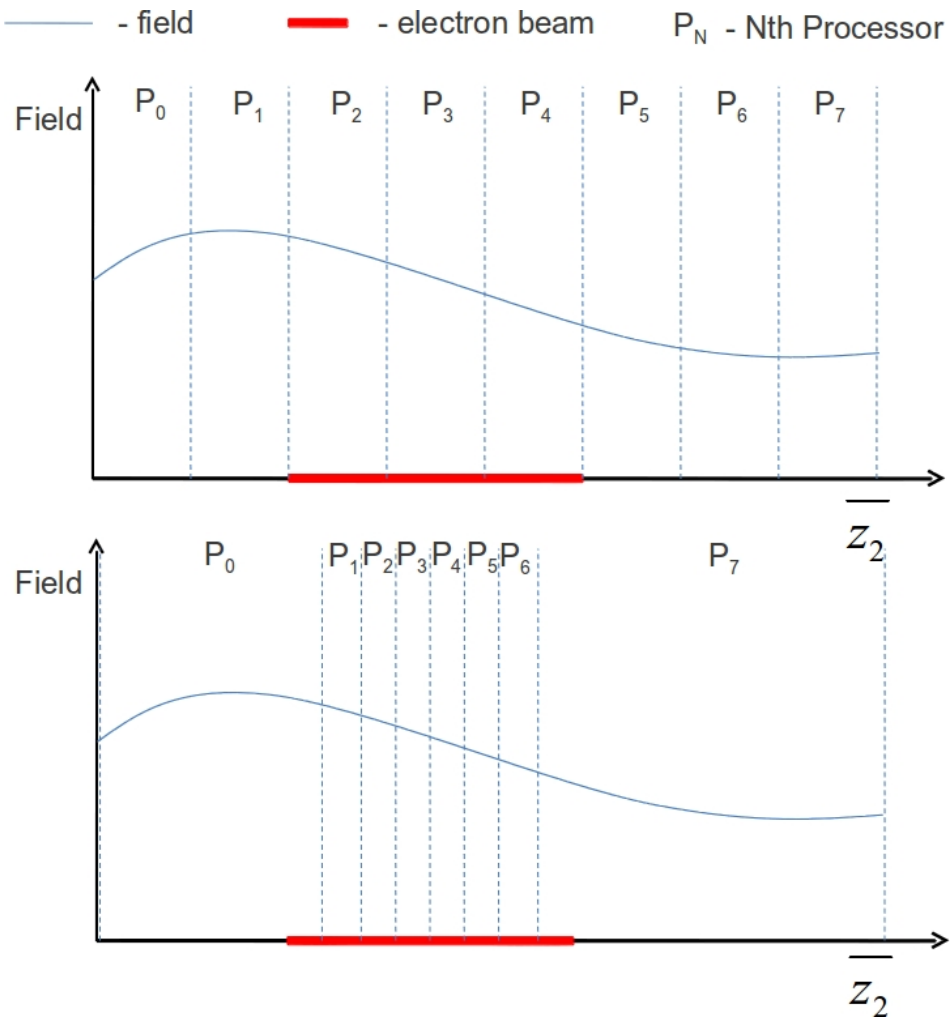

Figure 4.4: Methods of parallelizing the FEL system. Electrons are shown in red, and field indicated in blue. The data must be divided amongst 8 processors, labelled P_0-P_7. The first diagram on top shows the field distributed evenly over the processors, in which case most of the processing is being performed by processors P_2 and P_3, as the field nodes are only driven by the electrons which are close to them. The second shows the electrons distributed evenly, in which case the processing effort seems to be better balanced. Howerever, the diffraction step, which occurs for all field nodes, would then require a redistribution of the field data to make that step have an even computational balance amongst processors.

4.5 Linear Solver Limitations

The memory requirements of the algorithm pose some problems even when parallelizing, and some situations may not be modelled due to memory constraints. These occur when using a long undulator or electron beam.

It is found that the most memory and processor intensive section of the algorithm is solving the linear system of equation (4.24) to obtain $\frac{\partial A_\perp}{\partial \bar{z}}$ for the field equation. The SuperLU_DIST manual [51] explains there is a sequential bottleneck during the initial stages of the solution. In contrast, the Fourier method (in Appendix A) has a sigificantly lower memory requirement - the Fourier method of solving the source term was abandoned only due to slow performance caused by the prohibitive number of calculations required.

In an attempt to reduce the memory demand for the linear solver, an "active" section of the field is chosen in the transverse plane, which includes only those nodes required for the field generation throughout propagation in the entire undulator. It is assumed the electron beam will be confined to this transverse area with the necessary beam focusing. The nodes outside this region are only required for diffraction.

It is worth considering that the total transverse area of the field must be significantly larger than the electron beam, to allow for diffraction. Typically, for 64×64 nodes in $\bar{x}$ and $\bar{y}$, only the inner 20 nodes will be interacting with the electron beam if it is matched to the focusing chanel, as the beam's radius will remain constant. This is shown in figure 4.5. The electron beam will be confined to the area indicated by the green ellipse. The "active" nodes, indicated in red, are the only nodes needed in the linear solver. The outer, blue, nodes are redundant during the solution of the source term. Solving only these inner nodes during the linear solver step dramatically reduces the computation time and memory constraint on the code at run-time.

It may be that SuperLU_DIST is not a suitable choice of linear solver for this problem. It seems to be better suited to non-symmetric systems. A solver optimized for solving systems with symmetric matrices should prove a better

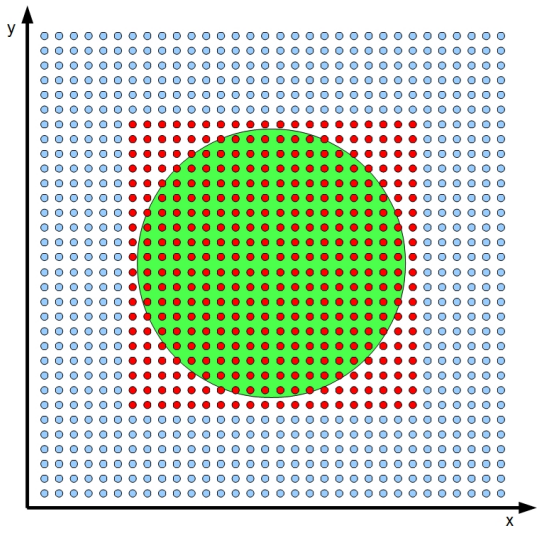

Figure 4.5: Diagram showing the transverse plane of the system, and why only the center nodes are needed to solve the source term. The green ellipse is the transverse electron beam profile, with the transverse field nodes overlayed. The red nodes are the so-called "active" set, which will be solved for in the source term. The blue nodes are only required for the field diffraction.

option and increase performance. It should be relatively simple to change the solver in the code, as all routines pertaining to the linear solver are contained in a single module. Alternative linear solvers which may be considered include PSPASES [52] , MUMPS [53] and DSCPACK [54].

4.6 Diffraction Requirements

Modelling the radiation field on a grid of finite extent has consequences for the diffraction. Since the code models the full radiation spectrum (up to the Nyquist frequency), the code exhibits a frequency dependant diffraction length. For lower, sub-resonant frequencies this can become a problem, especially at very low frequencies which diffract more quickly. As the code must model the field within a finite length in the transverse directions, whilst still preserving an adequate sampling rate in $\bar{x}$ and $\bar{y}$ to model the transverse behaviour of the FEL, it poses a problem when the field diffracts past the transverse boundaries of the system. The diffraction algorithm is performed in transverse Fourier space, which has periodic boundary conditions, and in real space the phenomenon emerges as build-up of a low frequency background field which can become large. This is a problem, in particular, for the Coherent Spontaneous Emission (CSE) from the electron pulse, which arises from the Fourier components of the shape of the electron pulse, and so typically has significant low frequency content. This type of emission cannot be modelled in an averaged code, and may be a significant source of start-up from FEL's using short electron pulses. The diffraction characteristics and the implications for the code are now described.

The Rayleigh range is a measure of the diffraction in the system. After one Rayleigh range in z the waist of the intensity will increase by $\sqrt{2}$. The Rayleigh range may be written as [23]

$$z_R = \frac{\pi w_{x0}^2}{\lambda} \tag{4.29}$$

where w_{x0} is the initial waist of the intensity in x (or y), and λ is the radiation wavelength. This is obtained assuming the following form for the intensity

distribution I in x and y:

$$I = I_0 \exp\left[\frac{-2x^2}{w_{x0}^2}\right] \tag{4.30}$$

where I_0 is the peak intensity.

The input parameters given in the code are the standard deviation $\sigma_{\bar{x},\bar{y}}$ of the electron beam and $\sigma_{f\bar{x},\bar{y}}$ of the seed field in the transverse directions. So it is desirable to change to these variables.

The field envelope is defined from the standard deviation σ_{fx} by the standard form of the Gaussian distribution,

$$\xi_0 = \xi_{0pk} \exp\left[\frac{-x^2}{2\sigma_{x0}^2}\right] \tag{4.31}$$

and the intensity is simply the magnitude of the envelope squared

$$I = |\xi_0|^2 = \xi_{0pk}^2 \exp\left[\frac{-x^2}{\sigma_{x0}^2}\right] \tag{4.32}$$

and so it is found that

$$w_0 = \sqrt{2}\sigma_{fx0} \tag{4.33}$$

So changing the Rayleigh length (4.29) to the scaled notation, recalling that $\bar{z} = z/l_g$, $\bar{z}_2 = ct/l_c$,$\bar{x}, \bar{y} = x, y/\sqrt{l_c l_g}$, and changing to the standard deviation of the field gives

$$\bar{z}_R = k_{z2}\sigma_{f\bar{x}0}^2 \tag{4.34}$$

where $k_{z2} = 2\pi/\lambda_{z2}$ is the wavenumber in $\bar{z}_2$.

The general expression describing the characteristic σ_{fx} of a Gaussian field after a propagation distance z is

$$\sigma_{fx} = \sigma_{fx0}\sqrt{1 + \frac{z^2}{z_R^2}} \tag{4.35}$$

This places restrictions on which frequencies can be modelled with a transverse plane of finite extent without excessive build-up of low frequency due to

periodic boundary conditions. The length of the sampled field in the transverse axes must be long enough to accomodate the full length of the radiation being modelled. If the field diffracts to an area beyond the extent of the model then the numerical solution becomes invalid, resulting in a significant non-zero background field arising. To avoid this, the length of the sampled field in x and y, $l_{wx,y}$ must be larger than the total length of the intensity distribution of the field in those directions.

In the code a Gaussian distribution is generally assumed to be adequately described by a total length of $6\sigma_{fx}$, for example when initializing the electron distributions or initializing a seed field. Here, however, the Gaussian is assumed to have **significant** values at the edges of the sampled field in the transverse plane when $l_{wx} = 4\sigma_{fx}$. Then the length of the sampled field in the transverse plane l_{wx} is able to model a frequency component with transverse size $4\sigma_{fx}$ when

$$l_{wx} > 4\sigma_{fx} \tag{4.36}$$

and converting to scaled notation and substituting in expression (4.35) to obtain the condition of the length of the sampled field in $\bar{x}$, $l_{w\bar{x}}$ after propagation distance $\bar{z}$ and initial transverse fied size $\sigma_{f\bar{x}0}$ gives

$$l_{w\bar{x}} > 4\sigma_{f\bar{x}0}\sqrt{1 + \frac{\bar{z}^2}{\bar{z_R}^2}} \tag{4.37}$$

and using (4.34) and rearranging gives the allowed frequencies in $\bar{z_2}$:

$$k_{z2} > \frac{\bar{z}}{\sigma_{\bar{x}0}^2}\left(\frac{l_{w\bar{x}}^2}{16\sigma_{f\bar{x}0}^2} - 1\right)^{-1/2} \tag{4.38}$$

This shows that for the full 3D model there is a low frequency cut-off below which the field cannot model correctly. The best solution is to employ absorbing or transparent boundary conditions [55]. This is a non-trivial solution. Two other simpler methods are considered.

The first is to simply not allow the lower frequencies to diffract. This is easy to do as the diffraction solution (equation (4.13)) is in Fourier space with an explicit

frequency dependence. It will, however, lead to an unphysical field intensity at these frequencies. However, if these frequencies are far below the resonant frequency they should not have any significant effect on the collective electron beam-radiation interaction, and can be safely filtered out in post processing.

The other option is to filter the lower frequencies during the simulation. It could be argued that this is closer to what would actually happen in the undulator since these frequencies will diffract away very quickly.

It must be noted that either solution means that the low frequencies below the cut-off are not being modelled correctly. The validity of this is entirely dependant upon the parameters being modelled. For instance, in [56], which describes a 1D helical FEL model similar to the 3D version presented here, the electrons are decelerated in small bursts over a period smaller than a resonant wavelength by a narrow, intense radiation pulse. If the energy exchanges happen on this small a scale then high power low frequency components could become important. On the other hand, for a more conventional system, where the exchange is only significant over many undulator periods, it is safe to assume that radiation far from resonance can be ignored.

One criticism is, of course, that the code here is designed specifically to model frequencies away from resonance. For now it is noted that only very low frequencies will be ignored, which still enables a wider frequency model than that using the SVEA, and that ALL frequencies above the cut-off, including higher harmonics are still modelled self-consistently.

The cutoff will fall close to the resonant frequency ω_r for smaller values of the electron beam transverse dimension $\sigma_{x,y}$, because a smaller initial transverse radius will result in a shorter gain length, from equation (4.34). In the 3D simulations presented in section 5.4.2, the highest frequency cutoff is at $\approx \frac{\omega_r}{3}$, that is, one-third of the resonant frequency.

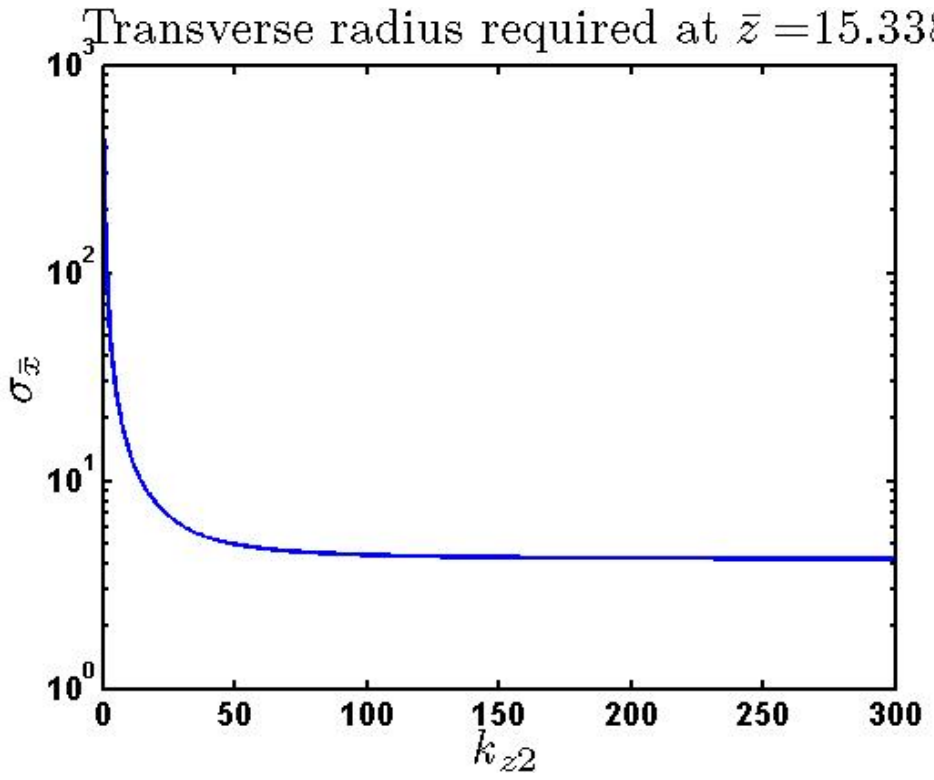

Figure 4.6: Plot of the how the frequency cutoff, defined by equation (4.38), varies with the initial radius $\sigma_{\bar{x}}$, for a fixed $\bar{z}$. The larger the initial radius, the smaller the cutoff.

4.7 Code Overview

A diagram of the parallel code algorithm is shown in figure 4.7. The yellow boxes correspond to non-parallel operations, which each processor performs on its own in full. For example, the full global field array is kept on each processor, so it is generated, in full, by each processor individually.

The code is written in FORTRAN 90/95, and has been written using open-source packages, to enable maximum portability. The data is output in SDDS format [57]. There is no parallel support for SDDS, so the processors take turns at opening the data file(s) and writing their own local data to them.

At the moment, the post-processing of the data files is performed using a number of routines written in MATLAB, which is proprietary software. However, it should not be difficult to change this to its FOSS (free and open source software) alternative, Octave. Or it may be wiser to use analysis packages on the servers the code is run on. Given that the data files are potentially very large, so that analysing the data on a standard desktop machine will not be possible for large runs, and transporting the data between machines is a troublesome issue, as is the storage of the data, if it is to be stored permanently, it may be more efficient to analyse the data on the servers on which the code is run.

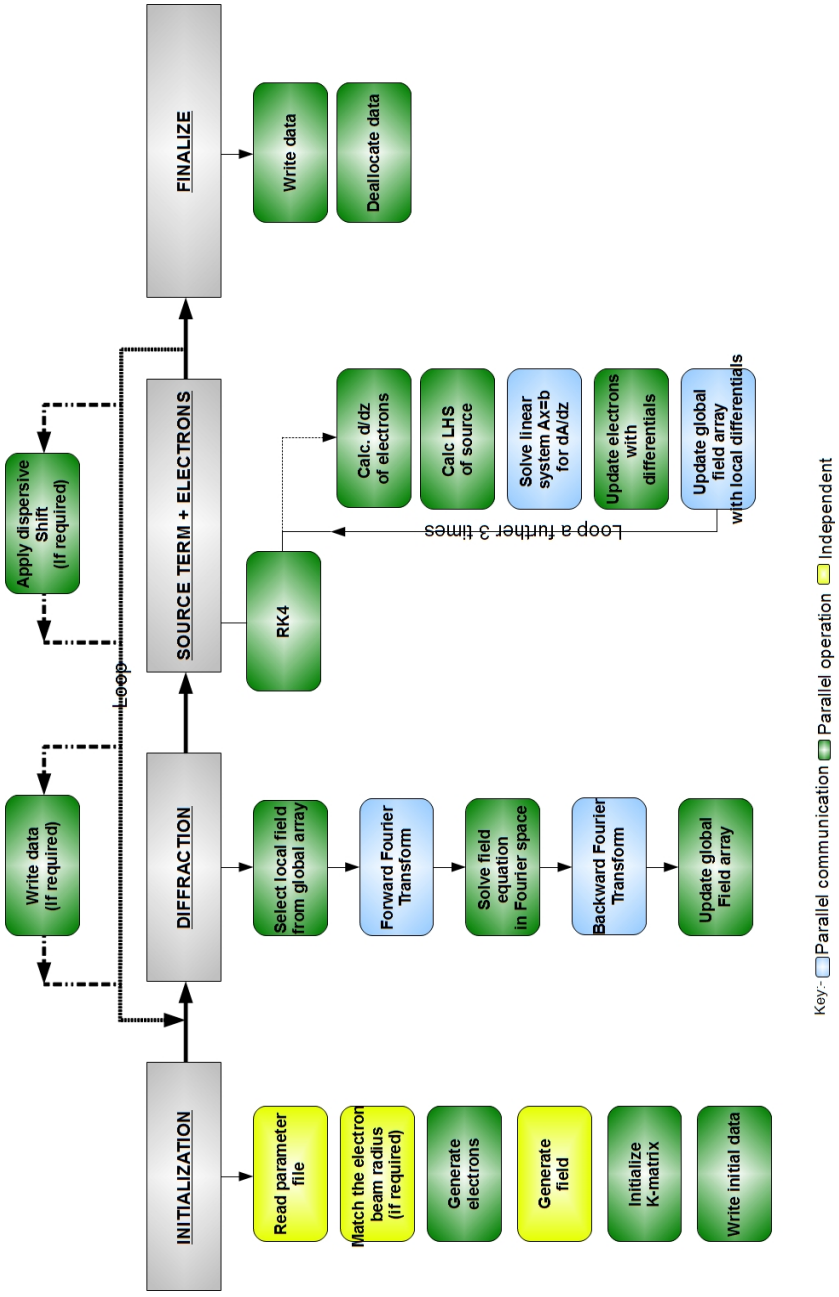

Figure 4.7: Diagram of full algorithm.

Chapter 5

Results

Several FEL systems are now modelled using the simulation code. The initial results are to test the code against previous 1D unaveraged FEL results in [58], [40] and [45], which test the 1D limit and demonstrate that the field and electron bunching are being described correctly. The subsequent results show the effects of the undulator polarization, undulator chicane sections, 3D electron beam focusing and field diffraction. The final examples demonstrate new, potentially exciting, effects that the code may be used to investigate.

5.1 1D Approximation

Initially, the code is run in the 1D limit, using parameters from [58], [40] and [45]. The results are shown in the following subsections and give excellent agreement with the referenced works.

In the 1D limit, the source equation 4.16 is integrated over $\bar{x}$ and $\bar{y}$, so that

$$\frac{\partial A_\perp}{\partial \bar{z}} = \frac{\gamma_r}{a_w \bar{n}_p T} \sum_{j=1}^{N} \frac{\bar{p}_{\perp j}(\eta p_{2j}(\eta p_{2j}+2))^{1/2}}{(1+|\bar{p}_{\perp j}|^2)^{1/2}} \delta(\bar{z}_2 - \bar{z}_{2j}), \tag{5.1}$$

where T is the transverse area of the radiation field. Diffraction is not solved, and only one node and one electron in the transverse plane are used.

5.1.1 CSE in a Helical Undulator

The following parameters, taken from [40], are used in this first benchmark. The parameters test if the Coherent Spontaneous Emission (CSE) is being generated correctly. CSE arises from current gradients in the electron pulse. The radiation feedback is switched off to observe only the spontaneous emission from the electron pulse. This is achieved by forcing $A_{\perp j} = 0$ in the electron equations.

The FEL parameter $\rho = 0.01$ and the rms wiggler parameter $\bar{a}_w = 2.0$ were used. The electron pulse is $2l_c$ long, that is, two coherence lengths, corresponding to a length of 2 in the $\bar{z}_2$ frame (as $\bar{z}_2 = (ct - z)/l_c$). The undulator is 1 gain length long, i.e. $\bar{z} = 1$. A resonant wavelength in $\bar{z}_2 = 4\pi\rho$ and an undulator period in $\bar{z} = 4\pi\rho$. So the undulator length ≈ 8 periods long. The electron pulse has a rectangular or "flat-top" current distribution in $\bar{z}_2$, and there is no noise in the cold, resonant distribution, meaning that $p_{2k} = 1$ and the electron weighting factor $\chi_k = 1 \forall k$. As a consequence the current gradient is zero except at the edges of the electron pulse, where there is a discontinuity in the current gradient. The radiation feedback onto the electrons is artificially switched off here, so that only the spontaneous emission from the electron pulse is generated.

As explained in section 2.4, in an averaged model of the FEL, the field is averaged over a length in $\bar{z}_2$ equivalent to at least 1 resonant radiation cycle, and so rapid variations in the source term on the scale of this averaged period are not modelled correctly in such an averaged code. However, without averaging, the discontinuities at the edges of the pulse result in a strong coherent emission necessitating an unaveraged model of the FEL.

The plots in figure 5.1 show the scaled intensity $|A_\perp|^2$ as a function of $\bar{z}_2$ at different positions within the first undulator period. The electron macroparticle positions, shown in red, are intitialized at position $0 \leq \bar{z}_2 \leq 2$ as shown in plot *a*). In the $\bar{z}_2$ frame, the electron pulse tail is to the right, and as the pulse moves from left to right it is slipping back through the stationary radiation frame. In this sense $\bar{z}_2$ is like a scaled time variable. The intensity emitted from the pulse is seen to oscillate within an undulator period, shown in *b*)- *d*). The electron pulse slips back, and the observed interference effect results in the coherent radiation spikes

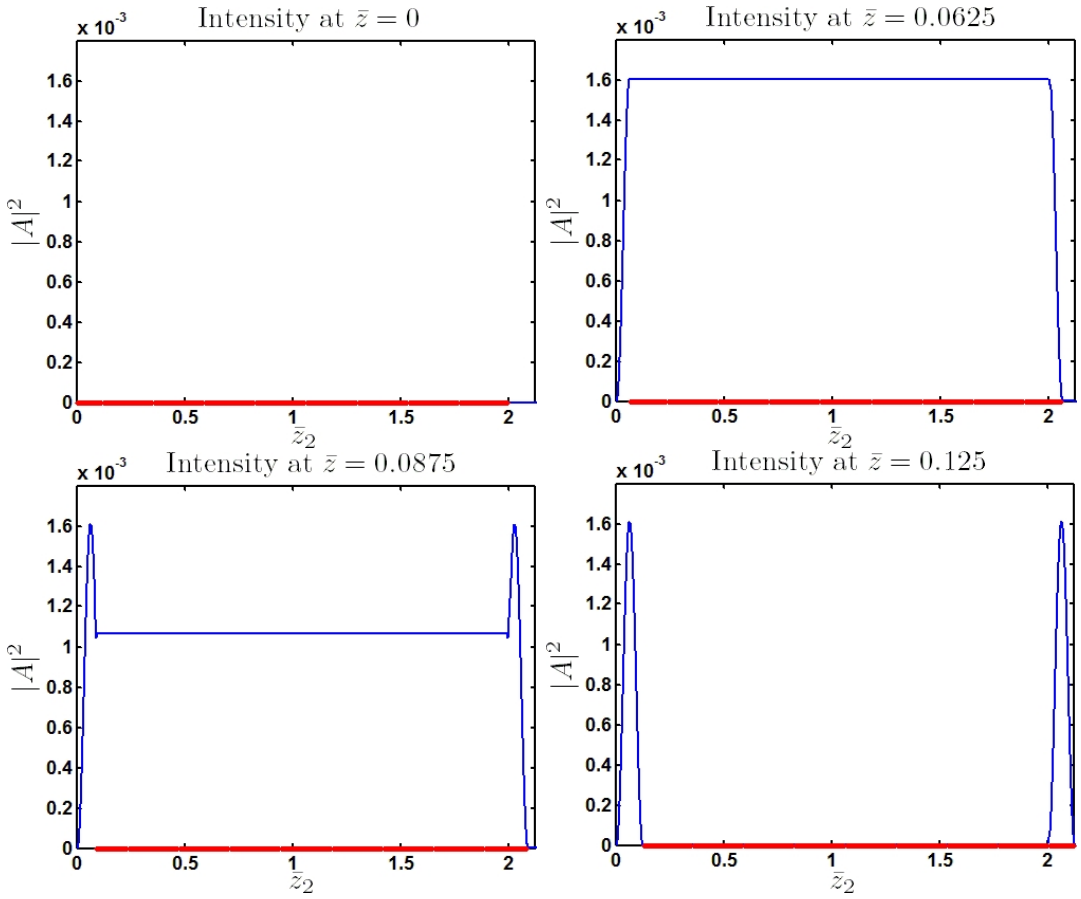

Figure 5.1: Multiple plots of scaled intensity vs $\bar{z}_2$. The code is in the 1D limit, and the plots show the generation of CSE over an undulator period. The electron beam position in $\bar{z}_2$ is in red. The intensity over the electron pulse is seen to oscillate and a process of constructive interference leaves the CSE spikes at the head and tail of the electron pulse.

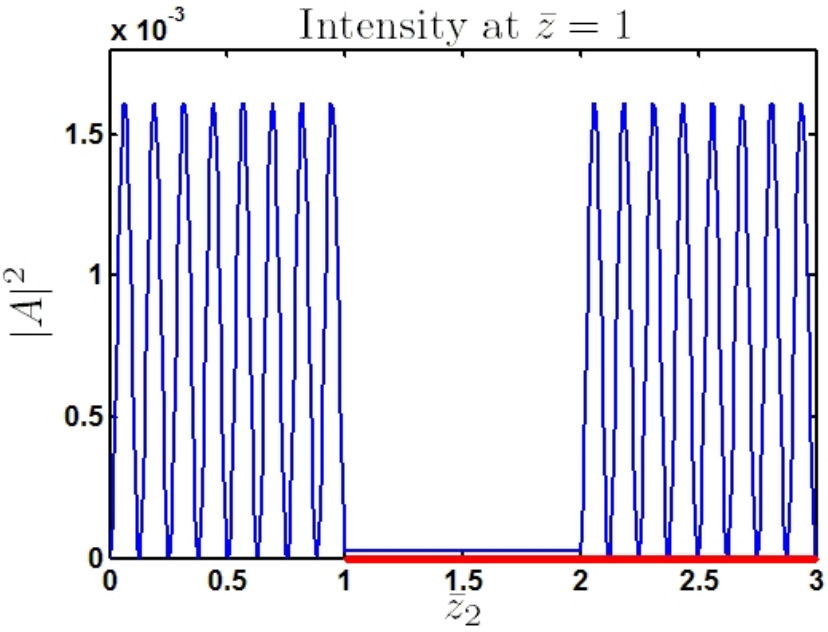

Figure 5.2: The code in the 1D limit, after a further 7 undulator periods from the simulation results in figure 5.1. Therefore 8 CSE spikes in radiation intensity have been generated through the process shown in figure 5.1. The plot gives excellent agreement with [40].

emitted from the edges after one full undulator period, seen in the final plot. The region over the electron pulse $0.125 \leq \bar{z}_2 \leq 2$ in d) has destructively interfered. If the electron macroparticle weights had noise added, this destructive interference cycle would result in a small random noise in the intensity, from which the SASE process begins.

The final result after 1 gain length, or 8 undulator periods, is presented in figure 5.2. It gives excellent agreement with the simulation presented in figure 1 of [40]. The 8 spikes of duration 1 resonant wavelength are the result of the interference effect shown in figure 5.1. According to CSE theory the magnitude of the coherent emission should be $\approx 16\rho^2 = 1.6 \times 10^{-3}$ [40]. The position of the electrons in $\bar{z}_2$ are again shown in red, and the electron beam is seen to have propagated in $\bar{z}_2$ to $1 \leq \bar{z}_2 \leq 3$, with the head of the pulse at $\bar{z}_2 = 1$ and the tail at $\bar{z}_2 = 3$.

5.1.2 SACSE in a Helical Undulator

In the previous section, the radiation feedback onto the electrons was artificially switched off in the code. This interaction is now switched on in the code so that the radiation/electron interaction is self-consistent and one observes the FEL amplifying the initial CSE. This amplification process, with startup from CSE rather than noise, is known as Self Amplified Coherent Spontaneous Emission (SACSE) [40]. The electron pulse in the example presented here is 10 cooperation lengths long, the undulator is 15 gain lengths, and $\rho = 0.005$.

Again, a flat top current distribution is used, so $\chi_k = 1$ for all electrons. As in the previous section, the CSE will be emitted strongly from the edges of the electron pulse. The intensities at two different propagation distances through the undulator are shown in figure 5.3.

In the top plot, the electron pulse $\bar{z}_2$ position is again indicated in red along the axis, and the scaled intensity $|A_\perp|^2$ is shown in blue. The head of the electron pulse is at $\bar{z}_2 = 3.75$. At this stage one can identify three distinct slippage, noise and free-space regions.

The free-space region is that for $0 \leq \bar{z}_2 \leq 3.75$, and here the CSE from the head of the electron pulse has propagated forward into free space, and does not interact with the electron pulse. As in the previous section, the amplitude of the CSE is oscillatory with a period of $4\pi\rho$, but the oscillations cannot be resolved on the scale shown. The slippage region $10 \leq \bar{z}_2 \leq 13.75$ contains the CSE from the tail of the pulse, which has propagated through the electron beam towards the head, and has been amplified. The region $3.75 \leq \bar{z}_2 \leq 10$, is the so-called steady state region. It shall be called the noise region here, since it is the region evolving noise alone, and is outwith any influence of CSE.

The CSE bunches the electrons as it propagates over them from the rear, and this, in turn, amplifies the field more strongly. This self-consistent interaction continues until the radiation is amplified to a superradiant-type spike, shown in the bottom plot of figure 5.3, at $\bar{z}_2 \approx 14$. The electron pulse is shown between $15 \leq \bar{z}_2 \leq 25$, with the front of the electron pulse at $\bar{z}_2 = 15$. There is no longer any noise region as the CSE has propagated throughout the entire electron pulse.

Figure 5.3 is a reproduction of the SACSE plot in [40]. It is important to recall here, that for comparison with [40], the $\bar{z}_2$ coordinate system is inverted with respect to the $\bar{z}_1$ frame of [40]. Both models are in excellent agreement.

Reference [40] also compared the non-averaged results evolving from CSE with those of the averaged model which contains no CSE and evolves from noise alone. These results demonstrate that SACSE generates output of much higher output intensity, and reduces the shot-to-shot fluctuations.

5.1.3 SACSE in a Helical Undulator with Energy Spread

The previous two sections utilized a flat-top current distribution, with no noise or energy spread. Now, the noise and energy spread are added to allow comparison with the two results presented in [45].

[45] describes the method of generating an electron distribution in an un-averaged FEL code based on Poisson statistics. The results of two simulations are shown which describe the effects of energy spread on the generated CSE, and shows whether CSE or noise dominates the generated field, for two different electron beam distributions, a Gaussian and a flat-top.

Both the flat-top and Gaussian cases with noise are run, with $\rho = 7.96 \times 10^{-3}, \bar{a}_w = 2, \gamma_r = 100.0$ and $Q = 1nC$, in line with the examples in the reference. For the flat-top case an electron pulse of duration $6l_c$ is used, and the undulator is $5l_g$ long. In the Gaussian case, the pulse is $18l_c$ long, with standard deviation $\sigma_{z2} = 3$ and the undulator length is $2l_g$. In both cases there is a longitudinal momentum spread of standard deviation $\sigma_{p2} = 0.008$, which corresponds to the momentum spread in the $\bar{z}_1$ frame $\sigma_p = 0.5$ in the reference.

The main features in the flat-top case, shown in the top of figure 5.4, are the same as those modelled in the previous section in the top graph in figure 5.3. The free space region is between $0 \leq \bar{z}_2 \leq 5$, the amplified CSE is present in the region $6 \leq \bar{z}_2 \leq 11$, and the section of the pulse still evolving only from noise is $5 \leq \bar{z}_2 \leq 6$. Note the reduction in the magnitude of the emitted CSE in the free-space region. This is due to the energy spread smearing out the discontinuity in the electron beam current profile at the front of the pulse. Here the oscillations in

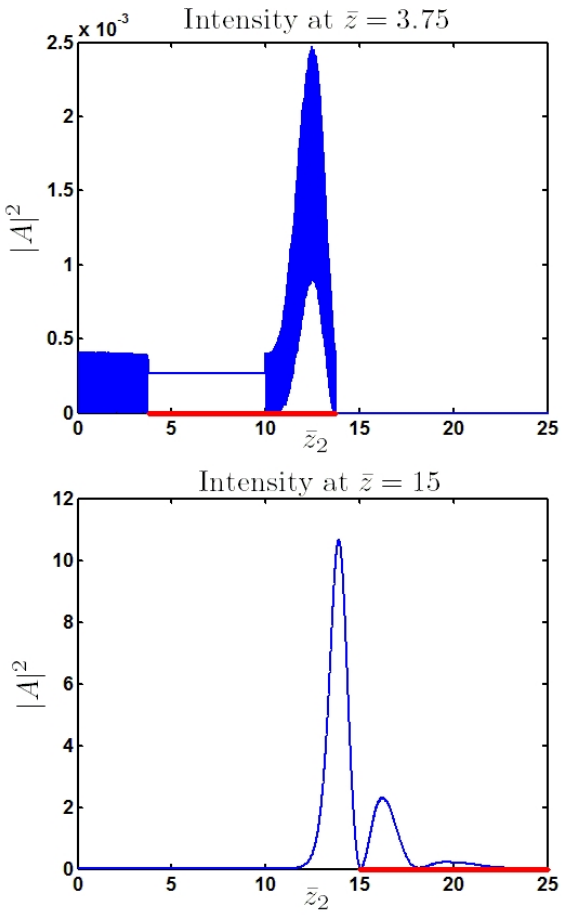

Figure 5.3: Plots of scaled intensity vs the scaled time coordinate $\bar{z}_2$. The code is in the 1D limit, using parameters used to produce figure 2 of [40]. A flat top current distribution has been used. The electron pulse position is in red. The initial CSE can be see in the top plot, emitted from the discontinuities in the electron current at the edges of the electron pulse. The oscillations in amplitude are not able to be resolved at this scale. The CSE from the back of the electron pulse, on the right side of the pulse, has been amplified as it passes over the electron pulse. The bottom plot shows the same process further in the undulator. The amplification of the CSE having propagated over the electron pulse has resulted in a large intensity spike. This is SACSE.

the magnitude of the CSE can be clearly seen to be decreasing as the interaction progresses and the current edge has become less defined.

The bottom graph in figure 5.4 is a filtered version of the top plot. The spectrum is filtered to allow only frequencies above $\approx 0.2\lambda_r$ to be shown. Note that the oscillations in the CSE are no longer present, demonstrating that the oscillations are due to the low frequency emission which is dependant on the shape of the electron pulse. The low frequency content causes the envelope of the higher resonant frequency to modulate. The coherent emission at resonance is still seen to be much larger than the emission from noise.

For a Gaussian current, the top plot of figure 5.5 again exhibits CSE from the current gradients in the pulse. However, as the electron pulse has a Gaussian current distribution, there are two spikes peaking where the gradient is maximum.

Both the regions $0 \leq \bar{z}_2 \leq 2$ and $18 \leq \bar{z}_2 \leq 20$ exhibit CSE from the discontinuities at the head and tail of the electron pulse. This is due to the electron pulse being sampled for a finite length of $6\sigma_{z2}$ in $\bar{z}_2$. Modelling the electron pulse to 9σ will reduce this, although not remove it completely. It is important to note this fact. If one desires to startup the FEL process from only the noise of the electron pulse, then this CSE must be smaller than the noise. This is not the case here, as shown in the second plot of figure 5.5 where a high bandpass filter has been applied. The lower frequencies are eliminated, and only the radiation primarily from the resonant frequency is shown. Other frequencies are present, but the dominant frequency is the resonant frequency. Without filtering there are low frequency components of CSE present from the shape of the electron pulse. It is seen from the noisy structure of the output that the noise dominates the CSE at the resonant frequency. It is also seen from this filtered plot that the CSE from the finite sampling, in the regions $0 \leq \bar{z}_2 \leq 2$ and $18 \leq \bar{z}_2 \leq 20$, is larger in magnitude than the noise. Again, it should be emphasised, this arises from the edges of a Gaussian sampled beam. The plots in both the flat top and Gaussian cases agree with the results of [45].

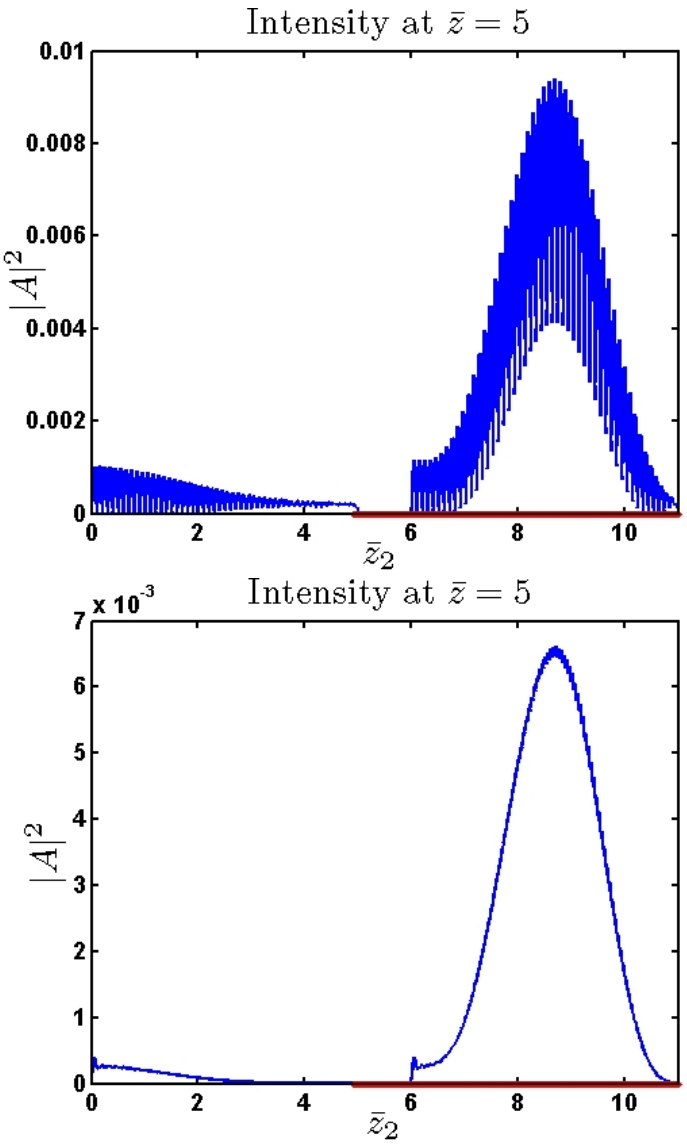

Figure 5.4: Plots of scaled intensity vs the scaled time coordinate $\bar{z}_2$. The code is in the 1D limit, using parameters used to produce figures 4 and 5 in [45]. In the top plot, similar behaviour to the top plot in figure 5.3 is observed. The amplification of CSE from the electron pulse tail can be seen. The bottom plot show the same result, with a high band pass filter applied to the radiation field. Frequencies $\leq 0.2\lambda_r$ are neglected. The oscillations in the CSE intensity have disappeared.

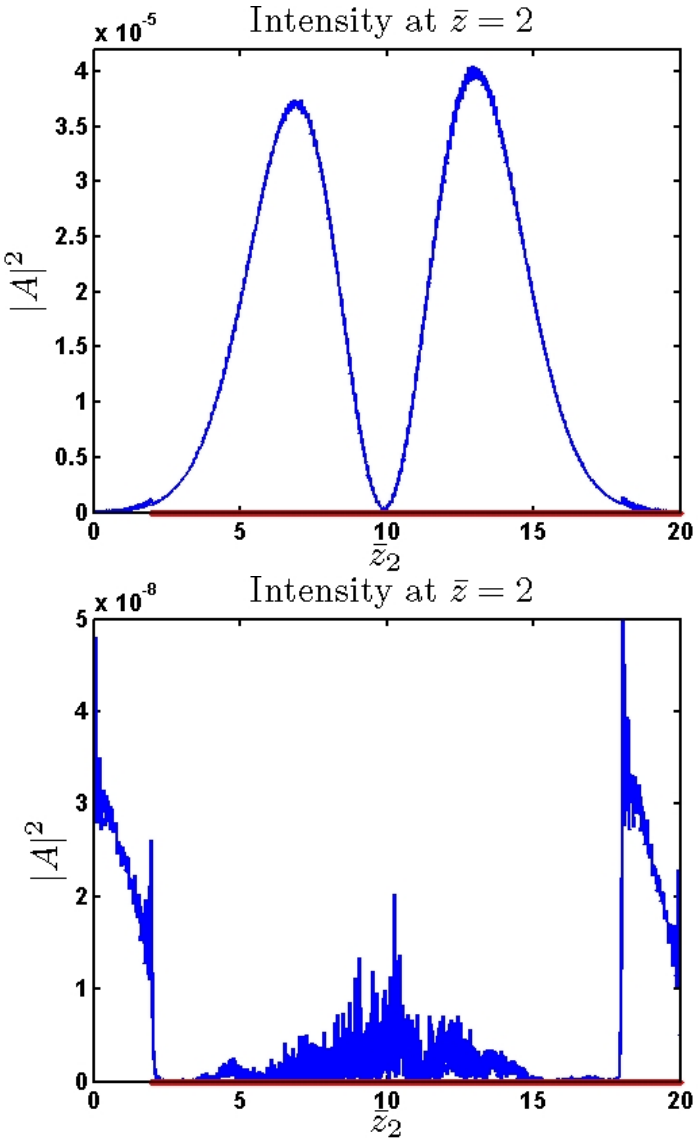

Figure 5.5: Plots of scaled intensity vs the scaled time coordinate $\bar{z}_2$. The code is in the 1D limit, using parameters used to produce figures 7 and 8 in [45], giving excellent agreement. A Gaussian current distribution (with noise) is used with $\sigma_{z2} = 3$. In the top plot, the CSE, arising from current gradients in the electron pulse, peaks twice, where the current gradients are largest. The bottom plot is the filtered intensity. All radiation frequencies $\leq 0.2\lambda_r$ are neglected. As the low wavelengths from the electron pulse shape are now gone, the noise is seen to dominate at the resonant frequency.

5.1.4 SACSE in a Planar Undulator

For the final test in the 1D limit, a comparison with the result presented in [58] is performed, where an unaveraged 1D model of a planar undulator FEL was described. The result is compared to the case of a flat-top current distribution in the reference. There is noise present in this example. The FEL parameter $\rho = 0.01$, $\bar{a}_w = 2$, $\gamma_r = 100$ and the undulator polarization is $f_x = 0, f_y = 1$. Figure 5.6 shows the x radiation fields at distances $\bar{z} = 2$ and $\bar{z} = 25$ into the wiggler. The electron pulse measures $40l_c$ in length. This is a much longer electron pulse and propagation distance than the previous examples. The features of the plots are the same as in the flat top cases of SACSE in the helical undulator, although now, for a direct comparison with [58], the scaled x polarized field is shown rather than the intensity. The top graph shows the initial CSE, with the noise, free-space and slippage regions cearly visible. There is no apparent amplification yet. The bottom graph shows the expected SACSE spike at $\bar{z}_2 \approx 45$, and the noise region over the electron pulse is at $25 \leq \bar{z}_2 \leq 40$, as the SACSE spike has not propagated to this region yet. The noise region in this example has amplified to saturation: this is SASE. The intensity spikes from the SASE appear to have a random structure, and are evolving independently. Given that there is no energy spread, this example is deep into saturation, and the normal expected characteristics of the SASE process (spike separation $\approx 2\pi l_c$ etc) occuring at saturation may not be valid.

5.2 Polarization

The field polarization is driven by the electrons traversing a wiggler of polarization specified by f_x and f_y. Simulations are now presented that demonstrate that the field and its polarization are driven consistently with such a variable transverse current. The simulations in this section are performed in the 1D approximation described in the previous subsection.

Figure 5.7 shows the field generated in 3 separate simulations. In each, an identical, extremely short, electron pulse propagates an undulator with different

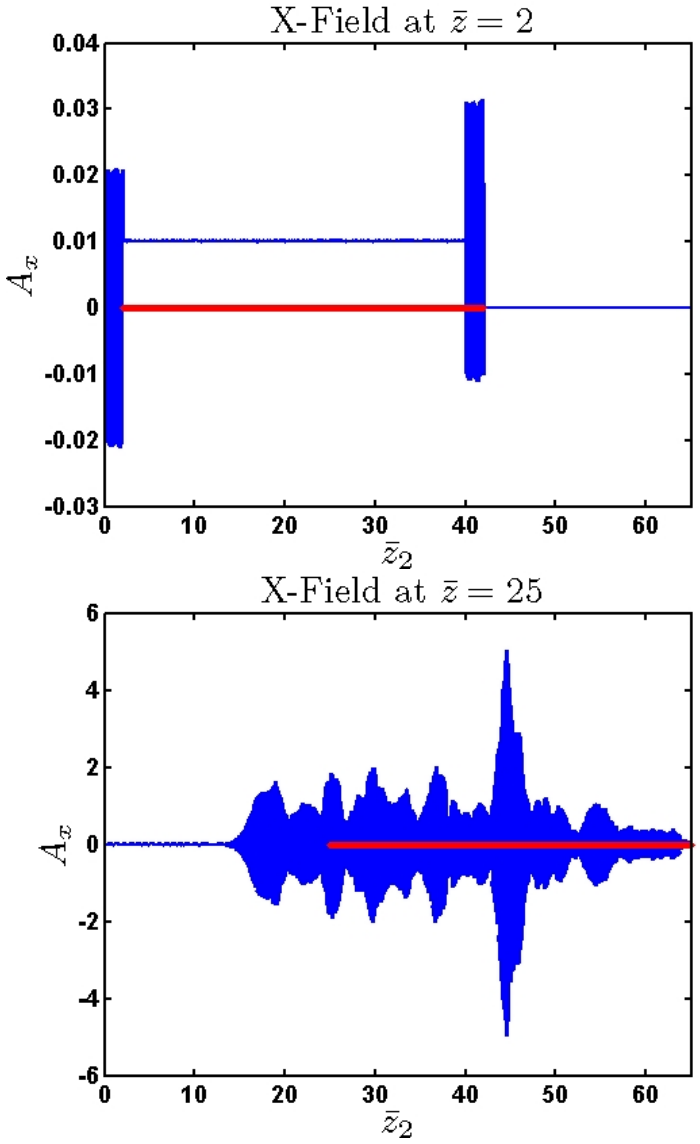

Figure 5.6: Plots of scaled x polarized field vs the scaled time coordinate $\bar{z}_2$. The code is in the 1D limit, using parameters used to produce figure 3 in [45], giving excellent agreement. A flat top current distribution is used, this time in a planar undulator. The features present in the two plots in figure 5.3 are present here, with the initial CSE from the rear of the electron pulse (at $\bar{z}_2 = 42$) in the top plot being amplified as it propagates though the electron pulse in the bottom plot. Note this time the scaled field is plotted rather than the intensity.

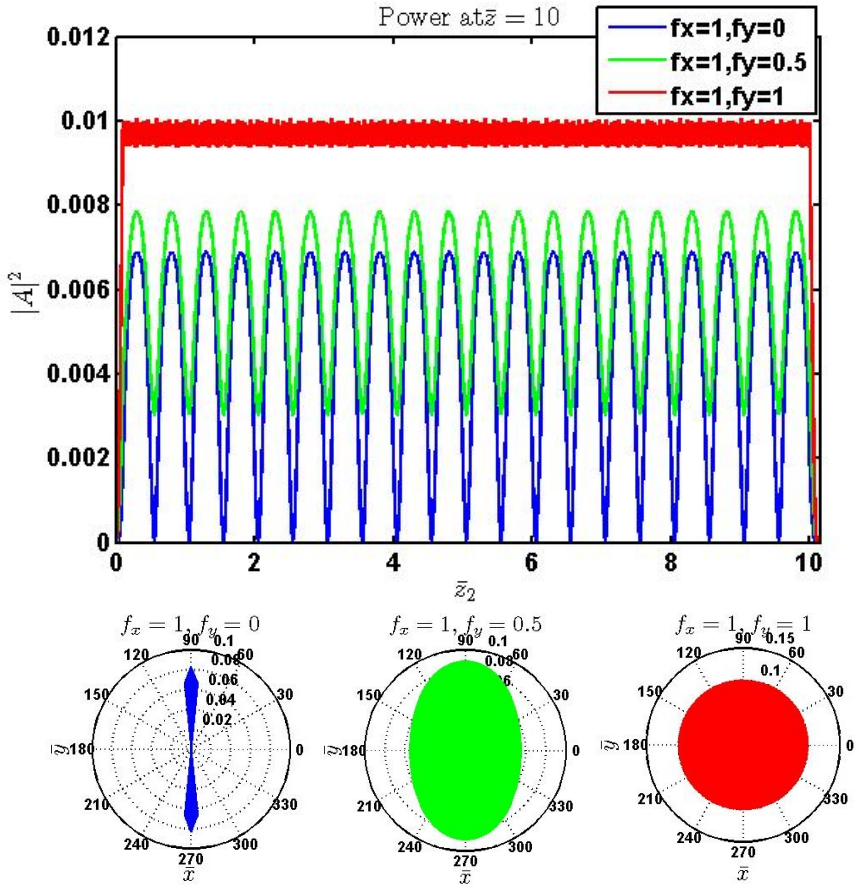

Figure 5.7: Example of different field polarizations as driven by electrons in planar, eliptical and helical wigglers as specified by f_x and f_y. The radiation polarization profiles are shown at the bottom, and the scaled powers on top. The undulator is 20 undulator periods long. The electron pulse length $l_e = 0.1\lambda_r$, so has radiated coherently, generating an output much like a single electron with a large charge.

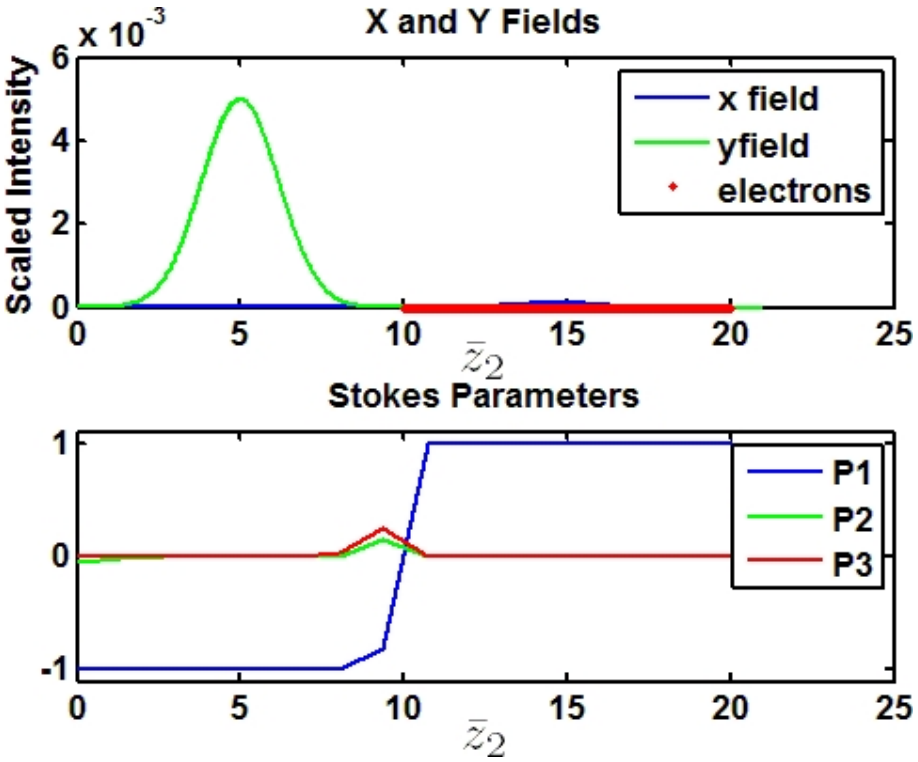

Figure 5.8: The plots show the result of seeding a y polarized undulator (so the electron oscillation is in x) with a y polarized field. The upper plot shows the intensity of the x and y fields, and the position of the electron pulse, which has a Gaussian distribution of 1.667 and a total length of $l_e = 10$ in $\bar{z}_2$. The undulator propagation distance is $\bar{z} = 10$. The original Gaussian seed field is still present between $0 < \bar{z}_2 < 10$, and has been unaffected by the electron beam. The lower plot shows the 3 Stokes parameters, $P1$, which shows the linear polarization rate, $P2$, which shows the skew polarization rate, and $P3$, which shows the circular polarization rate.

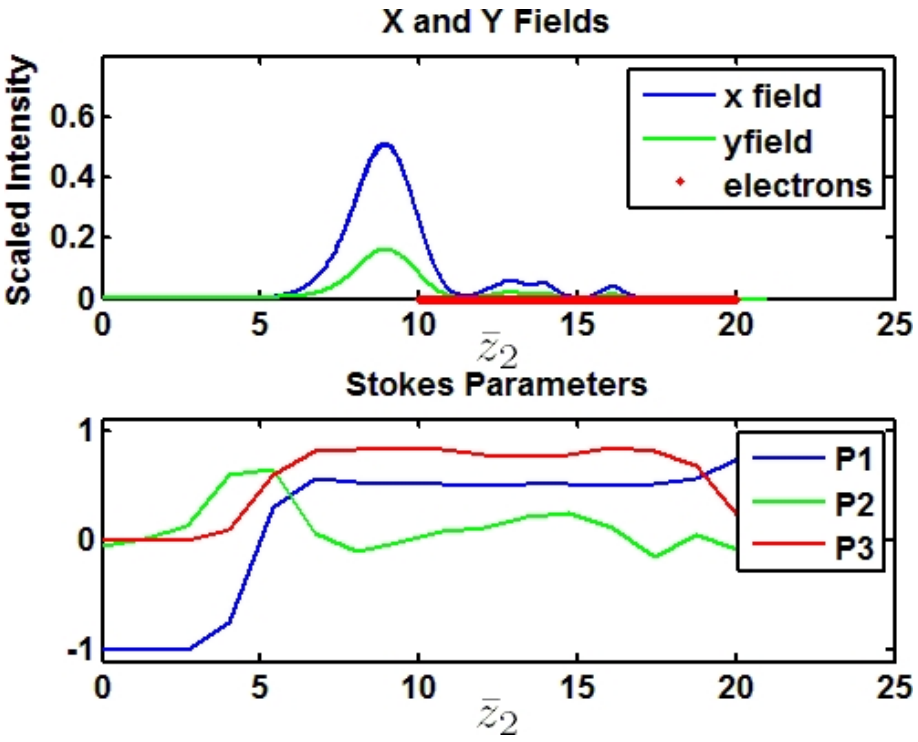

Figure 5.9: The same two plots as in figure 5.8, this time using an undulator of polarization $f_x = 0.5, f_y = 1$. All other parameters are the same.

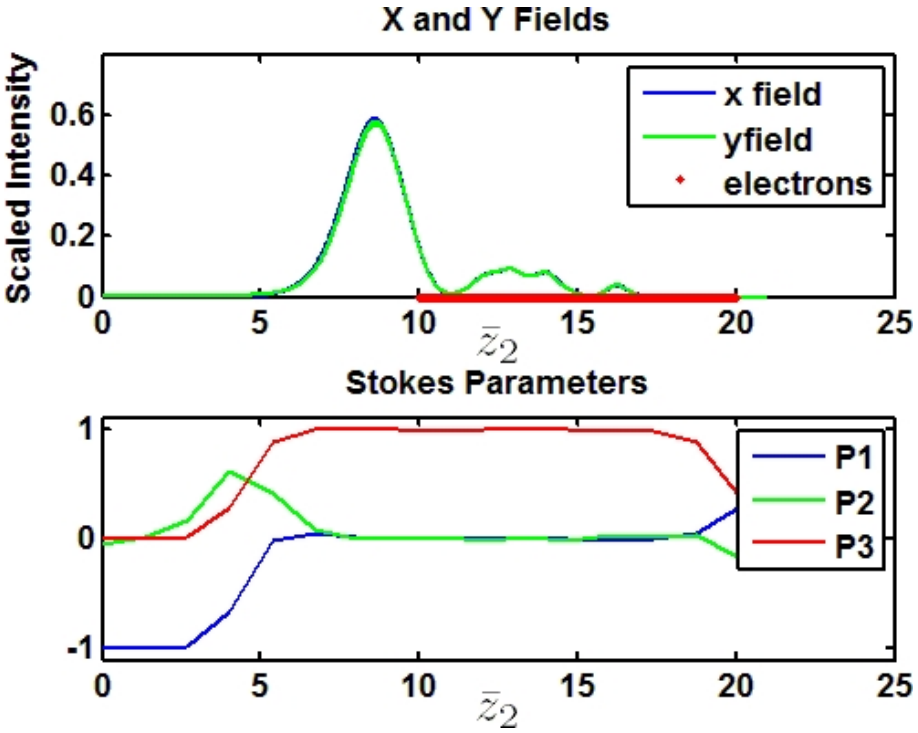

Figure 5.10: The same two plots as in figure 5.8, now using an undulator of helical polarization, $f_x = 1, f_y = 1$. All other parameters are the same.

polarization. The FEL parameter $\rho = 0.0796$, and the electron pulse length in $\bar{z}_2$ is $\frac{4\pi\rho}{10}$, where $4\pi\rho$ is the resonant FEL wavelength in the scaled $\bar{z}_2$ frame. The size of the electron pulse should mean that the electrons emit coherently with characteristics much like a single, super-charged electron. The blue lines show a planar undulator with $f_x = 1, f_y = 0$, the green corresponds to an elliptical undulator with $f_x = 1, f_y = 0.5$, and the red shows a helical with $f_x = f_y = 1$. Two plots are shown per undulator: the top shows the intensity, and the bottom shows the polarization ellipse for each case, formed by plotting A_x vs A_y. One would expect for the case $f_x = 1, f_y = 0$, from the Lorentz equation (3.12), that the electron pulse oscillate in, and thus produce a field in, the y axis. Increasing f_y to 0.5, one should also expect a slight oscillation in the x direction. The helical undulator should produce a circular polarized field. Note that in this figure the instantaneous intensity $A_x^2 + A_y^2$ is plotted with the fast oscillatory terms. It is not the more common time-averaged intensity. This is why the linear and elliptical intensities are oscillatory, and the circular polarized result shows a constant intensity.

Interestingly, the field polarization is solved self-consistently i.e. it is not predefined by assumption. The electrons will only interact with the appropriate part of the radiation field vector. For example, if the electrons oscillate in the y-direction and are seeded with an x-polarized field there will be no interaction.

To show this the electron pulse is seeded with a linear polarized field. Again, three simulations are performed with identical electron pulses but differently polarized undulators. The initial seed field, with a y polarization, is identical in all three. The electron pulse is of length $10l_c$, with a Gaussian distribution of standard deviation $\sigma_{z2} \approx 1.667$. The seed field envelope also has a Gaussian distribution with the same deviation.

In the first example a planar wiggler with $f_x = 0, f_y = 1$ is used, so the electrons oscillate in x and should not interact with the orthogonal seed. In the second the undulator polarization is $f_x = 0.5, f_y = 1$, and the third has $f_x = f_y = 1$.

Figures 5.8 - 5.10 plot the results. The top plot in each figure show the

intensity of the x (blue) and y (green) polarized fields. This time, the more common time-averaged intensity is shown. It is found by simply averaging the square of the field in each transverse direction over one radiation cycle in $\bar{z}_2$ about each point. The position of the electron pulse in $\bar{z}_2$ is indicated in red. There is no energy spread in the beam in this example: the purpose of the simulation is purely to illustrate the self-consistent evolution of the polarization in the code.

In the linear case, figure 5.8, the electron pulse passes through the undulator and is unaffected by the seed field. The seed is visible here in green, and remains unchanged from its initial state. The blue x field generated from noise is here barely visible on this scale. In the second example, for the elliptical polarized undulator, figure 5.9, the slight electron oscillation in y results in an energy exchange with the seed field. The seed causes a bunching of the electrons which then emit coherently according to the undulator polarization. The reduced intensity of the y field demonstrates that the electrons are generating and amplifying a field with elliptical polarization. The helical undulator case of figure 5.10 results in the same behaviour, but now identical intensities in x and y are generated.

To quantify the polarization, the Stokes parameters are shown in the bottom graphsof figures 5.8 - 5.10. If the x and y polarized electromagnetic fields are described in the form

$$E_x = E_{x0}\cos(\omega t) \tag{5.2}$$

$$E_y = E_{y0}\cos(\omega t + \delta), \tag{5.3}$$

where E_{x0}, E_{y0} are the amplitudes of the fields, ω is the angular frequency and δ is the phase difference between x and y, then the Stokes parameters are defined as

$$S_0 = \left\langle E_x^2 + E_y^2 \right\rangle \tag{5.4}$$

$$S_1 = \left\langle E_x^2 - E_y^2 \right\rangle \tag{5.5}$$

$$S_2 = \langle 2E_x E_y \cos(\delta) \rangle \tag{5.6}$$

$$S_3 = \langle 2E_x E_y \sin(\delta) \rangle \,. \tag{5.7}$$

where the brackets $\langle \ldots \rangle$ indicate an average over many wavelengths.

The normalised Stokes parameters are then [59]

$$P_1 = \frac{S_1}{S_0} \tag{5.8}$$

$$P_2 = \frac{S_2}{S_0} \tag{5.9}$$

$$P_3 = \frac{S_3}{S_0} \tag{5.10}$$

These measure the degree of linear polarization aligned across the x ($P_1 = 1$) and y ($P_1 = -1$) axis, the linear skew polarization at 45° ($P_2 = 1$) and 135° ($P_2 = -1$) angles to the x axis, and the right hand ($P_3 = 1$) and left hand ($P_3 = -1$) circular polarization in a given field. Since they are averaged quantities, $A_\perp$ is split into sections across $\bar{z}_2$, each 20 resonant periods long, within which the averaged Stokes parameters are calculated. This provides a way of observing how the polarization changes along the pulse in the longitudinal $\bar{z}_2$ coordinate.

The original y polarized seed field, shown in the intensity plot of figure 5.8, is located at $0 \leq \bar{z}_2 \leq 10$. The corresponding polarization plot on the bottom of figure 5.8 shows the polarization as $P_1 = -1$ in this region, correctly indicating the y polarization. The polarization then changes to $P_1 = 1$, an x polarized field, which is the polarization of the spontaneous emission from the electron pulse.

The Stokes parameters for the second and third examples in figures 5.9 and 5.10 show the seed field polarization changes according to the electron oscillation direction in the transverse plane. The peak of the seed field was at $\bar{z}_2 = 5$, which the Stokes parameters show is now almost completely circularly polarized in the helical case of figure 5.10.

5.3 Slippage Section/Chicanes

The code can model the effects of a series of multiple phase shifts and delays of the electron pulse with respect to the radiation field during propagation in the undulator. Each phase shift simulates the effect of a dispersive chicane with longitudinal shift in $\bar{z}_2$ and dispersive strength factor D. In this model, the FEL is composed of many modules, composed of an undulator section and a chicane, see

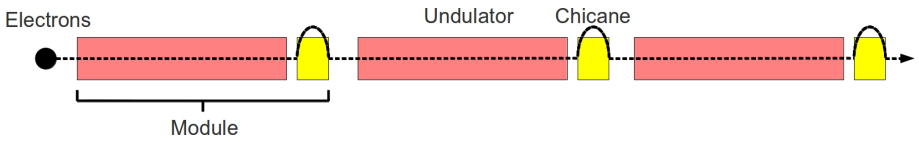

Figure 5.11: Illustration of an FEL composed of multiple unduator-chicane modules.

figure 5.11. Each chicane adds a delay to the electron beam with respect to the radiation field. The phase shifts are applied at intervals specified by a lattice file, and the nth line of the lattice file corresponds to the nth wiggler-chicane module. Each line specifies the number of wiggler periods in the undulator section, and then the number of resonant wavelengths the electron beam is delayed by due to the chicane with respect to the radiation field.

As the electrons travel through the chicane, they may be travelling at different longitudinal velocities, which, if they propagate freely, will result in a change in their position with respect to the average position of the electron beam. This process of dispersion is controlled here by a dispersive strength parameter D of the chicane, which is used to artificially give "more" or "less" dispersion. A larger value of D means the electrons will deviate further from their relative positions according to their differences in energy. The change in $\bar{z}_2$ due to the dispersion process and the delay δ is given by

$$\bar{z}_{2j} = \bar{z}_{2j0} - D\frac{(1 - p_{2j})}{2\rho} + \delta \tag{5.11}$$

where δ is the average longitudinal shift of the beam in $\bar{z}_2$ without dispersion due to the chicane. In order to illustrate and test the effects of this, the code is run in the 1D limit for this sub-section.

By applying periodic shifts to the electron beam by utilizing multiple undulator-chicane modules, one can generate a frequency comb, with frequency mode spacing determined by the total slippage in each undulator/chicane module [36]. The modal envelope is equal to the usual FEL spectrum for one undulator module. These modes can be locked with a periodic modulation on parameters, e.g. by supplying a modulation on electron beam energy. The mode-locked FEL is predicted to generate X-ray attosecond pulse trains from an FEL [36].

An unaveraged code may be better equipped than an averaged code to simulate the mode-locked FEL due to its enhanced frequency range. Indeed, the unaveraged 1D simulations of the mode-locked FEL predict significantly higher output intensities and substantially shorter radiation pulse widths than the averaged simulations [60].

To check the generation of modes in this code, an electron beam of length $l_{\bar{z}2} = 50$, and Gaussian charge distribution with $\sigma_{z2} \approx 8.3$ and bunch charge $1nC$ is propagated through a helical undulator, with $\rho = 0.005$. Each module contains an undulator of 8 periods, followed by a chicane which delays the electron bunch a further 23 undulator periods with respect to the radiation. The total slippage in each module is therefore $31 \times 4\pi\rho$ in $\bar{z}_2$. The beam passes through 18 such undulator-chicane modules. Figure 5.12 shows the scaled intensity spectrum of the combined x and y fields. Here $D = 0$, so the electron beam is simply being delayed without dispersion. The modes are not locked in this example.

According to [36], the spacing of the generated modes in the scaled $\bar{z}_2$ frame should be $\Delta\omega_{z2} = 3.2258$. The frequency axis is scaled so the fundamental appears at 1 by multiplying the frequencies by 2ρ, and so in this case the spacing should be 0.0323. This is observed in the result shown in figure 5.12, so the modes are being generated as predicted.

More generally, this functionality allows for easy modification to allow a more general transformation to be applied to the electron coordinates at intervals specified by the user in the lattice file. This allows for the opportunity in the future to easily insert e.g. FODO focusing quadrupoles periodically, to allow a more realistic transverse focusing of the electron beam.

5.3.1 3D Broadband Model

Due to not performing the SVEA, the code is capable of modelling the full radiation spectrum self-consistently in 3 dimensions. It is limited only by the sampling period specified by the user via the Nyquist condition [61]. As the code is in 3D, it simulates the transverse intensity profile of the radiation. Coupling to harmonics through betatron motion and Fourier components from the shape of the electron

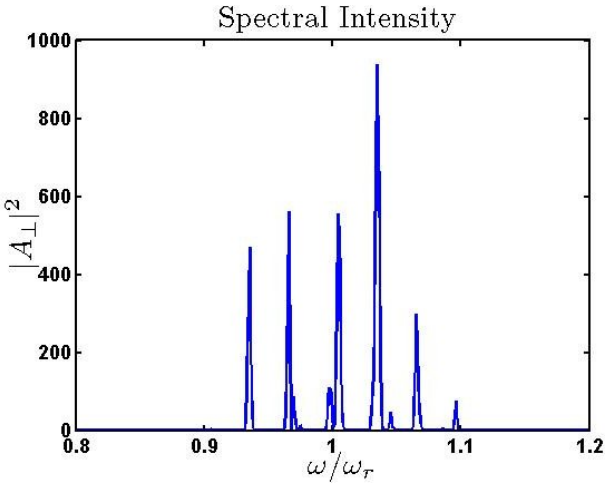

Figure 5.12: The spectral intensity of the field resulting from an electron beam undergoing periodic phase shifts in an undulator. The electron beam has passed through a sequence of 18 modules, each comprised of an 8 period undulator, and a chicane which then delays the electron pulse by 23 undulator periods. In such a scheme, it is expected the radiation field will develop a series of modes centered on ω_r with spacing $\Delta\omega/\omega_r = 0.0323$. The spectrum here displays such a spacing.

bunch are also simulated, due to the fundamental nature of the equations solved.

In the example, now presented to demonstrate some of these effects, another electron pulse a fraction of a resonant wavelength in length ($\sigma_{z2} \approx \lambda_r/60$) is used to radiate coherently much as in figure 5.7, but now in 3D, in a longer undulator. The undulator is 50 periods long with $\bar{a}_w = 2$ and undulator polarization $f_x = 1, f_y = 0$, so the electrons oscillate and generate a field in y. The feedback process onto the electrons is artificially switched off here to show only the spontaneous undulator spectrum.

Figure 5.13 shows the spectral intensity of the y field along the $\bar{z}_2$ axis in the center of the transverse plane at $\bar{x} = 0, \bar{y} = 0$ (in blue), and slightly off from center at $\bar{x} = 0, \bar{y} = 0.3796$ (in red). The frequency axis is scaled to ω/ω_r, so the resonant frequency is at 1. The field at $\bar{x} = \bar{y} = 0$ exhibits strong emission at the odd harmonics of the fundamental. Note the presence of even harmonics away from the center in the red line, as expected in a planar undulator.

The bandwidth of the fundamental at $\bar{x} = 0, \bar{y} = 0$ is shown in figure 5.14. The radiation generated in an undulator is expected to have a bandwidth of

$$\frac{\delta\omega_n}{\omega_n} = \frac{1}{nN_w}, \tag{5.12}$$

where n indicates the n^{th} harmonic of the resonant frequency ω_r and $\delta\omega_n$ is the frequency range from the peak emission at ω_n to the minimum caused by the interference effect [2]. In this example $N_w = 50$, so the resonant frequency should have a bandwidth of $\approx \frac{1}{50} = 0.02$. This is seen to be the case, indicated in figure 5.14.

The bandwidths of the 3^{rd} and 5^{th} harmonics of the field at $\bar{x} = 0, \bar{y} = 0$ are shown in figures 5.15 and 5.16 respectively. As the frequency axis is scaled to $\frac{\omega}{\omega_r}$, what is shown in these figures is $\frac{\delta\omega_n}{\omega_r}$. As $\omega_n = n\omega_r$, from equation (5.12), $\frac{\delta\omega_n}{\omega_r} = \frac{1}{N_w}$, which is the same for all harmonics. So the bandwidth of the 3^{rd} and 5^{th} harmonics should be the same as the 1^{st} harmonic in these units. Figure 5.15 and 5.16 give good agreement with this.

To see the 3D field properties of the harmonics, the field is filtered with a narrow band-pass filter centered around the desired frequency. Figure 5.17 shows

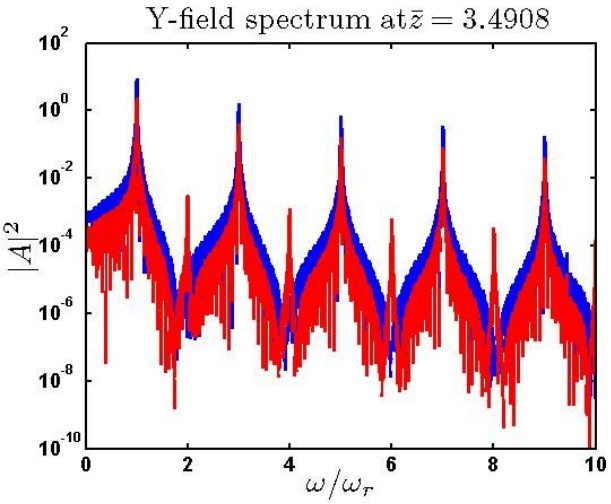

Figure 5.13: Spectrum of the y-polarized field. The blue line shows the on-axis field, and the red line is the field at point $\bar{x} = 0, \bar{y} = 0.3796$. Note the even harmonics are only present off-axis. The phase-front of the y-polarized field of the second harmonic at a transverse slice in $\bar{z}_2$. It exhibits the expected double-lobed structure.

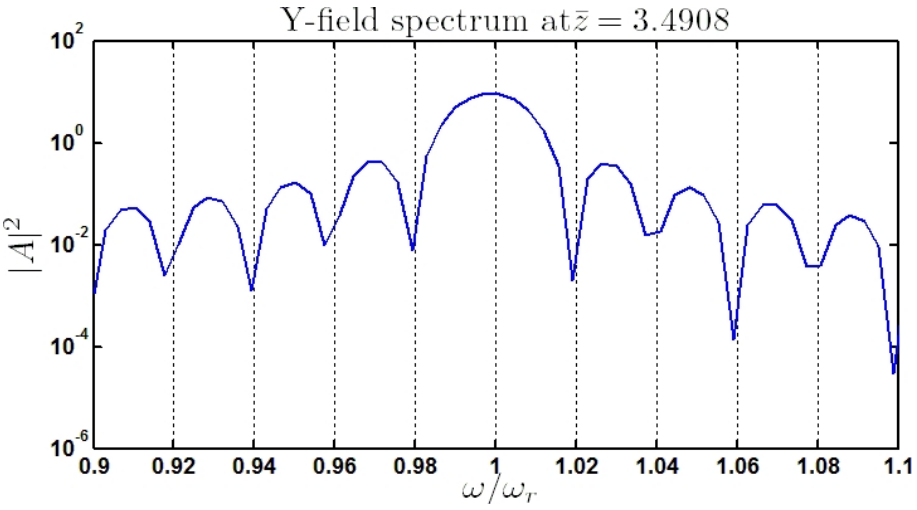

Figure 5.14: Spectrum of the y-polarized field, showing detail about the resonant frequency.

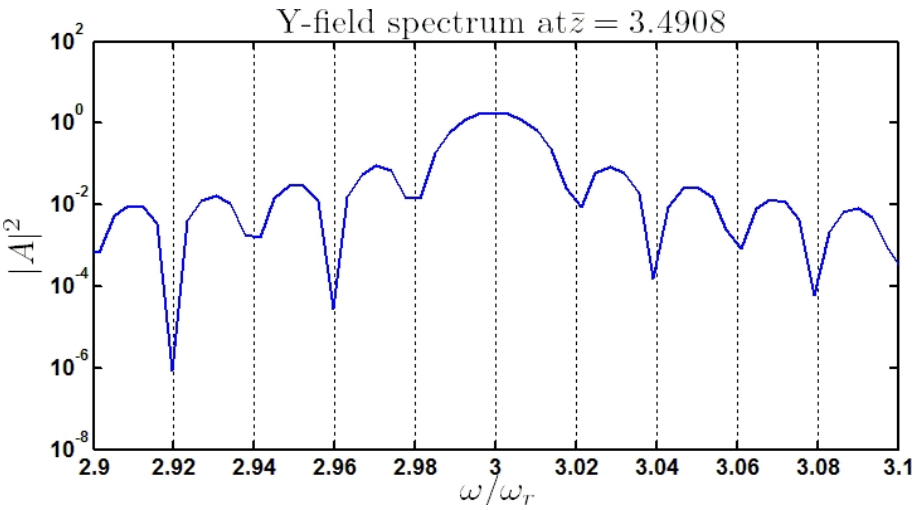

Figure 5.15: Spectrum of the y-polarized field, showing detail about the 3^{rd} harmonic of the resonant frequency.

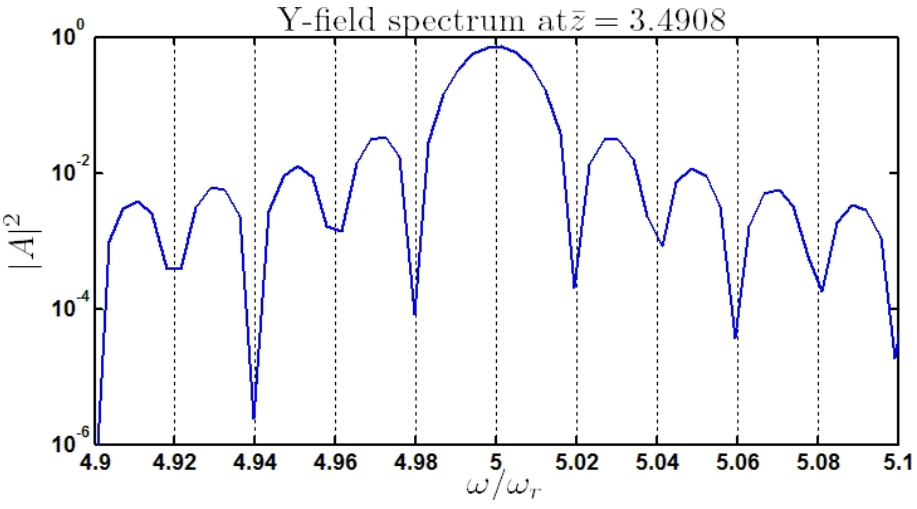

Figure 5.16: Spectrum of the y-polarized field, showing detail about the 5^{th} harmonic of the resonant frequency.

a transverse slice of the y polarized field on the left and the transverse intensity on the right, both filtered about the second harmonic, at the same fixed point in $\bar{z}_2$. Both the phase front and the intensity show the expected double-lobed structure, typical of even harmonics in the planar undulator [2], with no emission on-axis.

5.4 3D Effects

5.4.1 Emittance and Diffraction

The main 3D effects which will inhibit the gain process in the FEL over those in a 1D model are the field diffraction and electron beam emittance. These effects can be tested in isolation to check the validity of the simulation code.

Diffraction is tested by initializing a Gaussian field in the transverse plane, constant along $\bar{z}_2$, and propagating 1 Rayleigh length with the field generation from the electrons artificially switched off. The field radius should increase by $\sqrt{2}$. From the equation for the Rayleigh range as a function of frequency, equation (4.34), the Rayleigh range of the resonant wavelength, which is $4\pi\rho$ in the $\bar{z}_2$ frame, is

$$\bar{z}_R = \frac{\sigma_{\bar{x}0}^2}{2\rho} \tag{5.13}$$

So for $\sigma_{\bar{x}0} = \sigma_{\bar{y}0} = 0.4$ and $\rho = 0.008$, $\bar{z}_R \approx 10.05$. Figure 5.18 shows the initial (top) and final (bottom) transverse intensity profile, after propagating to $\bar{z}_R$. The result is typical of every transverse slice in $\bar{z}_2$. The reduction in intensity and broadening of σ_x is evident. To evaluate this more clearly, the intensity along the $\bar{x}$ axis at $\bar{y} = 0$ is in figure 5.19. The waist of the transverse intensity, which is at $1/e^2$ of the peak, is seen to increase by $\sqrt{2}$, showing the diffraction is being simulated correctly.

The electron beam emittance and focusing can be checked by matching the transverse dimensions of the electron beam to the undulator focusing channel.

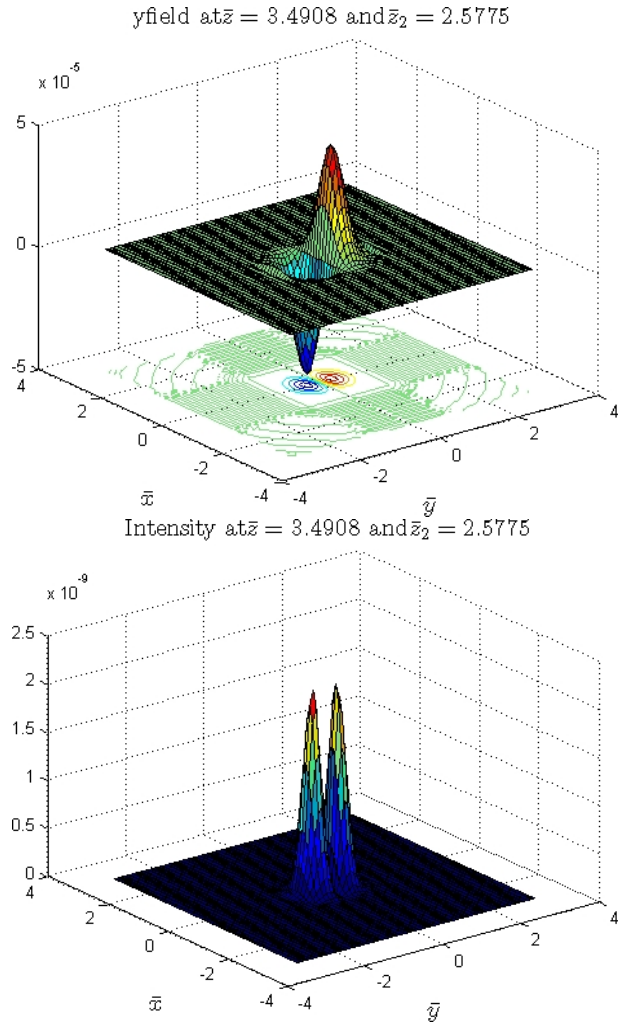

Figure 5.17: The top shows the phase-front of the y-polarized field of the second harmonic at a transverse slice in $\bar{z}_2$, and the bottom plot shows the intensity in the same slice. It exhibits the expected double-lobed structure.

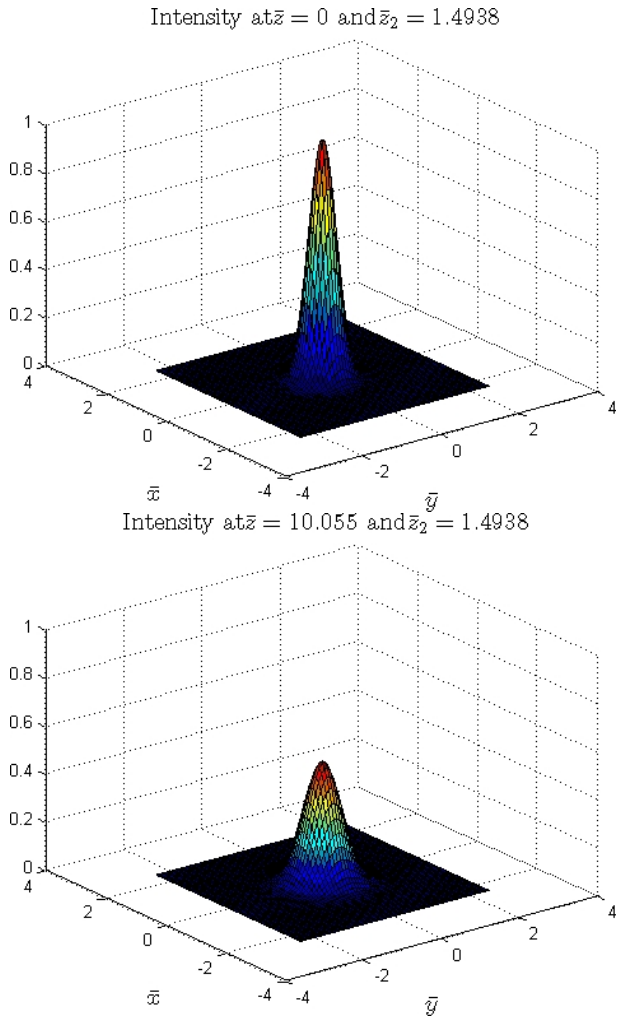

Figure 5.18: Plot on top shows the initial intensity, identical at all transverse slices in $\bar{z}_2$. The plot on the bottom shows the intensity after one Rayleigh length, and the intensity is seen to have diffracted to twice its original area.

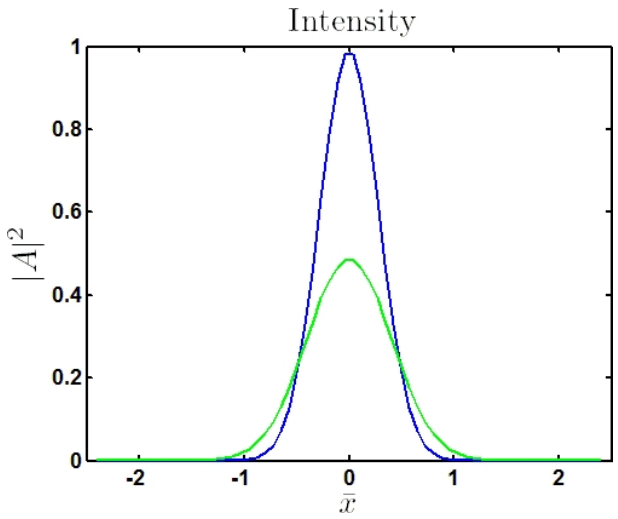

Figure 5.19: Figure showing the broadening of the transverse intensity profile due to diffraction. The intensity is shown at $\bar{y} = 0$, the center of the $\bar{y}$ axis, varying along the $\bar{x}$ axis. The blue line is the initial intensity at $\bar{z} = 0$, the green line is the intensity after one Rayleigh length at $\bar{z}_R$. The intensity waist has increased by $\sqrt{2}$ after a Rayleigh range.

The electron beam radius should then remain constant. The parameters used are

$$\rho = 0.01, \bar{\epsilon} = 1, \bar{a}_w = 1.5, f_x = f_y = 1,$$
$$\gamma_r = 500, \lambda_w = 0.015m, f = 0.4$$

Following the procedure of beam matching in section 4.3, the scaled matched beam radius should be $\bar{r}_m \approx 0.96$, with an initial radius of $3\bar{\sigma}_x \approx 0.68$. The initial momentum spread in the transverse directions is $3\bar{\sigma}_{px} \approx 0.33$. The field evolution and interaction is artificially switched off, so the electrons travel unpeturbed through the wiggler. This allows the effect of only the focusing channel and the undulator on the electron motion to be observed.

Plots of $\bar{x}$ vs $\bar{p}_x$ are shown in the top two plots of figure 5.20. The beam is initialized in a square grid as shown in the first plot. As a consequence, as the beam rotates in phase space due to the focusing channel there will be a small oscillation in the radius from the corners between the initial radius and the maximum radius $\bar{r}_m$. The oscillation should have a period of $\bar{\lambda}_\beta/4$, where

$\bar{\lambda}_\beta = 2\pi/\bar{k}_\beta$ is the period of the betatron oscillations in $\bar{z}$. The definition of $\bar{k}_\beta$ is in equation (3.76), and in this case, $\lambda_\beta = 16.755$. This behaviour is shown in the bottom plot in figure 5.20, which shows the radius of the beam in $\bar{x}$ as a function of propagation distance $\bar{z}$. The radius is found simply by the maximum electron position in $\bar{x}$. It should be noted that this does not indicate that the charge distribution in the transverse dimensions remains constant, only that that electrons will not travel outside the beam envelope specified by the maximum radius.

It should also be noted that the square beam used can be made circular by neglecting the electrons whose χ_k weighting falls below a certain percentage of the maximum. Then the macro-electrons at the corners of the phase space distribution may be ignored. The code has this capability but it was not employed here.

5.4.2 SACSE in a Helical Wiggler in 3D

A full 3D simulation exhibiting Self Amplified Coherent Spontaneous Emission is presented.

An electron beam 6 cooperation lengths long, with a flat-top current distribution in $\bar{z}_2$ and a Gaussian current distribution in $\bar{x}$ and $\bar{y}$ is injected through an undulator with the following parameters:

$$\rho = 0.00556, \bar{\epsilon} = 0.3, \bar{a}_w = 1.0, f_x = f_y = 1,$$
$$\gamma_r = 700, \lambda_w = 0.008m, f = \sqrt{2}$$

As in the previous 1D SACSE cases, the electron pulse should emit coherent radiation strongly from its edges, which have a large current gradient. In this high slippage/short pulse regime, the coherent emission from the rear of the electron pulse should propagate over the electron pulse and consequently be amplified. Both a 1D and a 3D simulation are performed for comparison, to observe the deleterious effects the diffraction has on the amplification.

If the Rayleigh length of the resonant wavelength $z_R(k_r) \lesssim l_g$, then the diffraction will be significant during an FEL exponential gain length. In the scaled

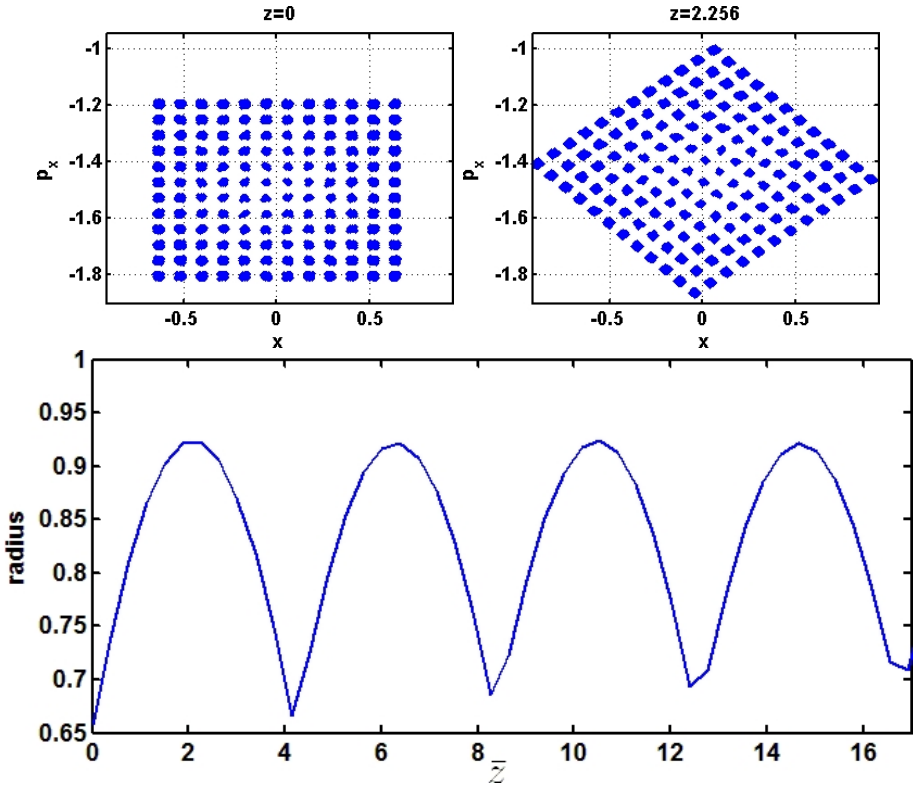

Figure 5.20: Figure showing the rotation in transverse phase space of the focused electron beam and the resulting oscillation of the radius of the beam. The first graph on the top left plots the scaled x momentum $\bar{p}_x$ vs $\bar{x}$, and shows the electron beam at $\bar{z} = 0$, initialized on a square grid. The plot on the top right shows the same view at $\bar{z} = 3.384$, and the electron beam is shown to have rotated in the $\bar{x}$ phase space. This results in an oscillation in the electron beam radius in $\bar{x}$ as the electrons at the corners sweep around. The beam radius in $\bar{x}$ is shown varying along the propagation distance $\bar{z}$ in the bottom plot, and the oscillation has a period of quarter the betatron period $\bar{\lambda}_\beta$. The maximum is just below the matched beam radius calculated in equation (4.27).

variables this becomes

$$\bar{z}_R \lesssim 1. \tag{5.14}$$

The electron beam is matched to the undulator, so its radius is given by equation (3.80), and the Rayleigh range of the resonant wavelength for initial radius equal to the matched electron beam radius $\bar{\sigma}_b$ is given in equation (5.13). So equation (5.14) becomes

$$\bar{\sigma}_b^2 \lesssim 2\rho \tag{5.15}$$

$$\Rightarrow \frac{\sigma_b^2}{l_g l_c} \lesssim 2\rho, \tag{5.16}$$

and then from the definition of the matched transverse radius in equation (3.80),

$$\epsilon_n \lesssim 2\rho l_g l_c \gamma_r k_\beta. \tag{5.17}$$

The coherence length definition (in figure 3.2) is $l_c = \dfrac{\lambda_r}{4\pi\rho}$, so equation 5.17 becomes

$$\epsilon_n \lesssim \frac{\gamma_r \lambda_r}{2\pi} l_g \gamma_r k_\beta. \tag{5.18}$$

and if $k_\beta l_g \sim 1$, so that $\lambda_\beta \sim 2\pi l_g$, then, broadly speaking, if

$$\epsilon \lesssim \frac{\lambda_r}{2\pi} \tag{5.19}$$

then diffraction may be considered significant within a gain length.

In the scaled notation, remembering the definition of the scaled transverse emittance $\bar{\epsilon} = \dfrac{\epsilon}{2\rho l_c}$ from equation (3.81), this condition becomes

$$\bar{\epsilon} \lesssim 1 \tag{5.20}$$

for significant diffraction.

In this simulation, $\bar{\epsilon} = 0.3$, so one can expect diffraction to negatively impact upon the lasing. For a source of matched transverse size the Rayleigh range of the resonant wavelength is, in terms of the scaled emittance,

$$\bar{z}_R = \frac{\bar{\epsilon}}{\bar{k}_\beta}, \tag{5.21}$$

which is 3.3 with these parameters. This is above but still on the order of a gain length.

The electron betatron wavelength $\lambda_\beta \approx 70 l_g$ in this case. In addition to effecting the initial radius of the emitted radiation and thus the diffraction, the electron emittance induces a longitudinal energy spread in the beam which also degrades the amplification. The induced spread is calculated in [33] as

$$\sigma_\epsilon = \frac{k_r \bar{a}_w f \epsilon}{4\gamma_r} \tag{5.22}$$

which can be expressed in terms of the scaled emittance, using equation (3.81), as

$$\sigma_\epsilon = \frac{\bar{a}_w f \bar{\epsilon}}{4\gamma_r} \tag{5.23}$$

The total effective energy spread due to both the longitudinal and transverse emittance is then

$$\sigma_T = \sqrt{\sigma_\gamma^2 + \sigma_\epsilon^2}, \tag{5.24}$$

where σ_γ is the usual 1D energy spread. This total effective spread must be used to satisfy the condition for lasing, so that

$$\sigma_T < \rho. \tag{5.25}$$

In this simulation a longitudinal energy spread of 0.001 is used, which combined with the induced energy spread calculated using equation (5.23), gives a total effective spread of $\sigma_T \approx 1.005 \times 10^{-3} < \rho$. The energy spread induced from the emittance does therefore not seem to be significant compared to σ_γ. It is likely then, that the transverse energy spread will not reduce the amplification. A charge redistribution in the transverse directions due to the emittance may still affect the interaction, due to electrons oscillating in and out of resonance, and physically oscillating outside the radiation field radius. However, as $\bar{\lambda}_\beta$ is large compared with the gain length and the entire undulator length, any deleterious effects are likely to mostly be due to diffraction.

The result of the simulation is shown in figures 5.21 and 5.22. Shown are the power, intensity at the center of the transverse plane $\bar{x} = 0, \bar{y} = 0$, where the intensity will be at a maximum, and the transverse intensity at a fixed point in $\bar{z}_2$. The intensity in 3D, with a Gaussian transverse charge distribution centered on $\bar{x}, \bar{y} = 0$, will generate a maximum radiation intensity at $\bar{x}, \bar{y} = 0$. The electrons in the center of the Gaussian, with resonant energy, before noise is added, will have electron weight $\chi_k = 1$. The 1D case, as it is a flat-top current distribution, will also have $\chi_k = 1$ before noise. The intensity produced in the center of the Gaussian is compared with the 1D simulation. These plots are shown at propagation distances $\bar{z} \approx 4$ and $\bar{z} \approx 8$.

It is important to recall that the radiation field has a high band-pass filter applied to stop the diffraction problems outlined earlier. Here the filter omits frequencies below $\approx 1/3^{rd}$ of the resonant frequency. The same filter is applied to the 1D case also, to allow an equivalent comparison. The filtering removes the low frequency components whose interference with the resonant wavelengths cause the oscillation in the radiation envelope of the resonant frequency observed in for example the simulation presented in figure 5.4 and [45]. Thus the CSE is observed as a constant intensity emitted from the sharp edges of the electron pulse.

The plots at the beginning of the interaction, in figure 5.21, display the CSE, here already showing some amplification. The electron beam lies between $4 \leq \bar{z}_2 \leq 10$, and the radiation from $\bar{z}_2 = 0$ to 4 is the CSE fom the front edge of the pulse, having travelled ahead into free space. The rear of the pulse from $\bar{z}_2 = 6$ to 10 is in the slippage region, and the CSE has begun to be amplified. The region $\bar{z}_2 = 4 \rightarrow 6$ is still evolving from noise, and a transverse intensity slice taken from this region shows a noisy multi-mode transverse intensity structure, as expected [32].

Further into the interaction, in figure 5.22, the expected amplification is observed, albeit significantly smaller than in the corresponding 1D case. The electron pulse now lies between $\bar{z}_2 \approx 8$ and ≈ 14, and the system is dominated entirely by slippage. The CSE from the tail of the pulse, now at $\bar{z}_2 = 14$, has

been amplified as it travels over the pulse. The diffraction of the CSE in the 3D case has hindered the interaction, showing the importance of the 3D model in this example.

Another 2 simulations have been performed, with $\bar{\epsilon} = 0.5$ and $\bar{\epsilon} = 1.0$. The other parameters are kept the same. The FEL parameter ρ is being held constant here, although by increasing the beam emittance this should be reduced due to a larger beam diameter. It has been held constant to show the effects of only the increasing emittance.

It can be seen in the equation for the Rayleigh range (5.21) that as $\bar{\epsilon}$ increases, the Rayleigh range also increases, reducing the diffraction and the negative impact on the gain from diffraction. However it is seen from equation for the energy spread induce by the emittance (5.23) that the effective energy spread will also increase, which inhibits the interaction further. The condition for the allowed frequencies due to low frequency diffraction in equation (4.38) shows that the frequency cutoff is relaxed for larger initial radii. However, for comparison, the same frequency cutoff as the case when $\bar{\epsilon} = 0.3$ is kept in the simulations where $\bar{\epsilon} = 0.5$ and $\bar{\epsilon} = 1$.

The results presented here are also compared to 1D equivalent simulations, but this time, in an attempt to simulate the decoupling due to the effective induced spread, the total effective spread induced by the emittance is taken into account in each of the 1D models. When $\bar{\epsilon} = 1$, from equation (5.24) the total spread $\sigma_T = 0.0011$, and when $\bar{\epsilon} = 0.5$, $\sigma_T = 0.0010308$. These correspond to spreads in $\bar{p}_2$ of $\sigma_{p2} = 0.0022$ and 0.0010308, respectively. These are the Gaussian energy spreads in p_{z2} used in the 1D simulations.

Figures 5.23 - 5.25 show the comparisons for each of the three 3D simulations. The simulations have been run to $\bar{z} \approx 4$. Figure 5.23 shows the case where $\bar{\epsilon} = 0.3$, figure 5.24 shows the result of using $\bar{\epsilon} = 0.5$, and figure 5.24 has $\bar{\epsilon} = 1.0$. One can see that as the emittance is increased, the difference between the 1D case and the 3D case reduces, and for $\bar{\epsilon} = 1$, the solution is very similar. The effects of diffraction are reducing, since the Rayleigh range for each case is longer with increasing emittance. $\bar{z}_R = 3.3$ for the case where $\bar{\epsilon} = 0.3$, $\bar{z}_R = 5.5$ for $\bar{\epsilon} = 0.5$

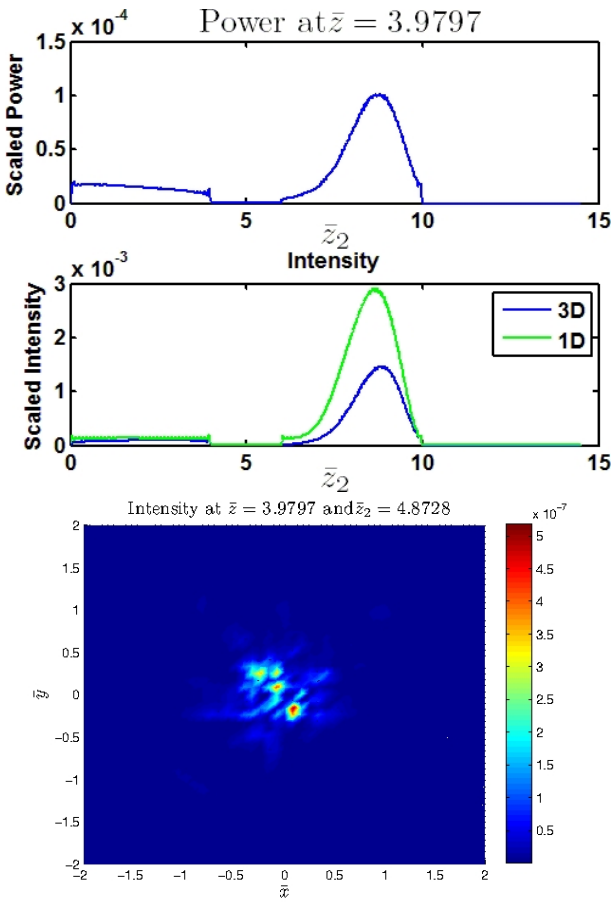

Figure 5.21: 1st plot: Scaled power, which is the scaled intensity integrated over $\bar{x}$ and $\bar{y}$. 2nd plot: The intensity in the center of the radiation field i.e. $\bar{x} = 0, \bar{y} = 0$, compared with the 1D intensity. 3rd plot: Transverse intensity slice at $\bar{z}_2 \approx 5$, showing a noisy transverse mode structure.

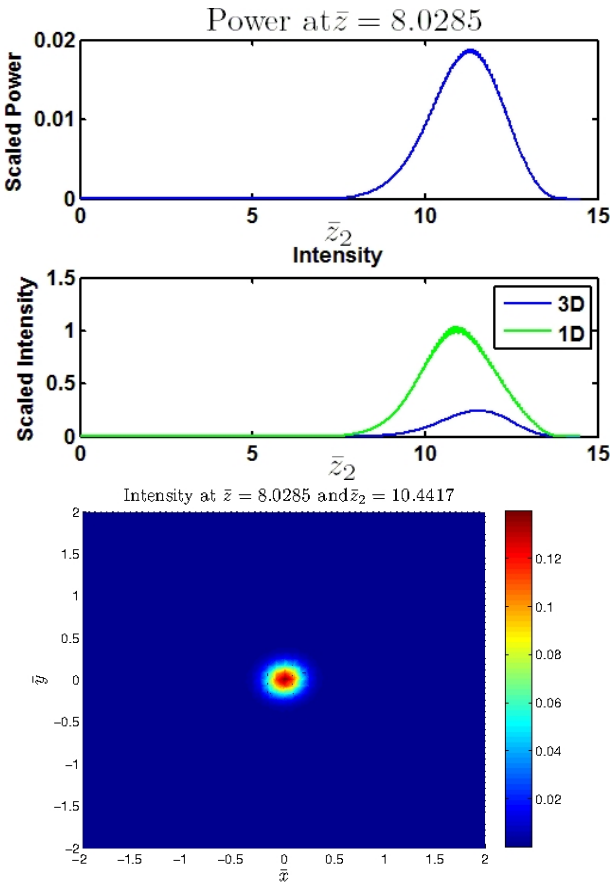

Figure 5.22: Equivalent plots as those in figure 5.21, with the electron pulse now propagated to $\bar{z} = 8$. Note the reduced intensity compared to the 1D case, and the single transverse mode in the bottom plot.

and $\bar{z}_R = 11.0$ for $\bar{\epsilon} = 1.0$. Examining the 1D plots, it is observed that the extra electron beam energy spread used to approximate the effective spread from the emittance has made negligible difference: the 1D plots are almost identical in all three examples. It may be a reasonable assumption then that the increase in Rayleigh length with increasing scaled emittance is causing the field to diffract less, and inhibiting the interaction less. It would seem that the main deleterious 3D effect in the example where $\bar{\epsilon} = 0.3$ is diffraction.

The equivalent energy spread approximated in equation 5.23 is applied to the 1D simulations as a spread about the resonant energy. In fact, this spread is induced such that γ_r is the **maximum** value. This is because the electrons travelling directly in the $\bar{z}$ direction only are resonant, and the electrons travelling at the same energy at a slight angle to the z-axis have a slighty reduced speed in z. This leads to a detuning, which further degrades the interaction. This has not been taken into account in the 1D case. There is also the physical decoupling as some electrons undergo large oscillations within the beam envelope due to the betatron motion, which cannot be taken into account in the 1D examples. As mentioned above, the wavelength of these oscillations is $\bar{\lambda}_\beta \approx 70$, and is the same for all three emittance cases. Thus, at the propagation distance $\bar{z} = 4$ presented in these comparisons, there will not have been significant deviations of the electrons from their initial positions in $\bar{x}$ and $\bar{y}$.

5.4.3 Short Chirped Pulse

Electron pulses produced by laser plasma accelerators for undulators can produce electron pulses with longitudinal duration on the order of a few resonant wavelengths. An electron beam of such small duration, with a strong negative chirp, may "flip" over in longitudinal phase space during propagation in the undulator.

During this process, the electron bunch will be smaller than a resonant wavelength, and consequently will radiate coherently for a number of undulator periods dependant on the magnitude of the chirp. For a stronger chirp, the electron pulse will radiate coherently for less undulator periods, giving a broader bandwidth.

This new effect is in fact not strictly speaking an FEL effect. It is a coherent

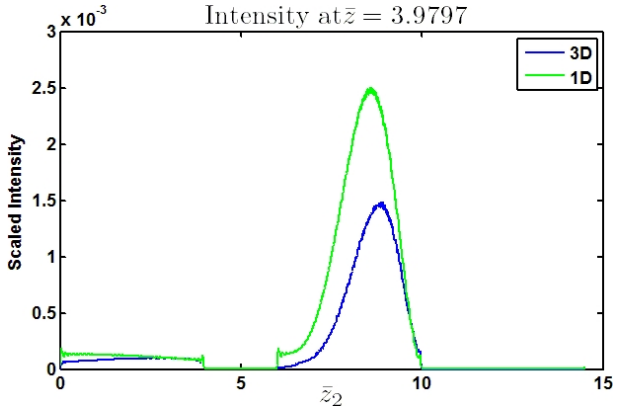

Figure 5.23: Comparison of intensity in the center of the transverse electron distribution at $\bar{x}, \bar{y} = 0$ of 3D (blue) case with 1D intensity (green) produced with the equivalent energy spread of $\sigma_{p2} = 2.01 \times 10^{-3}$ corresponding to $\bar{\epsilon} = 0.3$.

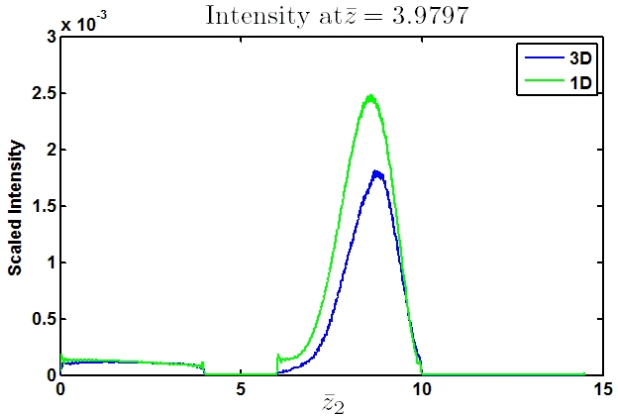

Figure 5.24: Comparison of intensity in the center of the transverse electron distribution at $\bar{x}, \bar{y} = 0$ of 3D (blue) case with 1D intensity (green) produced with the equivalent energy spread $\sigma_{p2} = 2.0616 \times 10^{-3}$ for the case where $\bar{\epsilon} = 0.5$.

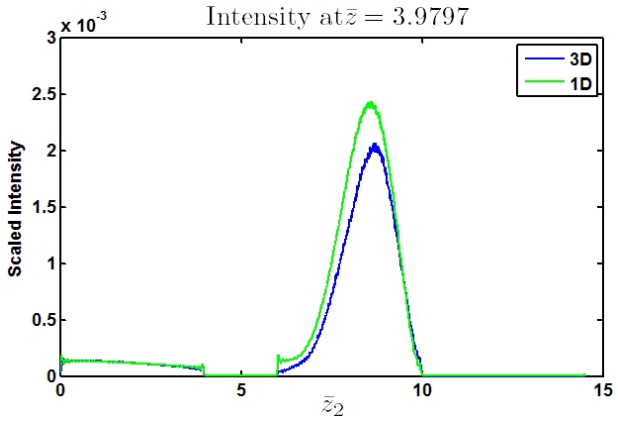

Figure 5.25: Comparison of intensity in the center of the transverse electron distribution at $\bar{x}, \bar{y} = 0$ of 3D (blue) case with 1D intensity (green) produced with the equivalent energy spread $\sigma_{p2} = 2.2 \times 10^{-3}$ for the case where $\bar{\epsilon} = 1.0$.

effect arising purely from the linear evolution of the electron beam due to the chirp. Nevertheless, this code is well suited to simulating it in 3D.

An analytic solution can be defined from the scaled equations as follows [62]. First of all an initial linear chirp, g_0, is defined in the electron beam such that

$$g_0 = \frac{dv_j}{d\bar{z}_2}, \tag{5.26}$$

where v_j is the j^{th} electron's phase velocity. Taking the initial electron beam distribution to be a Gaussian with rms spread σ_0, the spread after propagation distance $\bar{z}$ will then be

$$\sigma(\bar{z}) = \sigma_0 + g_0\sigma_0\bar{z} \tag{5.27}$$

$$\Rightarrow \sigma(\bar{z}) = \sigma_0(1 + g_0\bar{z}) \tag{5.28}$$

To prevent $\sigma(\bar{z})$ from becoming equal to zero from the perfect linear chirp, a small intrinsic pulse length σ_i is added such that

$$\sigma(\bar{z}) = \sqrt{\sigma_0^2(1 + g_0\bar{z})^2 + \sigma_i^2} \tag{5.29}$$

With an initial chirp and electron distribution defined in this way, the initial peak electron current $I_{pk} = \dfrac{Q}{\sqrt{2\pi}\sigma_0}$, and the electron weighting function, in 1D,

as a function of $\bar{z}$, can then be found to be

$$\chi(z,t) = \frac{I(\bar{z},\bar{z}_2)}{I_{pk}} \tag{5.30}$$

$$\chi(z,t) = \frac{\sigma_0}{\sqrt{\sigma_0^2(1+g_0 z)^2+\sigma_i^2}} \exp\left(-\frac{\bar{z}_2^2}{2(\sigma^2(1+g_0 z)^2+\sigma_i^2)}\right) \tag{5.31}$$

The predictable evolution of the electron distribution allows the field equation to be integrated over $\bar{z}$ to obtain an analytic solution for the field. The field equation used is the 1D field equation from [45], which is for a helical undulator in the Compton limit. The solution is obtained in Fourier space, and the final expression for the envelope as a function of $f = \omega/\omega_r$ is

$$\tilde{A}(f) = \frac{4\pi\rho}{f} \exp\left(-i\frac{f-1}{2\rho g_0}\right) \exp\left(-\frac{f^2\sigma_i^2}{8\rho^2}\right) \exp\left(-\frac{(f-1)^2}{2\sigma_0^2 g_0^2 f^2}\right) \tag{5.32}$$

Both a 1D and 3D simulation are presented here. The 1D simulation is presented to demonstrate the evolution of the field and electron beam on propagation. In the 3D case the electron beam is matched to the natural focusing channel in the undulator.

The following parameters were used to simulate this effect:

$$\rho = 0.008; a_w = 1.5; \gamma = 707; \lambda_w = 1.5cm$$
$$f_x = f_y = 1$$

The electron beam chirp $\frac{dp_{2j}}{d\bar{z}_2} = -0.192$, and the initial σ spread of the Gaussian distribution in $\bar{z}_2$ is $\sigma_{z2} = 0.333$. There is also an energy spread of $\sigma_{p2} = 0.0027$.

Figure 5.26 shows the evolution in phase space of the electron bunch, in 1D, and shows bunch compression and decompression due to the energy chirp. The corresponding 1D radiation intensity is also shown. As the electron pulse bunches to durations of the order of the resonant radiation wavelength, it radiates coherently. Recall that p_{2j} is the rate of change of the electron's $\bar{z}_2$ position, so that a higher value of p_{2j} means the electron will travel faster in the positive $\bar{z}_2$ direction. However, the $\bar{z}_2$ frame is the stationary radiation frame, so an electron

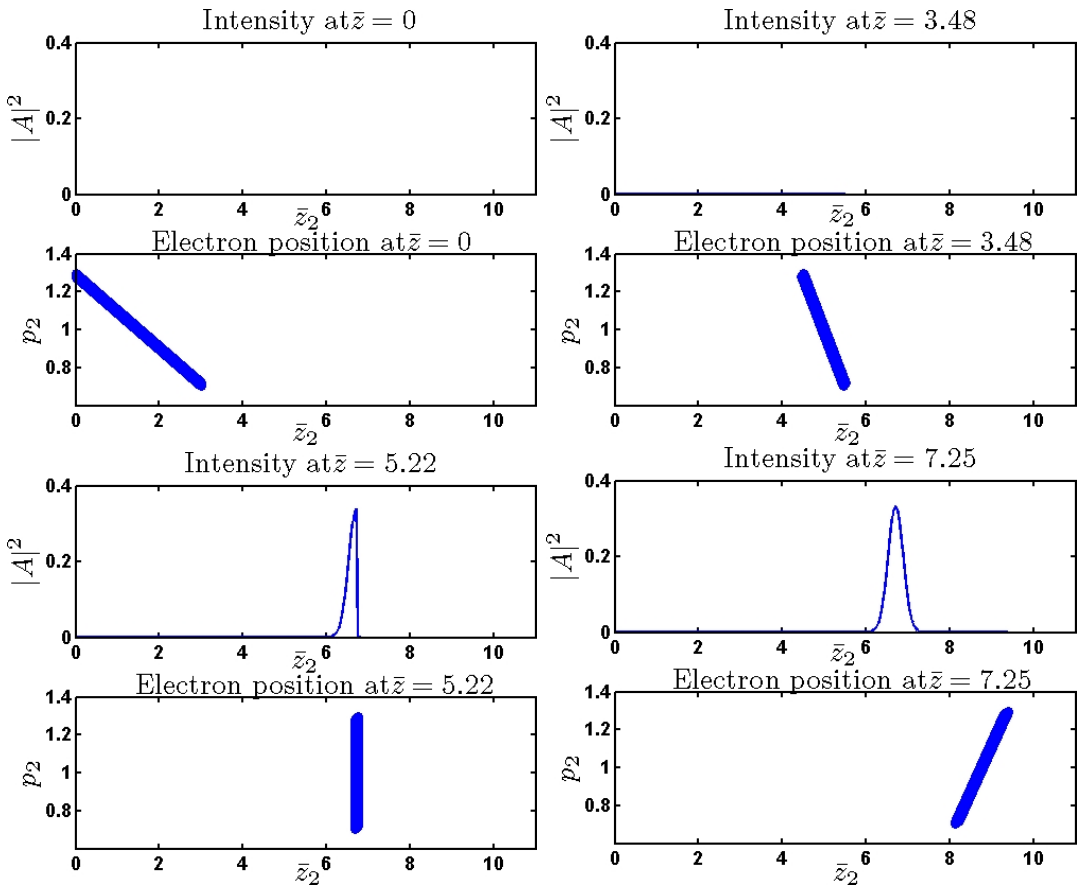

Figure 5.26: These 8 plots show the intensity and electron beam phase space at 4 different propagation distances. The initial chirp in the plot at $\bar{z} = 0$ in the top left causes the electron pulse to compress and then decompress. When it is bunched to a length in $\bar{z}_2$ of $\lesssim 4\pi\rho$ (that is to say, less than a resonant radiation wavelength) it generates a single coherent spike in intensity.

which is travelling faster from the front of the radiation at $\bar{z}_2 = 0$ is actually travelling slower in the lab frame: it is slipping backwards through the radiation more quickly. So, from the chirped electron beam in the top left of figure 5.26, the electrons at the front of the electron pulse at $\bar{z}_2 = 0$ have a smaller velocity in the direction of propagation than the electrons at the tail of the pulse. This causes the electrons to bunch. The phase space plot at $\bar{z} = 5.22$ in figure 5.26 shows the compressed electron bunch, and the resulting coherently emitted radiation spike is shown in the corresponding intensity plot.

Note that the final radiation pulse width, shown on the intensity plot at $\bar{z} = 7.25$ in figure 5.26, is slightly less than a cooperation length. Depending on the initial chirp, and thus the number of undulator periods the pulse is bunched for, the radiation pulse width may be significantly less than one cooperation length, which is smaller than pulse widths produced by the FEL process in SASE.

The radiation spectral output is shown in figure 5.27. Figure 5.28 shows the analytic prediction in equation (5.32) for the same parameters. The analytic and numerical solutions are seen to be in good agreement.

The 3D simulation, using the same parameters, is run with a scaled emittance of $\bar{\epsilon} = 0.8$, and the beam is matched to the undulator. This gives an effective energy spread, from equation (5.23), of $\sigma_\epsilon = 0.00064$, which is very small compared to the spread used in the 1D simulation. The betatron wavelength in $\bar{z}$ is $\bar{\lambda}_\beta = 67.01$ from equation (3.76), and the Rayleigh length of the resonant wavelength from equation (5.21) is $\bar{z}_R = 8.532$. Using these parameters then, it would be reasonable to assume the 3D effects will not sigificantly deviate from the 1D solution.

The scaled power in $\bar{z}_2$ and the transverse intensity slice near the coherently radiated peak are shown in figure 5.29 and figure 5.30. The sharp peak in the power indicates the region where the electron beam was strongly bunched and radiating coherently, at $6 \leq \bar{z}_2 \leq 7$. This is the same position as in the 1D case. The transverse intensity is seen to give a sharp peak on-axis.

Also shown is the scaled spectral intensity in the center of the transverse plane, in figure 5.31, and it again gives good agreement with the analytical solution in

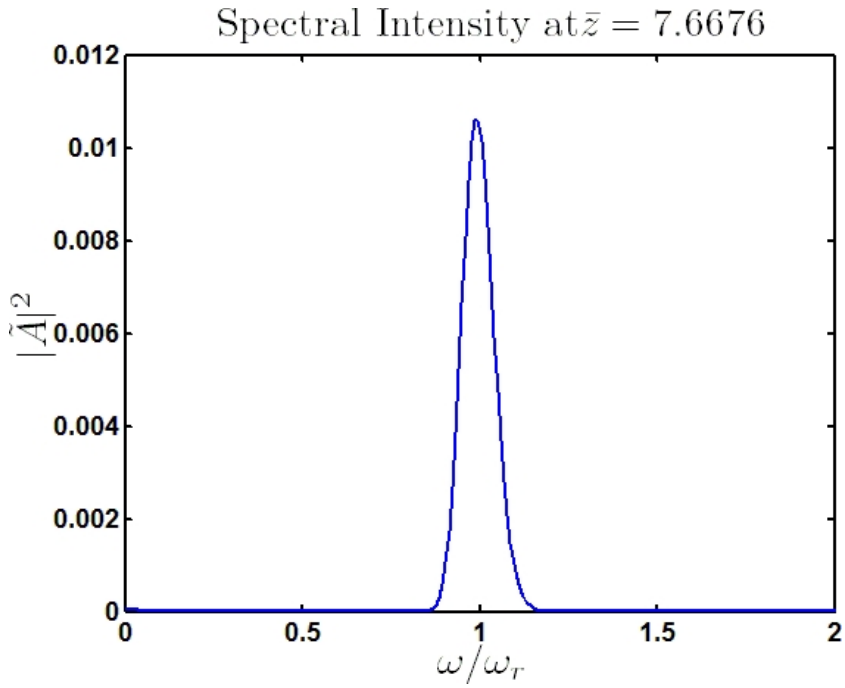

Figure 5.27: The intensity spectrum of the simulation presented in figure 5.26.

figure 5.28. The 3D effects have not significantly reduced the intensity, and the basic mechanism has not been degraded.

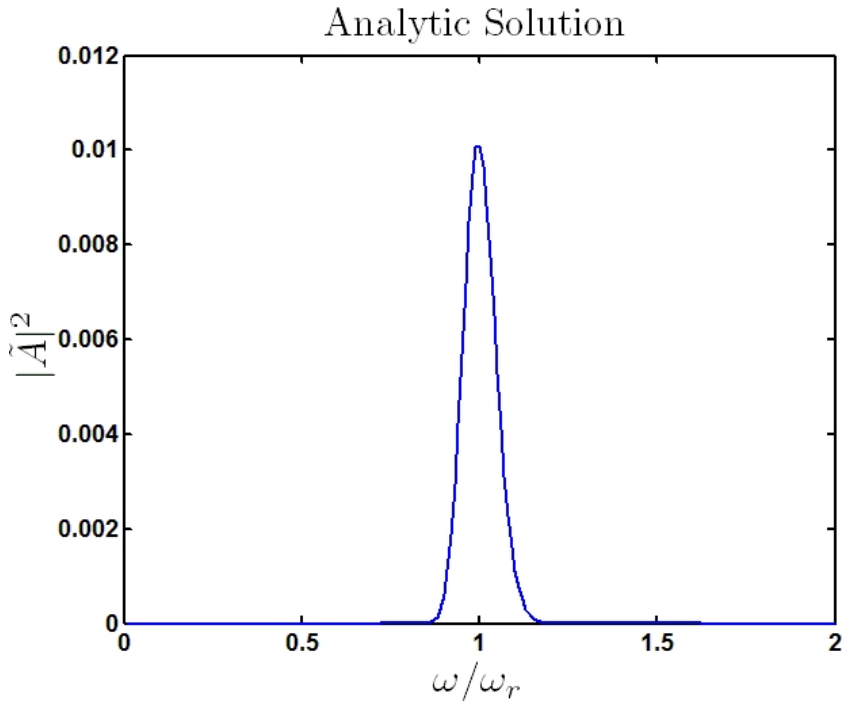

Figure 5.28: The analytic solution of the parameters used to produce the spectral intensity of the simulation plotted in figure 5.27.

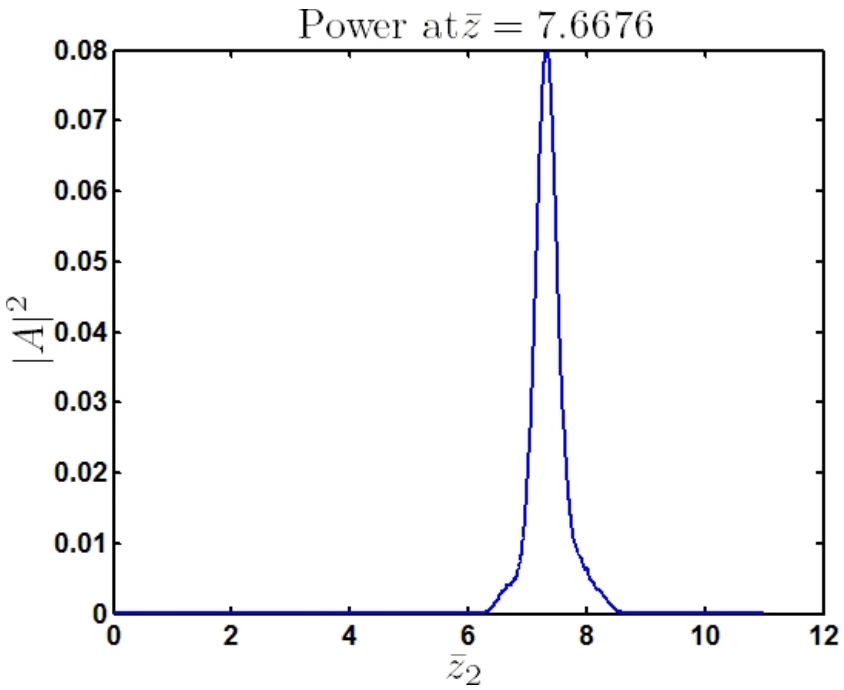

Figure 5.29: The power in $\bar{z}_2$ of the 3D simulation of the short chirped pulse.

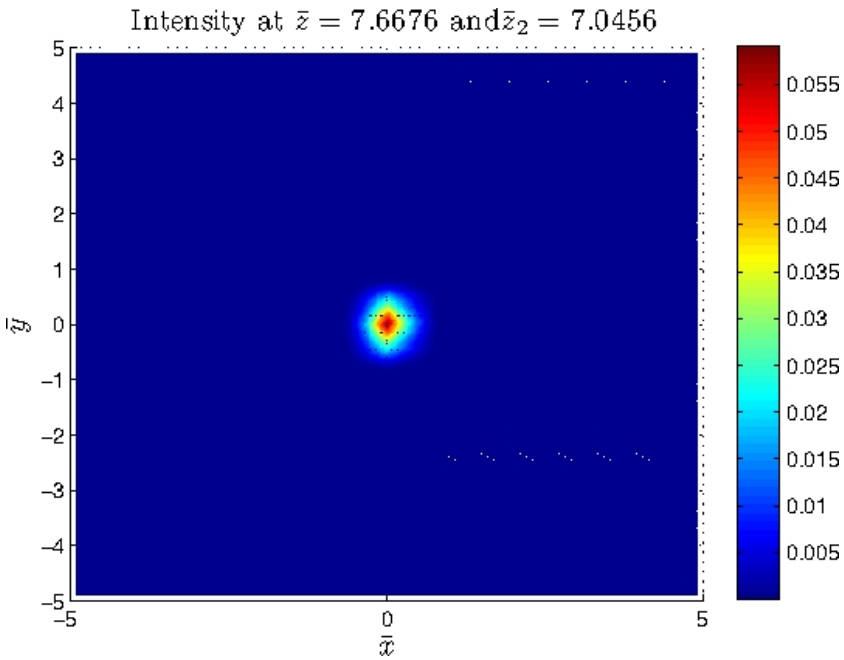

Figure 5.30: The transverse intensity profile near the peak power shown in figure 5.29.

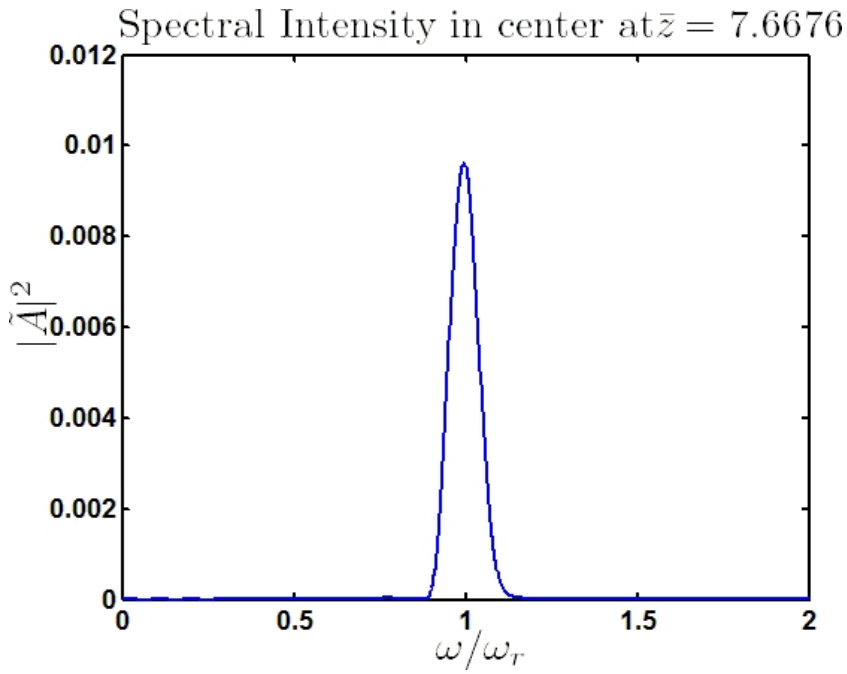

Figure 5.31: The spectral intensity along the $\bar{z}_2$ axis where $\bar{x} = 0$,$\bar{y} = 0$.

Chapter 6

Conclusions and Future Work

A new 3D mathematical model of the FEL has been developed which makes few limiting assumptions. In particular, the SVEA or Eikonal approximation is not applied, meaning the model can describe phenomena below the radiation wavelength scale. The model describes a variably polarized undulator and radiation field. Large changes in the initial electron positions may also be modelled.

The model is solved numerically by a parallel MPI code written in FORTRAN which balances the electron distribution uniformly amongst processors. The numerical solution requires the use of the Split-Step Fourier Method, which splits up the field diffraction and source terms into two separate steps. The diffraction solution uses Fourier transforms, which the code uses FFTW 2.1.5 to perform. The source term solution demands the use of a linear solver, so SuperLU _ DIST was used to accomplish this in parallel. The electron beam has been matched to a linear focusing channel so that its radius remains constant. A range of "active nodes" were chosen, which are the only nodes in the transverse plane which interact with the electrons. Using only these nodes to construct the stiffness matrix in the linear solver reduces both computational memory and time taken by the linear solver. The problem of diffracting long radiation wavelengths has been outlined, and a low frequency cutoff defined below which frequencies can not be modelled due to large diffraction. Frequencies below this cut-off are filtered out during each diffraction step in the code.

Results have been presented which shows the code agrees with previously established work. The polarization was shown to be solved self-consistently, and the diffraction and focusing effects were shown to be solved correctly. The 3D SACSE simulation presented could not have been performed in an averaged code. The 3D effects were shown to be important to the SACSE interaction.

There are a number of improvements which could be made to the code. The most immediate work which should be performed is the addition of boundary conditions to the diffraction solution, and the testing of different linear solvers to see which gives the best performance. The problem with the broadband diffraction limits the frequency range of the code, and places restrictions upon which FEL parameters may be modelled. The low frequency cut-off means that the resonant frequency cannot be modelled for some FEL parameters. Although the simulations presented in this thesis show the expected behavior, if one wishes to solve for a more realistic FEL, absorbing or transparent boundary conditions may need to be employed.

Testing and implementing more appropriate linear solvers should allow more complex systems to be modelled. Currently the linear solver significantly limits the size of the field which can be modelled. The 3D SACSE runs presented in this thesis were at the limit of the solvers capability, and the system was relatively small compared to more typical FEL systems. The reason SuperLU_DIST inhibits the code so much is that it is desgned and optimized for non-symmetrical linear systems. As the stiffness matrix is symmetric, using a linear solver appropriate to this should enhance the performance from both a speed and memory standpoint significantly. Tests are currently underway to do this.

In a real undulator with variable polarization, it is the phase between the x and y fields which are varied to produce the desired polarization. The model here could concievably be altered to reflect this, rather than the current method of varying the magnitudes of the magnetic undulator field in x and y. The constant focusing channel could also be changed to include focusing quadrupoles. As mentioned earlier, this could be achieved by altering the undulator-lattice/phase shifting section of the code. In fact, after a set number of undulator periods the

electron beam may have any coordinate transform applied to it. In practise, it should be relatively easy to do this.

Another pressing issue is the post-processing routines. An interface was designed in MATLAB for presentation of the results in [41], but this reads all the data files at once and consumes a large amount of memory. Indeed, the final, full 3D runs could not be analysed using this interface. A separate, lighter MATLAB script was written to generate this output.

Even this lighter script, however, was only just able to process the information due to memory constraints in the desktop machine used. In the future it will be necessary to employ a solution which processes the data files "on site," meaning the same multi-processor machines used to run the code will be needed to perform the post-processing, simply because the data files are too big for a standard desktop to read into memory. This will also enable the post-processing to be more immediate: currently the data files must be transferred to a local desktop, which takes a large amount of time over the internet, considering the files for just a few steps are several 10's of gigabytes in size (and these are relatively small undulators and electron pulses).

There are tentative plans that the code, when ready, should be released via the web under an open source licence.

There are also the numerous situations the code could be used to explore. The mode-locked FEL has already been mentioned, as has the investigation of lasing using very short electron pulses. The investigations begun in [56] could be expanded upon, as the radiation pulse does not appear to saturate. In reality, radiation growth may be inhibited by diffraction effects, and this code may be used to research this.

The broadband nature of the code opens the possibility of seeding the FEL interaction with lower than resonant frequencies, either to amplify the radiation, or perhaps, to help accelerate an electron pulse in the vein of an Inverse Free Electron Laser [63].

Different forms of the work in this thesis were presented at the international FEL conferences in 2009 and 2010. The FEL2009 conference paper is in appendix

A, and the two papers presented at FEL2010 are attached in appendices B and C. Posters were also presented for the three conference papers. A paper to be submitted to a peer reviewed journal is currently in preparation.

In general, a new, flexible FEL simulation tool has been developed that will allow many previously unexplored types of FEL interaction to be researched.

Bibliography

[1] J.M.J. Madey, 1971. Stimulated Emission of Bremsstrahlung in a Periodic Magnetic Field, *J. Appl. Phys.* **42**, 1906-1931.

[2] J.A. Clarke, 2004. *The Science and Technology of Undulators and Wigglers*, (Oxford University Press).

[3] F.R. Elder *et al*, 1971. Radiation from Electrons in a Synchrotron, *Phys. Rev.* **71** 829-830.

[4] A.L. Robinson, 2009. X-ray Data Booklet, Section 2.2 *History of Synchrotron Radiation*, Center for X-ray Optics and Advanced Light Source, Lawrence Berkeley National Laboratory.

[5] H. Motz, 1951. Application of the Radiation From Fast Electron Beams, *J. Appl. Phys.* **22**, 527-535.

[6] H. Motz, W. Thon, and R.N. Whitehurst, 1953. Experiments on Radiation By Fast Electron Beams, *J. Appl. Phys.* **24**, 826-833.

[7] L.R. Elias, W.M. Fairbank, J.M.J. Madey, H.A. Schwettman, and T.I. Smith, 1976. Observation of Stimulated Emission of Radiation by Relativistic Electrons in a Spatially Periodic Transverse Magnetic Field, *Phys. Rev. Lett.* **36**, 717-720.

[8] D.A.G. Deacon *et al.*, 1977. First Operation of a Free Electron Laser, *Phys. Rev. Lett.* **38**, 892-894.

[9] N.M. Kroll and W.A. McMullin, 1978. Stimulated Emission from Relativistic Electrons Passing Through a Spatially Periodic Magnetic Field, *Phys. Rev. A* **17**, 300-308.

[10] I.B. Bernstein and J.L. Hirschfeld, 1979. Amplification on a Relativistic Electron Beam in a Spatially Periodic Transverse Magnetic Field, *Phys. Rev. A* **20**, 1661-1670.

[11] P. Sprangle and R.A. Smith, 1980. Theory of Free Electron Lasers, *Phys. Rev. A* **21**, 293-301.

[12] A.M Kondratenko and E.L. Saldin, 1980. Generation of Coherent Radiation by a Relativistic Electron Beam in an Ondulator *Part. Accel.*, **10** 207-216.

[13] W.B. Colson, 1981. The Nonlinear Wave Equation for Higher Harmonics in Free-Electron Lasers, *IEEE J. Quant. Electron.* **QE-17**, 1417-1427.

[14] R. Bonifacio, F. Casagrande, and G. Casati, 1982. Cooperative and Chaotic Transition of a Free Electron Laser Hamiltonian Model, *Opt. Comm.* **40**, 219-223.

[15] T. Shintake *et al*, 2010. Status Report on Japanese XFEL Construction Project at SPring-8 *Proceedings of the 1st International Particle Accelerator Conference* 1285-1289.

[16] P. Emma *et al*, 2010. First Lasing and Operation of an Angstrom-Wavelength Free Electron Laser, *Nature Photon.* **4** 641-647.

[17] M. Altarelli *et al* (eds), 2007. The European X-Ray Free-Electron Laser Technical Design Report, DESY 2006-097.

[18] B.D. Patterson *et al*, 2007. Coherent Science at the Swiss FEL X-Ray Laser, *New Journ. Phys.* **12** 035012 (2010).

[19] J. Marangos *et al*, 2010. *NLS conceptual design report*, found at http://www.newlightsource.org/index.htm.

[20] W.M. Fawley, 2006. An Enhanced GINGER Simulation Code With Harmonic Emission and HDF5 Capabilities, *Proceedings of FEL 2006, BESSY, Berlin, Germany*, 218-221.

[21] S. Reiche, 1999. GENESIS: A Fully 3D Time-Dependant FEL Simulation Code, *Nucl. Instr. and Meth. in Phys. Res. A* **429** 243-248.

[22] E.L. Saldin *et al*, 1999. FAST: A Three-Dimensional Time-Dependant FEL Simulation Code *Nucl. Instr. and Meth. in Phys. Res. A* **429** 233-237.

[23] A.E. Siegman, 1986. *Lasers*, University Science Books, Sausalito.

[24] R. Bonifacio, R.M. Caloi, and C. Maroli, 1993. The Slowly Varying Envelope Approximation Revisited, *Opt. Comm.* **101** 185-187.

[25] S. Reiche, 2010. FEL simulations: History, Status and Outlook, *Proceedings of FEL 2010, Malmo, Sweden*, MOOCI1.

[26] F.A. Hopf *et al*, 1976. Classical Theory of a Free-Electron Laser, *Phy. Rev. Lett.* **37**, 1215-1218.

[27] R. Bonifacio and F. Casagrande *et al*, 1990. Physics of the High Gain FEL and Superradiance, *Rivista Del Nuovo Cimento* Vol **13** N 9.

[28] R. Bonifacio, C. Pellegrini, and L.M. Narducci, 1984. Collective Instabilities And High-Gain Regime in a Free Electron Laser, *Opt. Comm.*, **50** 373.

[29] N.M. Kroll, L.P. Morton, and M.N. Rosenbluth, 1981. Free-Electron Lasers with Variable Parameter Wigglers, *IEEE J. Quant. Electr.* QE-**17** 1436-1468.

[30] R. Bonifacio, B.W.J. McNeil, and P. Pierini, 1989. Superradiance in the High Gain Free-Electron Laser *Phys. Rev. A* **40**, 4467-4475.

[31] R. Bonifacio, L. de Salvo, P. Pierini, N. Piovella, and C. Pellegrini, 1994. Spectrum, Temporal Structure, and Fluctations in a Free Electron Laser Starting from Noise *Phys. Rev. Lett.* **73** 70-73.

[32] Z. Huang and K.J. Kim, 2007. Review of X-Ray Free-Electron Laser Theory, *Phys. Rev. ST Acc Beams* **10** 34801-34825.

[33] R. Bonifacio, L. De Salvo Souza, and B.W.J. McNeil, 1992. Emittance Limitations in the Free Electron Laser, *Optics Comm* **93**, 179-185.

[34] G. Lambert *et al*, 2009. Injection of Harmonics Generated in Gas in a Free-Electron Laser Providing Intense and Coherent X-Ray Light *Nature Phys.* **4** 296-300.

[35] G. Stupakov, 2009. Using the Beam-Echo Effect for Generation of Short-Wavelength Radiation *Phys. Rev. Lett.* **102** 074801.

[36] N.R. Thomson and B.W.J. McNeil, 2008. Mode locking in a free-electron laser amplifier, *Phys. Rev. Lett.* **100** 203901.

[37] F. Gruner *et al*, 2007. Design Considerations for Table-Top, Laser-Based VUV and X-Ray Free Electron Lasers, *Appl. Phys. B* **86** 431-435.

[38] N. Piovella, 1999. High gain free electron laser amplifiers starting from coherent and incoherent spontaneous emission, *Physics of Plasmas* **6** 3358.

[39] C. Maroli, V. Petrillo, and M. Ferrario, 2011. One-Dimensional Free-Electron Laser Equations Without The Sowly Varying Envelope Approximation, *Phys. Rev. ST Accel. Beams* **14**, 70703-70710.

[40] B.W.J. McNeil, G.R.M. Robb, and D.A. Jaroszynski, 1999. Self-amplification of coherent spontaneous emission in the free electron laser, *Opt. Comm.* **165**, 65-70.

[41] C.K.W. Nam, 2009. On the Theory and Modelling of the Fourth Generation Light Source, Ph.D. Thesis, University of Strathclyde.

[42] E.T. Scharlemann, 1989. in *High Gain, High Power FEL's* (edited by R. Bonifacio *et al*).

[43] R. Bonifacio and R. Corsini *et al*, 1993. New Effects in the Physics of High Gain Free-Electron Lasers; A Proposed Experiment and Possible Applications, *Rivista Del Nuovo Cimento* Vol **15** N 11.

[44] R.H. Hardin and F.D. Tappert, 1973. Applications of the split-step Fourier method to the numerical solution of nonlinear and variable coefficient wave equations, *SIAM Review*, **15**, 423.

[45] B.W.J. McNeil, M.W. Poole, and G.R.M. Robb, 2003. Unified model of electron beam shot noise and coherent spontaneous emission in the helical wiggler free electron laser, *Phys. Rev. ST - Acc. Beams* **6**, 070701.

[46] L.T. Campbell, R. Martin, and B.W.J. McNeil, 2009. A Fully 3D Unaveraged, Non-localised Electron, Parallelized Computational Model of the FEL, *Proceedings of FEL 2009, Liverpool, UK.*

[47] P.S. Pacheco. *Parallel Programming with MPI.* Morgan Kaufmann Publishers, Inc., 1997.

[48] X.S. Li and J.W. Demmel, 2003. SuperLU_DIST: A Scalable Distributed-Memory Sparse Direct Solver for Unsymmetric Linear Systems, *ACM Trans. Mathematical Software*,**29**, 2.

[49] L. Grigori, J. W. Demmel, and X.S. Li, 2007. Parallel Symbolic Factorization for Sparse LU with Static Pivoting, *SIAM J. Scientific Computing*, **29** 3.

[50] M. Frigo and S.G. Johnson, 2003. *FFTW 2.1.5 Manual*, available from http://www.fftw.org.

[51] X.S. Li, J. W. Demmel, J.R Gilbert, L. Grigori, and M. Shao, 1999. *SuperLU User's Guide*, available from crd.lbl.gov/x̃iaoye/SuperLU/.

[52] M. Joshi, G. Karypis, V. Kumar, A. Gupta, and F. Gustavson, 1999. PSPASES: Building a High Performance Scalable Parallel Direct Solver for Sparse Linear Systems, found at *http://www-users.cs.umn.edu/ mjoshi/pspases/.*

[53] MUMPS home page found at *http://graal.ens-lyon.fr/MUMPS/*.

[54] DSCPACK home page found at *http://www.cse.psu.edu/ raghavan/software.html*.

[55] B. Engquist and A. Majda, 1977. Absorbing Boundary Conditions for the Numerical Simulation of Waves, *Mathematics of Computation* **31** 629-651.

[56] B.W.J. McNeil, G.R.M. Robb, and M.W. Poole, 2003. An Improved 1D Model For Ultra High Power Radiation Pulse Propagation In The Helical Wiggler Free Electron Laser, *Proceedings of the 2003 Particle Accelerator Conference*.

[57] M. Borland, 1995. A Self-Describing File Protocol for Simulation Integration and Shared Postprocessors, in *Proceedings of the 1995 Particle Accelerator Conference, May 1-5, 1995, Dallas, Texas*.

[58] B.W.J. McNeil and G.R.M. Robb, 2002. Self-amplified coherent spontaneous emission in the planar wiggler free-electron laser, *Phys. Rev. E* **65**, 046503.

[59] E. Hecht and A. Zajac, 1974. *Optics*, (Addison-Wesley Publishing Company).

[60] B.W.J. McNeil, 2010. *Private Communication*.

[61] W.H. Press B.P. Flannery S.A. Teukolsky and W.T. Vetterling. *Numerical Recipes in Pascal*. Cambridge University Press, 1989.

[62] B.W.J. McNeil, 2011. *Private Communication*.

[63] E.D. Courant, C. Pellegrini, and W. Zakowicz, 1985. High-Energy Inverse Free-Electron-Laser Accelerator, *Phys. Rev. A* Vol **32** 2813-2823.

Appendix A

FEL2009 Paper

A FULLY 3D UNAVERAGED NON-LOCALISED ELECTRON, PARALLELIZED-COMPUTATIONAL MODEL OF THE FEL

L.T. Campbell, R. Martin and B.W.J. M^{c}Neil
SUPA, Department of Physics, University of Strathclyde, Glasgow, UK

Abstract

A new unaveraged 3D parallelized numerical model has been developed that will allow investigation of previously unexplored FEL physics. Unaveraged models are required to describe such effects as amplification of Coherent Spontaneous Emission and non-localised electron dynamics (see e.g. [1] and refs therein). A previous parallelized 3D model [2] was based upon a mixed finite element/Fourier method, however, there were some limitations in the parallel algorithm and numerical routines. These limitations are removed in the new model presented here by using only transforms in Fourier space enabling more effective data organization across multiple parallel processors and therefore allowing larger, more complex FEL systems to be studied. Furthermore, unlike the previous 3D model, which uses commercial numerical packages, the new simulation code uses only open-source routines.

INTRODUCTION

As FEL's continue to push boundaries of radiation wavelength and pulse lengths, and with more complex FEL schemes to achieve these being explored, it may become necessary to extend the scope of what numerical FEL codes can model. Most current codes average the equations governing the FEL interaction over a radiation period and confine electrons to a localised region within one radiation period of their initial conditions (in the electron beam rest frame.) To describe the FEL interaction at the sub-radiation period scale, and to model electron migration over distances greater than the radiation period (non-localised), a numerical code that models the unaveraged equations governing the FEL interaction is required.

A 1D non-averaged model describing both sub-period phenomena and non-localised electron propagation has previously been developed [1, 3, 4]. More recently a 3D parallel non-averaged model for a helical undulator was developed in [2]. A substantially modified version of this 3D model, with significantly better parallel performance, is presented in this paper.

The 3D FEL model of [2] uses a split-step Fourier method [5]. This method separates a single numerical integration step, of the governing differential equations along the undulator, into two separate half-steps. In the first half step a Fourier transform method is used to solve for the field diffracting in the absence of any electron source terms. In the second half-step a Finite Element Galerkin Method [6] is used to solve for the field being driven by the electron sources, and in the absence of diffraction, while a 4th order Runge-Kutta method simultaneously drives the electrons. When parallelized using MPI, the model requires communication between three separate data sets distributed over multiple processors with each integration step of the code. The amount of communication between processors should be kept to a minimum if the run-time of a parallel code is to scale well with the number of processors used, otherwise the run-time benefit of using multiple processors can become significantly reduced [7].

The model presented here replaces the FEGM of the above model with a Fourier method (using open-source FFT routines [8]) similar to that described in [9]. The field is therefore now solved entirely in a 3D Fourier space. The method allows a reduction in communication between processors and gives a better scaling of the run-time benefit with increasing processor number. Furthermore, the commercial routines used for the FEGM are not needed, improving portability and allowing an open-source code when released.

The model is also generalised to allow any undulator polarisation from planar to helical, variable along the FEL interaction.

THEORETICAL MODEL

Starting from the 3D Maxwell wave equation and the Lorentz force equation, the 3D FEL equations for an helical undulator in the scaled dimensionless form of [2] may be written:

$$-i\rho\left(\frac{\partial^2 A}{\partial\bar{x}^2}+\frac{\partial^2 A}{\partial\bar{y}^2}\right)+\frac{\partial A}{\partial\bar{z}}+2i\rho\frac{\partial^2 A}{\partial\bar{z}\partial\bar{z}_2}=\frac{\gamma}{a_w\bar{n}_p}\times$$
$$\frac{\partial}{\partial\bar{z}_2}\sum_{j=1}^{N}\bar{p}_{\perp j}e^{i\bar{z}_2/2\rho}\sqrt{\frac{\epsilon Q_j(\epsilon Q_j+2)}{(1+|\bar{p}_{\perp j}|^2)}}\,\delta^3(\bar{x}_j,\bar{y}_j,\bar{z}_{2j}) \quad (1)$$

$$\frac{d\bar{p}_{\perp j}}{d\bar{z}}=\frac{a_w}{2\rho}\left[ie^{-\frac{i\bar{z}}{2\rho}}-\left(\frac{2\gamma_r\rho}{a_w}\right)^2\epsilon Q_j A e^{-\frac{i\bar{z}_{2j}}{2\rho}}\right]-$$
$$\frac{a_w^2\epsilon}{8\rho^2}\sqrt{\frac{Q_j(2+\epsilon Q_j)}{(1+|\bar{p}_{\perp j}|^2)}}\frac{(\bar{x}_j-i\bar{y}_j)}{(1+\epsilon Q_j)^2} \quad (2)$$

$$\frac{dQ_j}{d\bar{z}}=\frac{a_w}{4\rho}\frac{Q_j(\epsilon Q_j+2)}{1+|\bar{p}_{\perp j}|^2}\left[i(\epsilon Q_j+1)(\bar{p}^*_{\perp j}e^{-i\frac{\bar{z}}{2\rho}}-c.c.)+\right.$$
$$\left.\left(\frac{2\gamma_r\rho}{a_w}\right)^2\epsilon Q_j(\bar{p}^*_{\perp j}Ae^{-i\frac{\bar{z}_{2j}}{2\rho}}+c.c.)\right] \quad (3)$$

$$\frac{d\bar{z}_{2j}}{d\bar{z}}=Q_j \quad (4)$$

$$\frac{d\bar{x}_j}{d\bar{z}} = \sqrt{\frac{Q_j(\epsilon Q_j+2)}{1+|\bar{p}_{\perp j}|^2}}\mathrm{Re}(\bar{p}_{\perp j}) \quad (5)$$

$$\frac{d\bar{y}_j}{d\bar{z}} = -\sqrt{\frac{Q_j(\epsilon Q_j+2)}{1+|\bar{p}_{\perp j}|^2}}\mathrm{Im}(\bar{p}_{\perp j}) \quad (6)$$

where $\delta^3(\bar{x}_j,\bar{y}_j,\bar{z}_{2j}) \equiv \delta(\bar{x}-\bar{x}_j)\delta(\bar{y}-\bar{y}_j)\delta(\bar{z}_2-\bar{z}_{2j})$ and all variables are as defined in [2]. The only approximations made are the neglect of space charge, the paraxial approximation, and

$$\left|\frac{\partial E_\perp}{\partial \bar{z}}\right| << \left|\frac{\bar{\beta}_z}{1-\bar{\beta}_z}\frac{\partial E_\perp}{\partial \bar{z}_2}\right|,$$

where $E_\perp = \xi_0 e^{-i\frac{\bar{z}_2}{2\rho}}$ and $\xi_0(\bar{z},\bar{z}_2)$ is the complex radiation envelope. The latter approximation is made in [10] where, expressed in the independent variables $(\bar{z},\bar{z}_1)$, it is shown to be equivalent to the neglect of any backward propagating field. Focussing of the electron beam is described by the final term of (2) corresponding to the 'natural focussing' of an helical wiggler. This term is easily modified for other focussing systems.

The field equation (1) is solved using the Fourier split-step method by seperating it into diffraction-only and source-only parts. For diffraction only in the absence of sources the field equation is

$$-i\rho\left(\frac{\partial^2 A}{\partial \bar{x}^2}+\frac{\partial^2 A}{\partial \bar{y}^2}\right)+\frac{\partial A}{\partial \bar{z}}+2i\rho\frac{\partial^2 A}{\partial \bar{z}\partial \bar{z}_2}=0 \quad (7)$$

Defining the 3D Fourier transform

$$\tilde{A}(k_{\bar{x}},k_{\bar{y}},k_{\bar{z}_2},\bar{z}) = FT\{A(\bar{x},\bar{y},\bar{z}_2,\bar{z}\} \quad (8)$$

and applying to (7) yields the solution

$$\tilde{A}(\bar{z}_0+\Delta\bar{z}) = \tilde{A}(\bar{z}_0)\exp\left(\frac{-i\rho(k_{\bar{x}}^2+k_{\bar{y}}^2)}{1-2\rho k_{\bar{z}_2}}\Delta\bar{z}\right) \quad (9)$$

for an arbitrary initial $\bar{z}_0$ and where the dependence of $\tilde{A}$ on $(k_{\bar{x}},k_{\bar{y}},k_{\bar{z}_2})$ is understood.

In the absence of diffraction, but with electron source terms, the field equation becomes

$$\frac{\partial A}{\partial \bar{z}} = \frac{\gamma_r}{a_w\bar{n}_p}\sum_{j=1}^{N}\bar{p}_{\perp j}e^{i\bar{z}_2/2\rho}\sqrt{\frac{\epsilon Q_j(\epsilon Q_j+2)}{1+|\bar{p}_{\perp j}|^2}}\delta^3(\bar{x}_j,\bar{y}_j,\bar{z}_{2j}). \quad (10)$$

In the previous code of [2], the field equation (10) was solved simultaneously with the electron equations using a 4th order Runge-Kutta and FEGM. One integration step required 3 different sets of field data distributed across the parallel processors: one for the Fourier transforms used in the diffraction step, one for the finite element, and one for the RHS of the source equation (10) plus the electron equations. The optimum form of the electron data distribution also changes as they migrate across field elements.

The alternative solution presented here utilises a Fourier description of the field source term, similar to the multi-frequency FEL model of [9], so that the entire field equation may be solved in Fourier space. Fourier transforming (10) using (8) gives

$$\frac{\partial \tilde{A}}{\partial \bar{z}} = \frac{\gamma_r}{a_w\bar{n}_p}\sum_{j=1}^{N}\bar{p}_{\perp j}\sqrt{\frac{\epsilon Q_j(\epsilon Q_j+2)}{1+|\bar{p}_{\perp j}|^2}}\times \exp\left[-i(k_{\bar{x}}\bar{x}_j+k_{\bar{y}}\bar{y}_j+\bar{z}_{2j}(k_{\bar{z}_2}-\frac{1}{2\rho}))\right] \quad (11)$$

Equation (11) describes how the electrons drive the field in 3D Fourier space and is relatively simple to solve numerically. To obtain the field in real space, required for the electron dynamic equations of (2...6), the inverse transform is all that is required and a finite element description of the field in real space is unnecessary.

VARIABLE UNDULATOR POLARISATION

The general form of the radiation field definition and the equation describing its evolution allows any field polarisation to be modelled. A relatively simple modification to the undulator field then allows modelling of an elliptically polarised FEL. The transverse terms of the magnetic wiggler field are re-defined as:

$$\mathbf{B_w} = \frac{B_w}{\sqrt{2}}(\mathbf{f}e^{-i\frac{\bar{z}}{2\rho}}+c.c.), \quad (12)$$

where the new basis vector $\mathbf{f} = (H\hat{\mathbf{x}}+i\hat{\mathbf{y}})/\sqrt{2}$ and the constant H has limits $0 \le H \le 1$, where $H=1$ corresponds to an helical undulator and $H=0$ for a planar undulator. For simplicity here, the axial terms of the wiggler field that give the natural focussing remain unchanged from [2]. Note that $\mathbf{f}$ is not a unit vector and the scaling of the equations is with respect to the y-component of the undulator magnetic field. The scaling factor H appears explicitly in the equation of motion for $\bar{p}_{\perp j}$ only:

$$\frac{d\bar{p}_{\perp j}}{d\bar{z}} = \frac{a_w}{2\rho}\left[\frac{i}{2}\left((1+H)e^{-\frac{i\bar{z}}{2\rho}}-(1-H)e^{\frac{i\bar{z}}{2\rho}}\right)-\left(\frac{2\gamma_r\rho}{a_w}\right)^2\epsilon Q_j A e^{-\frac{i\bar{z}_{2j}}{2\rho}}\right]- \frac{a_w^2\epsilon}{8\rho^2}\sqrt{\frac{Q_j(2+\epsilon Q_j)}{(1+|\bar{p}_{\perp j}|^2)}}\frac{(\bar{x}_j-i\bar{y}_j)}{(1+\epsilon Q_j)^2} \quad (13)$$

with all other equations in (1...6) remaining unchanged. Note that this form allows the undulator polarisation factor to vary as a function along its length $H(\bar{z})$.

NUMERICAL MODEL

The summation over real electrons is changed to a summation over macro-particles using the method of [1]. The localised electron density over a volume element $\bar{V}_k$ in the

scaled space $(\bar{x}, \bar{y}, \bar{z}_2)$ containing N_k electrons may be described as a by a fractional weighting factor $0 < \chi_k \leq 1$ of the scaled peak electron density in the pulse:

$$\frac{N_k}{\bar{V}_k} = \chi_k \bar{n}_p. \quad (14)$$

Using (14), the sum over N real electrons, appearing in the source term of (11), changes to a sum over $k = 1 \ldots N_m$ macroparticles each of electron charge weight N_k as follows:

$$\frac{1}{\bar{n}_p}\sum_{j=1}^{N}(\cdots)_j = \frac{1}{\bar{n}_p}\sum_{k=1}^{N_m} N_k(\cdots)_k = \sum_{k=1}^{N_m}\chi_k\bar{V}_k(\cdots)_k \quad (15)$$

Defining the normalized weighting $\bar{\chi}_k = \chi_k \bar{V}_k$, the final form of the Fourier field equation (11) implemented in the code is obtained:

$$\frac{\partial\tilde{A}}{\partial\bar{z}} = \frac{\gamma_r}{a_w}\sum_{k=1}^{N_m}\bar{\chi}_k\bar{p}_{\perp k}\sqrt{\frac{\epsilon Q_k(\epsilon Q_k+2)}{1+|\bar{p}_{\perp k}|^2}}\times \exp\left[-i(k_{\bar{x}}\bar{x}_k + k_{\bar{y}}\bar{y}_k + \bar{z}_{2k}(k_{\bar{z}_2} - \frac{1}{2\rho}))\right]. \quad (16)$$

The Fourier field is discretized into nodes along each axis $(\bar{x}, \bar{y}, \bar{z}_2)$ and wavevector k-values take the general form $k = 2\pi n/l$, where the integer $-M/2 \leq n \leq M/2$ and M is the number of nodes spanning length l along the axis. The numerical fast-Fourier transforms are taken using the parallel processor FFTW open-source package [8]. The macroparticles and fourier field nodes are initially distributed uniformly among the parallel processors with increasing $\bar{z}_2$.

The new split-step Fourier method consists of the following steps:

1. Field Diffraction Step: The Fourier field diffraction equation (9) is solved. Data redistribution of the transformed field is not required.

2. Field Driving and Electron Propagation Step: The Fourier field source equation (16) is solved and the macroparticle equations (2-6) are propogated using a 4th order Runge-Kutta method. Some macroparticle data needs to be communicated between processors to act as the source for all the Fourier field nodes of (16). After the macroparticles drive the field in Fourier space a backwards Fourier transform is required to calculate the real field for the macroparticle equations (2-6). The macroparticle equations are solved in parallel without need for communication of field data between processors.

3. The latter two steps are repeated until the end of the integration.

A summary of the differences between the previous FEGM algorithm of [2] and the new method presented here is shown in Fig. 1.

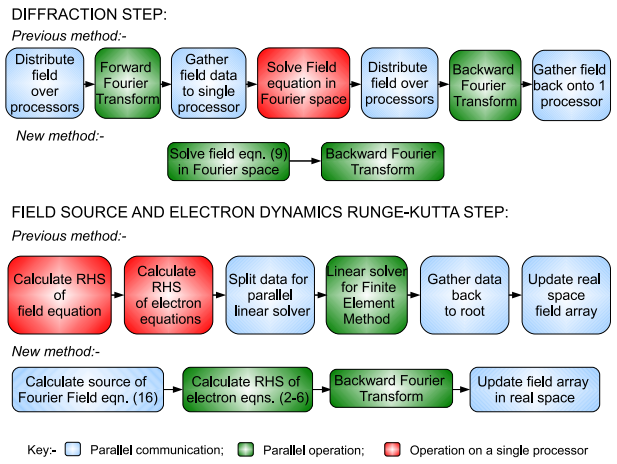

Figure 1: A schematic of the parallel algorithms showing the differences between the previous Finite Element Galerkin Method of [2] with the Fourier method presented here.

PLANE WAVE APPROXIMATION

The field description can be altered to approximate a plane wave by using only one node in the tranverse plane. Only the constant, non-oscilatory term of the numerical Fourier series then exists i.e. $k_{\bar{x}}, k_{\bar{y}} = 0$ and the field is then only a function of $\bar{z}_2$. Note, however, that this plane wave representation of the field still allows full 3D electron dynamic effects such as emittance and beam focussing to be modelled correctly. For a 'full' 1D limit, only one macroparticle, and so one value of the transverse variables, is used for each position in $\bar{z}_2$. The model is therefore quite flexible enabling a range of effects to be modelled, from a relatively fast full 1D model, to the plane wave approximation while retaining complete 3D electron dynamics, to the complete 3D model for both radiation field and electron dynamics.

To make the plane wave approximation in the numerical model the real-space field equation (10) is first integrated over the transverse plane ($\bar{x}$,$\bar{y}$). The equation is then Fourier transformed to give:

$$\frac{\partial\tilde{A}}{\partial\bar{z}} = \frac{\gamma_r}{a_w}\sum_{k=1}^{N_m}\bar{\chi}_k^{(1D)}\bar{p}_{\perp k}\sqrt{\frac{\epsilon Q_k(\epsilon Q_k+2)}{1+|\bar{p}_{\perp k}|^2}}\times \exp(-i\bar{z}_{2k}(k_{\bar{z}_2} - \frac{1}{2\rho})) \quad (17)$$

where $\bar{\chi}_k^{(1D)} = \chi_k l_k$ and l_k is the range of $\bar{z}_2$ initially occupied by the kth macroparticle. Simulations using the code in the full 1D limit give very good agreement with results from [1] and [3].

EXAMPLE

A simple example is used to demonstrate first simulation results using the code. Several high gain FEL schemes operating at short wavelengths propose to use the exhaust

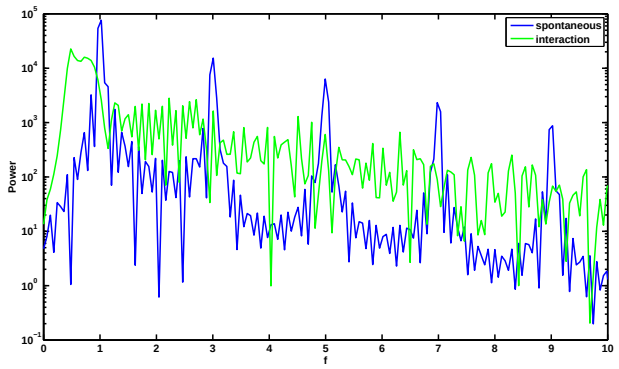

Figure 2: Spectra in the 1D planar wiggler limit for a short electron pulse generating CSR both with (green) and without (blue) coupling to the radiation field.

electron bunches to generate long wavelength radiation via Coherent Spontaneous Radiation, where the electron bunch length is less than the resonant wavelength of a long period undulator. While averaged FEL codes cannot model this interaction the non-averaged code described here can. Parameters similar to that of the UK NLS proposal [11] are used which in the scaling here are: $\rho \approx 0.24; a_w \approx 60$ and with a gaussian electron pulse $\sigma \approx 1/50$th that of a resonant radiation wavelength of $\lambda \approx 100\mu$m. The code simulated a planar undulator with $H = 0$ and operating in the 1D mode over 10 undulator periods (without any waveguide) of $\lambda_w = 1$m generates the spectra of Fig. 2 both with and without electron coupling to the radiation field. It can be seen that with electron coupling (green), the electron energy loss to the field shifts the resonant wavelength to longer wavelengths and significantly changes the spectrum from that of the uncoupled case (blue) which shows the usual CSR wiggler spectrum with odd harmonics clearly visible.

Using the same parameters, the second simulation demonstrates the code operating in 3D again with a planar wiggler. The scaled field polarisation is plotted in the $(\bar{x}, \bar{y})$ plane in Fig. 3 as a vector field. This polarisation does not change as a function of $\bar{z}_2$ so that it describes linearly polarised radiation and demonstrates the ability of the code to model variable polarisations.

CONCLUSION

A parallel FEL simulation code able to model sub-radiation wavelength effects and non-localised electron dynamics has been developed. This code algorithm significantly reduces run-time from the previous version of [2]. More rigorous testing and benchmarking of the code will be undertaken before release.

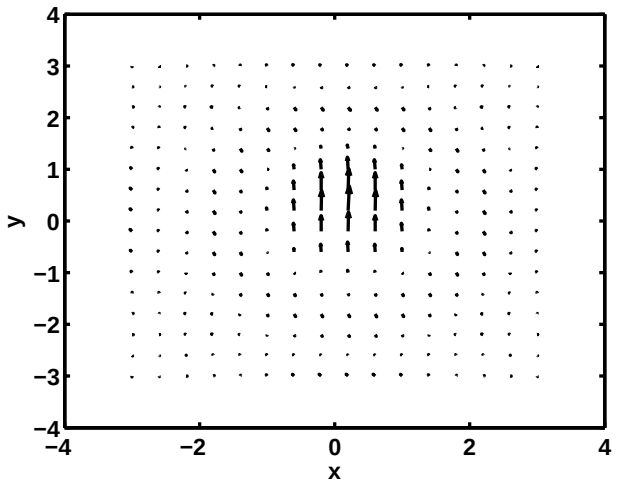

Figure 3: Scaled electric field vector plot using the code in the 3D planar wiggler limit to demonstrate generation of lineraly polarised radiation from a planar wiggler.

REFERENCES

[1] B.W.J. McNeil, M.W. Poole and G.R.M. Robb, Phys. Rev. ST Accel. Beams **6**, 070701 (2003); B. W. J. McNeil, G. R. M. Robb and M. W. Poole, MPPB060, Proceedings of the 2003 Particle Accelerator Conference, Portland, Oregon, USA (2003)

[2] C.K.W. Nam, P. Aitken and B.W.J. McNeil, MOPPH025, Proceedings of the 30th International FEL Conference, Gyeongju, Korea (2008); C.K.W. Nam, *On the Theory and Modelling of the Fourth Generation Light Source*, Ph.D. Thesis, University of Strathclyde (2009)

[3] B.W.J. McNeil, G.R.M. Robb and D.A. Jaroszynski, Opt. Commun. **165**, 65 (1999)

[4] B.W.J. McNeil, G.R.M. Robb and D.A. Jaroszynski, Nucl. Instrum. Methods Phys. Res., Sect. A **445**, 72 (2000)

[5] R.H. Hardin and F.D. Tappert, SIAM Review **15**, 423 (1973)

[6] K.H. Huebner E.A. Thornton and T.G. Byrom, *The Finite Element Method For Engineers*, Wiley (1995)

[7] P.S. Pacheco, *Parallel Programming with MPI*, Morgan Kaufmann Publishers, Inc. (1997)

[8] M. Frigo and S.G. Johnson, *FFTW 2.1.5 Manual* (2003) available from `http://www.fftw.org/`

[9] N. Piovella, Physics of Plasmas **6**, 3358 (1999)

[10] B.W.J. McNeil and G.R.M. Robb, Phys. Rev. E **65**, 046503 (2002)

[11] New Light Source (NLS) Project: Science Case and Outline Facility Design, Eds. J. Marangos, R. Walker and G. Diakun (2009) available from `http://www.newlightsource.org/`

Appendix B

FEL2010 Paper 1

AN UNAVERAGED COMPUTATIONAL MODEL OF A VARIABLY POLARIZED UNDULATOR FEL

L.T. Campbell and B.W.J. M^{c}Neil
SUPA, Department of Physics, University of Strathclyde, Glasgow, UK

Abstract

An unaveraged 3D model of the FEL has been developed which can model variably polarised undulators. The radiation field polarisation is self-consistently driven by the electron dynamics and is completely variable. This paper describes both physical model and computational code.

INTRODUCTION

Future FEL's may need to utilize effects which occur on the scale of a resonant radiation wavelength or smaller, timescales which are beyond the resolution of averaged FEL simulation codes. In order to investigate these effects and the facilities which will exploit them, 3D codes which solve unaveraged mathematical models of the FEL will be needed. The simulation codes of [1] and [2] are such codes. The disadvantage of a mathematical model with increased resolution is of course the much higher sampling rates needed to accurately model the system. To handle potentially very large data sizes such codes are best run in parallel on multiple processors.

In this paper the development of the unaveraged parallel computational model from [1] and [2] is reported. In [2], the variable H was added to describe the strength of the wiggler field in the x axis. This has been replaced by two new variables to control the strength of the wiggler field in both x and y enabling full variable wiggler polarization. The numerical method has been further refined to enhance its speed returning to the original Finite Element Method used in [1] while retaining the parallel memory distribution of [2]. The radiation field in x and y is now described fully including the 'fast' phase variations rather than via a complex envelope description. The code utilizes only open-source routines.

THE MODEL

An unnormalized vector basis:

$$\hat{\mathbf{f}} = f_x\hat{\mathbf{x}} + if_y\hat{\mathbf{y}} \tag{1}$$

is used to define a variable polarized undulator field

$$\mathbf{B}_w = \frac{B_w}{2}(\hat{\mathbf{f}}e^{-ik_w z} + c.c.) \tag{2}$$

where B_w is the peak magnetic field strength so that f_x and f_y describe the strength of the wiggler magnetic field in x and y. The vector basis $\hat{\mathbf{f}}$ is un-normalized so that the RMS magnetic field $\bar{B}_w$ varies from $B_w/\sqrt{2} \le \bar{B}_w \le B_w$ as the wiggler changes from planar to helical.

The electromagnetic field is defined as:

$$\mathbf{E}(x,y,z,t) = \frac{1}{\sqrt{2}}\left(\hat{\mathbf{e}}\xi_0 e^{i(kz-\omega t)} + \hat{\mathbf{e}}^*\xi_0^* e^{-i(kz-\omega t)}\right) \tag{3}$$

with complex envelope $\xi_0(x,y,z,t)$ and the normalized vector basis $\hat{\mathbf{e}} = \frac{1}{\sqrt{2}}(\hat{\mathbf{x}}+i\hat{\mathbf{y}})$ is defined with $\hat{\mathbf{e}}\cdot\hat{\mathbf{e}} = \hat{\mathbf{e}}^*\cdot\hat{\mathbf{e}}^* = 0$ and $\hat{\mathbf{e}}\cdot\hat{\mathbf{e}}^* = 1$.

The 3D FEL is described using the coupled Maxwell-Lorentz equations which in the Compton limit and with the paraxial approximation gives:

$$\nabla^2\mathbf{E} - \frac{1}{c^2}\frac{\partial^2\mathbf{E}}{\partial t^2} = -\frac{\mu_0 e}{m}\sum_{j=1}^{N}\frac{\mathbf{p}_j}{\gamma_j}\delta^3(x_j,y_j,z_j) \tag{4}$$

$$\mathbf{F} = -e(\mathbf{E} + \mathbf{v}\times\mathbf{B}),. \tag{5}$$

where $\delta^3(x_j,y_j,z_j) = \delta(x - x_j(t))\delta(y - y_j(t))\delta(z - z_j(t))$.

Projecting the wave equation (4) onto $\hat{\mathbf{e}}^*$ gives:

$$\left(\nabla^2 - \frac{1}{c^2}\frac{\partial^2}{\partial t^2}\right)E_\perp = -\frac{\mu_0 e}{m}\sum_{j=1}^{N}\frac{p_{\perp j}}{\gamma_j}\delta^3(x_j,y_j,z_j) \tag{6}$$

where $E_\perp = \xi_0 e^{i(kz-\omega t)} = E_x - iE_y$ is the transverse field. Similarly $p_{\perp j} = p_{xj} - ip_{yj}$ is the perpindicular momentum of the jth electron.

Defining the independent variables $\bar{z} = 2k_w\rho z$ and $\bar{z}_2 = 2k_w\rho\bar{\beta}_z(ct - z)/(1-\bar{\beta}_z)$, equation (6) becomes:

$$\nabla_\perp^2 E_\perp + (2k_w\rho)^2\left(\frac{\partial}{\partial\bar{z}}\left(\frac{\partial}{\partial\bar{z}} - \frac{2\bar{\beta}_z}{1-\beta_z}\frac{\partial}{\partial\bar{z}_2}\right)\right)E_\perp =$$

$$-\frac{e}{\epsilon_0 mc}4k_w^2\rho^2\left(\frac{\bar{\beta}_z}{1-\bar{\beta}_z}\right)^2\frac{\partial}{\partial\bar{z}_2}\sum_{j=1}^{N}\frac{p_{\perp j}}{\beta_{zj}\gamma_j}\delta^3(x_j,y_j,\bar{z}_{2j}) \tag{7}$$

and the independent variable of the parameters of the δ^3 Dirac delta function is now $\bar{z}$.

Assuming:

$$\left|\frac{\partial}{\partial\bar{z}}E_\perp\right| << \left|\frac{\bar{\beta}_z}{1-\beta_z}\frac{\partial}{\partial\bar{z}_2}E_\perp\right|, \tag{8}$$

which is equivalent to the neglect of the backwards

wave [3], then the wave equation (7) simplifies to:

$$\nabla_\perp^2 E_\perp - (2k_w\rho)^2 \frac{2\bar{\beta}_z}{1-\beta_z}\frac{\partial E_\perp}{\partial\bar{z}\partial\bar{z}_2} = -\frac{e}{\epsilon_0 mc}4k_w^2\rho^2\left(\frac{\bar{\beta}_z}{1-\bar{\beta}_z}\right)^2\frac{\partial}{\partial\bar{z}_2}\sum_{j=1}^{N}\frac{p_{\perp j}}{\beta_{zj}\gamma_j}\delta^3(x_j,y_j,\bar{z}_{2j}) \quad (9)$$

Projecting the Lorentz equation (5) onto $\hat{\mathbf{e}}^*$ and changing to the variables $(\bar{z},\bar{z}_2)$ the equation for the transverse momentum is obtained:

$$\frac{dp_{\perp j}}{d\bar{z}} = \frac{-e}{2k_w\rho c\beta_{zj}}\Big[\xi_0 e^{-i\frac{\bar{z}_{2j}}{2\rho}} - \frac{p_{zj}}{\gamma_j m}\left(\frac{\xi_0}{c}e^{-i\frac{\bar{z}_{2j}}{2\rho}} + iB_w G^*\right)\Big] \quad (10)$$

and the z component is:

$$\frac{dp_{zj}}{d\bar{z}} = \frac{-ep_{\perp j}}{4mck_w\rho\gamma_j\beta_{zj}}\left(\frac{\xi_0^*}{c}e^{i\frac{\bar{z}_{2j}}{2\rho}} - iB_w G\right) + c.c., \quad (11)$$

where $G = (f_x\cos(\bar{z}/2\rho) + if_y\sin(\bar{z}/2\rho))$ is a term describing electron 'jitter' motion in z resulting from propagation in a non-helical wiggler field. Using relation (11) with the equation for the electron energy:

$$\frac{dp_{zj}}{d\bar{z}} = mc\frac{d}{d\bar{z}}(\gamma_j\beta_{zj}),$$

along with equations (9), (10) and (11) and the scaling of [1], modified slightly so that:

$$\epsilon Q_j = \frac{1-\beta_{zj}}{\beta_{zj}}, \qquad \epsilon = \frac{1-\bar{\beta}_z}{\bar{\beta}_z},$$
$$\bar{x} = \frac{x}{\sqrt{l_g l_c}}, \qquad \bar{y} = \frac{y}{\sqrt{l_g l_c}},$$
$$\bar{p}_\perp = \frac{p_\perp}{mc}, \qquad A = \frac{e\sqrt{f_x^2+f_y^2}}{mc\omega_p\sqrt{2\gamma_r\rho}}$$

gives the final set of working equations which are solved numerically by the code:

$$-i\rho\left(\frac{\partial^2 A_\perp}{\partial\bar{x}^2} + \frac{\partial^2 A_\perp}{\partial\bar{y}^2}\right) + 2i\rho\frac{\partial^2 A_\perp}{\partial\bar{z}\partial\bar{z}_2} = \sqrt{\frac{f_x^2+f_y^2}{2}}\frac{\gamma_r}{\bar{a}_w\bar{n}_p}\frac{\partial}{\partial\bar{z}_2}\sum_{j=1}^{N}\frac{\bar{p}_{\perp j}}{(1+|\bar{p}_{\perp j}|^2)^{1/2}}\times (\epsilon Q_j(\epsilon Q_j+2))^{1/2}\delta^3(\bar{x}_j,\bar{y}_j,\bar{z}_{2j}) \quad (12)$$

$$\frac{d\bar{p}_{\perp j}}{d\bar{z}} = \frac{\bar{a}_w}{\rho\sqrt{2(f_x^2+f_y^2)}}\times \left(iG^* - \epsilon Q_j\left(\frac{2\gamma_r\rho}{\bar{a}_w}\right)^2 A_{\perp j}\right) + F_j \quad (13)$$

$$\frac{dQ_j}{d\bar{z}} = \frac{\bar{a}_w}{4\rho}\sqrt{\frac{2}{f_x^2+f_y^2}}\frac{Q_j(\epsilon Q_j+2)}{1+|\bar{p}_{\perp j}|^2}\times \Big(-i(\epsilon Q_j+1)(\bar{p}_{\perp j}G - \bar{p}_{\perp j}^* G^*) + \epsilon Q_j\left(\frac{2\gamma_r\rho}{\bar{a}_w}\right)^2(\bar{p}_\perp A_{\perp j}^* + \bar{p}_{\perp j}^* A_{\perp j})\Big) \quad (14)$$

$$\frac{d\bar{z}_{2j}}{d\bar{z}} = Q_j \quad (15)$$

$$\frac{d\bar{x}_j}{d\bar{z}} = \sqrt{\frac{Q_j(2+\epsilon Q_j)}{1+|\bar{p}_{\perp j}|^2}}\Re(\bar{p}_{\perp j}) \quad (16)$$

$$\frac{d\bar{y}_j}{d\bar{z}} = -\sqrt{\frac{Q_j(2+\epsilon Q_j)}{1+|\bar{p}_{\perp j}|^2}}\Im(\bar{p}_{\perp j}) \quad (17)$$

where the equations for the $\bar{x}$, $\bar{y}$ and $\bar{z}_2$ electron coordinates are simply derived from the scaled momentum/energy relations. The field term $A_\perp = A_x - iA_y$ is the scaled perpendicular field, related to the scaled complex envelope A by $A_\perp = Ae^{-i\frac{\bar{z}_2}{2\rho}}$. Hence the code now solves explicitly for the $\bar{x}$ and $\bar{y}$ radiation field components. This assists in resolving some numerical issues requiring many conversions between real and complex numbers when the electrons interact with a complex envelope A.

The term F_j describes a generic focussing channel of the electron transverse motion. This is similar to the natural focussing of the helical wiggler which for convenience may be varied independently of the actual undulator used via a scaling factor f. In the scaled notation used here the focussing force is given by:

$$F_j = -f\frac{\beta_{zj}\bar{a}_w^2\sqrt{\epsilon}}{8\gamma_j\rho^2}(\bar{x}_j - i\bar{y}_j). \quad (18)$$

COMPUTATIONAL SOLUTION

The code integrates the working equations by using a split step Fourier method [4], where the first half step solves field diffraction in the absence of the electron transverse current and the second step propogates the electrons and field equation in the absence of diffraction. Where previously the code solved the non-diffractive half-step in Fourier space, as outlined in [2], it is now solved using a Finite Element Method [5]. However, the beneficial memory and processing distribution across processors in the parallel algotithm of the previous Fourier method is retained.

The resolution of the model is not limited to the resonant radiation wavelength. The field must be sampled on the sub-wavelength scale to describe the resonant wave oscillations to the desired resolved frequency. Because of this, the data sizes for a full 3D field and 6D electron phase-space distribution can be large, hence the use of a parallel code algorithm to distribute the data and solve the equations.

The code of [2] used a fully distributed memory solution which solved both field source and diffraction in the Fourier domain. In terms of memory distribution this

works well, however the solution requires a prohibitive number of calculations per step. In order to drive the Fourier field each electron must interact with *every* field node, and the number of calcuations required is then proportional to the number of electrons $\times$ the number of Fourier nodes. In a full 3D system (and with electrons in 6 dimensions), this can give the order of 10^{14} interactions per quarter step using a standard Runge Kutte 4th order method for a moderately sized system, each of which is composed of many computational operations. The base number of calculations for a moderate simulation is prohibitively inefficient.

In replacing the Fourier method with the finite element method, however, each electron interacts with only its 8 surrounding nodes, so the number of calculations is proportional to the number of electrons $\times 8$. The base number of calculations is therefore significantly smaller and the code runs much more efficiently.

The main problem with a parallel algorithm for this finite element model is in the uniform distribution of the data. There are two different interaction systems, the electrons and the field, which are constantly shifting spatially in time with respect to each another due to the slippage of the field with respect to the electrons. Any given electron must have its local field stored on its processor for any given step. However, the local field shifts with each step. Furthermore, the rate at which the local field shifts is not a constant in an unaveraged system - the equations allow the electron to have a rapid change in energy within one radiation period e.g. for very high radiation fields.

One approach is to pick one of the systems, either the field or electrons, distribute it evenly and fix this distribution. The data distribution for the other system must be calulated at each step and will be shifted around the processors as appropriate. If the field is chosen as the fixed distribution, the electron variables will be shifted between processors. However, this leads to a poor spread of the computational load, as the electrons can only generate, amplify, and interact with the field finite elements which immediately surrounds them. This is especially true for short electron bunches, which is one of the areas an unaveraged code is particularly useful - the electrons in the bunch will only be distributed over a small percentage of the processors available at any one time. Those processors will be doing all the work to drive the field. Taking the opposite approach, by distributing the electron data uniformly across the processors, the computational load is well spread. However, the management of the field data between processors can become complicated by the need for the electrons on one processor to interact with potentially distant field nodes and the desire to uniformly distribute the field nodes across processors for the diffractive half-step.

In the compromise of the code presented here, the electrons are distributed evenly in memory *and* a full copy of the field is kept on each processor. This is justified by considering the relative memory sizes for a typical FEL system: each electron has 6 dimensions and the number

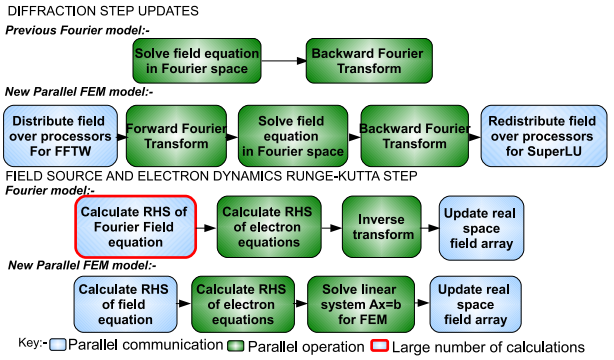

Figure 1: Illustration of the the differences in computational solution between [2] and the code used here.

of electrons can potentially be a few orders of magnitude larger than the number of field nodes; the field has only 3 dimensions. Clearly, the priority is to distribute the electrons in memory. However, recalculating the field distribution each step can add significant inter-processor communication time, which can hamper the ability of a parallel code for large processor numbers.

3D BEAM EFFECTS

The effects of the 3D electron beam are illustrated with a simple example. The beam is said to be matched when its radius is matched to the undulator focussing channel which may be calculated from the normalised emittance relation $\gamma\epsilon_x = \gamma\epsilon_y = \epsilon_n = \gamma r_b^2/\beta$ [6], and in terms of the scaled notation and putting in terms of the normalised emittance ϵ_n,

$$\bar{\sigma}_b = \left(\frac{2\sqrt{2}\rho\epsilon_n}{\epsilon \bar{a}_w l_g} \right)^{\frac{1}{2}} \tag{19}$$

where l_g is the gain length of the FEL, and $\bar{\sigma}_b$ is the Gaussian radius in $\bar{x}$ and $\bar{y}$.

A simulation to test the beam matching effects was performed. The parameters used were

$$\rho = 0.015, l_b = 4l_c, \epsilon_n = 10^{-6}\mu\ m, \bar{a}_w = 1.5,$$
$$f_x = f_y = 1, \gamma_r = 489, \lambda_w = 0.03m,$$

and electron beam shot noise is simulated via the method of [7]. The beam radius should therefore be ≈ 1.61. The field evolution and interaction is artificially switched off, so the electrons travel unpeturbed through the wiggler. This allows the effect of only the focussing term on the electron motion to be observed.

The result is shown in figure 2. The matched beam radius is calculated by the code and the particles are then loaded according to the shot-noise model of [7]. It is seen that the noise introduces a small deviation from the matched beam radius giving a value of ≈ 1.56. The electron beam radius then exhibits a very small oscillation on

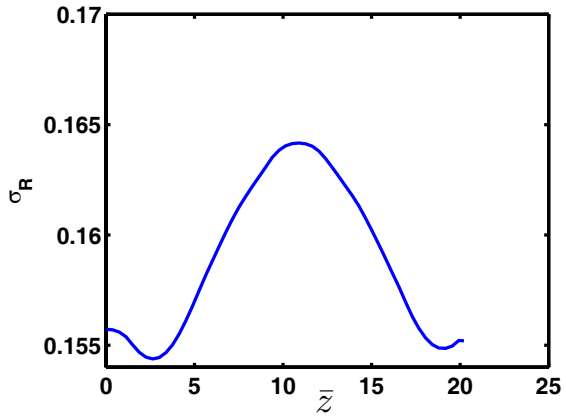

Figure 2: The radius of the electron beam as a function of propagation distance through the wiggler $\bar{z}$.

propagating through the wiggler. Increasing the number of macroparticles will decrease this small noise-oscillation.

A simulation including self consistent electron-field interaction is now shown. The electrons are seeded by a field with a constant gaussian profile in the tranverse plane. The scaled rms radius of the seed radiation intensity is chosen to match the rms value of the gaussian distribution of the electron beam $\bar{\sigma}_r = \bar{\sigma}_b$. Radiation diffraction was artifically switched off for this example. This will therefore show only the effects of the 3D electron beam on the system. The electron beam parameters are the same as for the previous example, the seed field peak intensity in $\bar{x}$ and $\bar{y}$ is chosen so that the scaled power is 10^{-3}. For comparison, simulations are performed both with and without the emittance and focussing. The results are shown in Fig. 3. For the case of no emittance or focussing the beam transverse monmentum has zero spread and therefore does not diverge even without a focussing channel. For the case with emittance and focussing the beam is matched and retains a constant radius as shown above. Hence any effects in the generation of radiation can be attributed to emittance and betatron effects only. The expected reduction in power generated and rate of the instability are clearly seen.

CONCLUSIONS

A new model for describing a 3D variably polarized FEL has been presented which uses an efficiently parallelised algorithm with finite elements to solve the working equations. A simple example of matching a 3D electron beam to a focussing channel and a diffraction-free FEL interaction were shown. The new code uses only publically available linear-solvers etc. and is intended for open-source release in the near future. A post processing visualization package is being worked on. The method of modelling diffraction is currently being updated from the method of [2] which utilized a complex envelope A to describe the radiation field. The new model uses the full field of the radiation i.e. including the fast oscillatory variations.

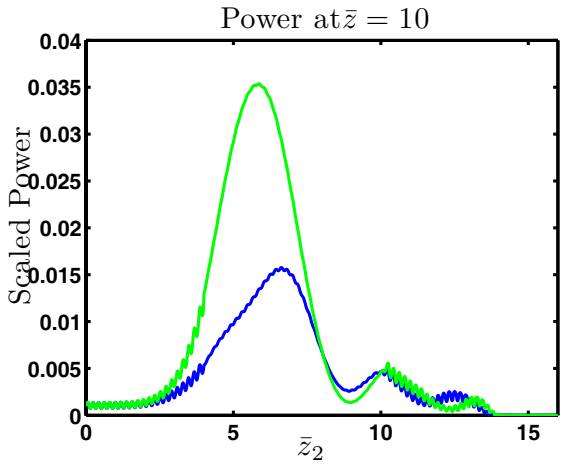

Figure 3: Power as a function of $\bar{z}_2$ after ≈ 10 gain lengths through the wiggler. Both simulations were run with identical parameters, one with emittance and beam focussing (blue) and one without (green).

REFERENCES

[1] C.K.W. Nam, P. Aitken and B.W.J. McNeil, Unaveraged Three Dimensional Modelling of the FEL, Proceedings of FEL 2008, Gyeongju, Korea

[2] L.T. Campbell and B.W.J. McNeil, A Fully 3D Unaveraged, Non-localised Electron, Parallelized Computational Model of the FEL, Proceedings of FEL 2009, Liverpool, UK

[3] B.W.J. McNeil and G.R.M. Robb, Phys. Rev. E **65**, 046503 (2002)

[4] R.H. Hardin and F.D. Tappert, *Applications of the split-step Fourier method to the numerical solution of nonlinear and variable coefficient wave equations*, SIAM Review, **15**, 423 (1973)

[5] K.H. Huebner, E.A Thornton and T.G. Byrom, *The Finite Element Method For Engineers*, Wiley (1995)

[6] R. Bonifacio R. Corsini et al, Rivista Del Nuovo Cimento Vol 15 N 11 (1993)

[7] B.W.J. McNeil M.W. Poole and G.R.M. Robb, Phys. Rev. ST - Acc. Beams **6**, 070701 (2003)

Appendix C

FEL2010 Paper 2

GENERATION OF VARIABLE POLARIZATION IN A SHORT WAVELENGTH FEL AMPLIFIER

L.T. Campbell*, B. Faatz**, B.W.J. M^cNeil*
*SUPA, Department of Physics, University of Strathclyde, Glasgow, UK
**DESY, Notkestrasse 85, 22607 Hamburg, Germany.

Abstract

To date, short wavelength Free Electron Laser amplifiers have generated linearly polarised radiation. For several important classes of experiment, variable polarisation is required. For example, in the wavelength range from 1.5 to 2.5 nm, light polarisation is important in characterising magnetic materials where measurements depend critically upon the handedness of the polarisation. It is therefore important that the polarisation does not fluctuate between measurements. In this paper, we study possible methods to generate variably polarised light and consider its shot-to-shot stability.

INTRODUCTION

Free Electron Lasers can now generate high intensity, fs pulses of linearly polarised radiation [1]. It is desirable to generate such radiation with circular polarization. It may be possible to modify existing facilities to generate circularly polarized light rather than build potentially expensive helical wiggler SASE FELs. Microbunched electron beams from existing planar wiggler SASE sources may be able to generate coherent circularly polarized radiation with similar powers to those of the existing planar wiggler FEL without extensive modification.

Conceptually, the simplest option is to inject microbunched electrons from a pre-saturated SASE planar wiggler FEL into a relatively short helical wiggler module. However, this may pose engineering challenges, and helical wigglers are significantly more expensive than planar wigglers. An alternative is the crossed planar wiggler scheme proposed in [2] and [3]. A secondary planar wiggler rotated 90° with respect to the first SASE wiggler will generate linearly polarized radiation perpendicular to that generated by the first wiggler. Ideally, the microbunched beam will radiate coherently and produce similar powers to that of the first wiggler in ~ 1.3 gain lengths [4] of the second wiggler. If a $\pi/2$ phase shift is supplied between the two wigglers the combined radiation of the 2 sources should sum to give circularly polarized light. However, since the second wiggler must be ~ 1.3 gain lengths to produce 'perfect' circular polarization, the system can only be optimised for one resonant wavelength for a given set of beam parameters.

A modified crossed planar wiggler proposed in [5] and shown schematically in Fig. 1 may remove this constraint. By dumping the radiation from the first SASE wiggler and then using two wigglers of equal length rotated 90° with respect to each other, the powers generated by the microbunched beam in each of these wigglers can be made equal and the polarization controlled by a relative phase shift between the two. The polarization stability of this scheme has been analyzed in [6], where 3D GENESIS simulations were used to calulate the radiation fields from the two crossed wigglers.

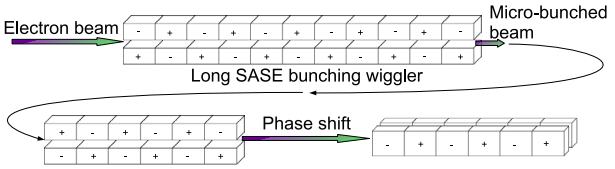

Figure 1: Illustration of the alterative crossed wiggler scheme from [5]

The unaveraged model presented in [7] describes a FEL with a variably polarised wiggler, and is capable of self-consistently describing the seperate transverse radiation fields through a common complex field. In addition, the model describes an extended radiation spectrum including significantly higher and lower frequency content simultaneously, subject to the Nyquist condition. The ability of this model to describe different radiation and wiggler polarizations accurately is discussed, and an example of how the crossed planar wiggler scheme can be simulated is shown with some preliminary results.

THE MODEL

Details of the derivation and scaling of the working equations may be obtained from [7] and are summarised here.

The FEL interaction is described by the coupled 3D Maxwell-Lorentz equations in a variable magnetic wiggler field defined as:

$$\mathbf{B}_w = \frac{B_w}{2}(\hat{\mathbf{f}}e^{-ik_w z} + c.c.) \tag{1}$$

where the unnormalized vector basis:

$$\hat{\mathbf{f}} = f_x\hat{\mathbf{x}} + if_y\hat{\mathbf{y}} \tag{2}$$

is used to define a variable polarized wiggler field and where B_w is the peak magnetic field strength. Hence, f_x and f_y describe the strength of the wiggler magnetic field in x and y. The vector basis $\hat{\mathbf{f}}$ is un-normalized so that the RMS magnetic field $\bar{B}_w$ varies from $B_w/\sqrt{2} \leq \bar{B}_w \leq B_w$ as the wiggler changes from planar to helical.

The electromagnetic field is defined as:

$$\mathbf{E}(x,y,z,t) = \frac{1}{\sqrt{2}}\left(\hat{\mathbf{e}}\xi_0 e^{i(kz-\omega t)} + \hat{\mathbf{e}}^*\xi_0^* e^{-i(kz-\omega t)}\right) \quad (3)$$

with complex envelope $\xi_0(x,y,z,t)$ and the normalized vector basis $\hat{\mathbf{e}} = \frac{1}{\sqrt{2}}(\hat{\mathbf{x}}+i\hat{\mathbf{y}})$ is defined with $\hat{\mathbf{e}}\cdot\hat{\mathbf{e}} = \hat{\mathbf{e}}^*\cdot\hat{\mathbf{e}}^* = 0$ and $\hat{\mathbf{e}}\cdot\hat{\mathbf{e}}^* = 1$. Projecting the field onto $\hat{\mathbf{e}}^*$ gives:

$$E_\perp = \xi_0 e^{i(kz-\omega t)} = E_x - iE_y \quad (4)$$

where E_x and E_y are the field components in x and y, or in terms of the scaled units of the working equations:

$$A_\perp = A\exp(-i(\bar{z}_2/2\rho)) = A_x - iA_y. \quad (5)$$

Rewriting the complex envelope A with an explicit magnitude and phase $A = |A|e^{i\psi}$ gives

$$A_x = |A|\cos(\bar{z}_2 - \psi) \quad (6)$$

$$A_y = |A|\sin(\bar{z}_2 - \psi) \quad (7)$$

For constant $|A|$ and ψ, these fields describe a circularly polarised field. More generally, if $|A|$ and ψ are both functions of $\bar{z}$ and $\bar{z}_2$ they can describe any polarization. This is what happens in the code which solves numerically for $A_\perp$: the radiation amplitide, phase and polarization evolve self-consistently, both driving, and being driven by, the transverse electron current due to a variable wiggler polarization. Unlike other simulation codes, the radiation field polarisation is not fixed with respect to any transverse axis. To obtain the complex envelope required for a given polarization equation (5) is re-arranged to obtain the real and imaginary parts of the envelope in terms of A_x and A_y. It can then be shown that the magnitude and phase of the envelope vary as:

$$|A| = \sqrt{A_x^2 + A_y^2} \quad (8)$$

$$\tan\psi = \left(\frac{A_x\sin(\bar{z}_2/2\rho) - A_y\cos(\bar{z}_2/2\rho)}{A_x\cos(\bar{z}_2/2\rho) + A_y\sin(\bar{z}_2/2\rho)}\right) \quad (9)$$

for the given polarization.

COMPUTATIONAL SOLUTION

The code which solves the combined electron-field interaction is described in more detail in [7]. The partial differential equations describing the field and electron variable evolution are solved using a Fourier split-step integration method, where the first half-step solves field diffraction using Fourier transform methods, and the second half step integrates the driven electron and field equations using a Runge Kutte 4th order and finite element method. All computation is performed in parallel and memory usage is spread evenly across processors increasing code efficiency.

VARIABLE WIGGLER POLARISATION SIMULATION

A general elliptical wiggler field can be varied from a linear to a full helical polarization with the electron beam having a corresponding transverse current. Simulations are now presented that demonstrate that the field and its polarization are driven consistently with such a variable transverse current.

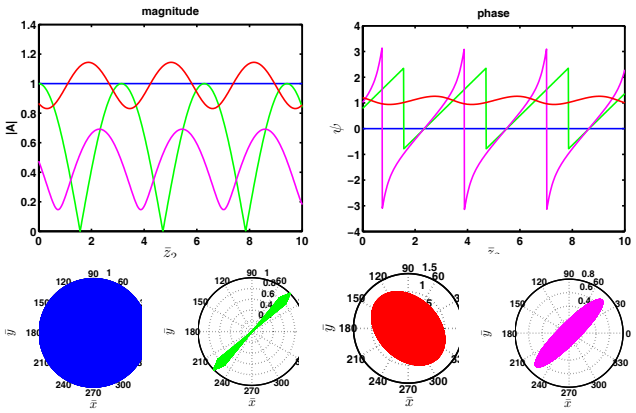

Figure 2: Illustration of how the complex envelope magnitude and phase vary to obtain different polarizations.

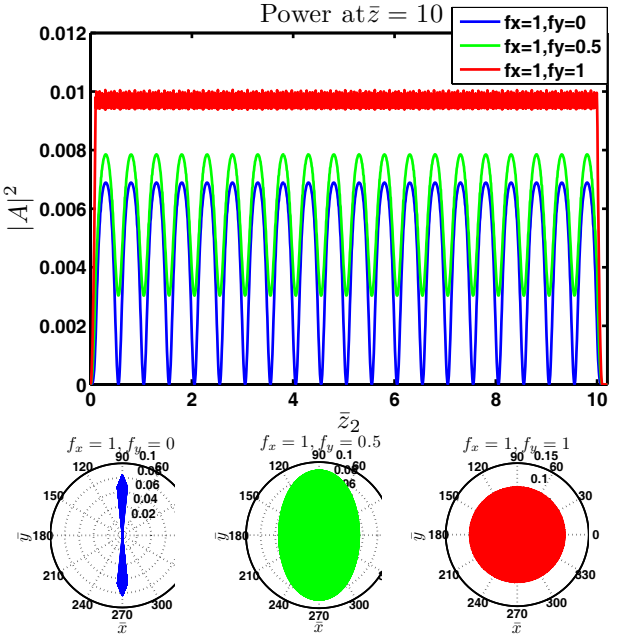

Figure 3: Example of different field polarizations as driven by electrons in planar, eliptical and helical wigglers as specified by f_x and f_y. The radiation polarization profiles are shown at the bottom, and the scaled powers on top.

In Figure 3 the x and y components of the radiation fields driven by a very short $\approx \lambda_r/10$ electron pulse propagating through three 20-period wigglers of different polarisation of are plotted. The electron pulse has a gaussian charge distribution and, being of sub-wavelength duration, behaves almost like a single high-charge particle emitting coherently. The self-consistent interaction of the field on the electrons was artificially switched off. The wiggler parameter $\bar{a}_w = 0.5$, so there is a relatively small harmonic content. The FEL parameter $\rho = 0.0796$. This simulation

demonstrates that the electrons drive the correct field polarization via the complex field. Note that the scaled 'instantaneous power' $\propto |E_\perp|^2$, i.e. including the fast oscillatory field term, has been plotted. The sinusoidal amplitude of the electric field is evident in the planar and elliptical cases whereas the non-oscillatory ampluitude of the electric field in the helical case gives a continuous instantaneous power.

PRELIMINARY RESULTS FROM A CROSSED PLANAR FEL SYSTEM

Although the crossed planar wiggler scheme of [5] in principle allows tunable circular polarization in SASE, the electron bunching is initially noisy. Such bunching may impede the ability of this scheme to achieve good circular polarization. This is because the phase slippage induced to achieve the circular polarisation, even for relatively small wiggler lengths and phase shifts, may not allow good amplitude and phase matching of the electric fields to give the desired polarisation. A simulation with the unaveraged code to examine the effects of this is now outlined and preliminary results presented.

An electron pulse of 40 cooperation lengths is propagated through a long planar wiggler to just before saturation, approx 17.5 gain lengths. The FEL parameter was set to $\rho = 0.01$. This is larger than typical values for short wavelength SASE FEL's however it reduces the computational load and enables initial predictions and investigation of the principles to be made quickly.

The noisy radiation output and bunching is typical of the SASE process. A cold, flat top current distribution was used so that a large fraction of the beam evolves only from shot-noise. However, as this is an unaveraged code, CSE is generated at the edges of the beam, with that from the back developing into a superradiant spike. The front 15 cooperation lengths of the electron pulse have been untouched by superradiant SACSE spike evolution and have evolved only from shot-noise. To artificially remove CSE effects,

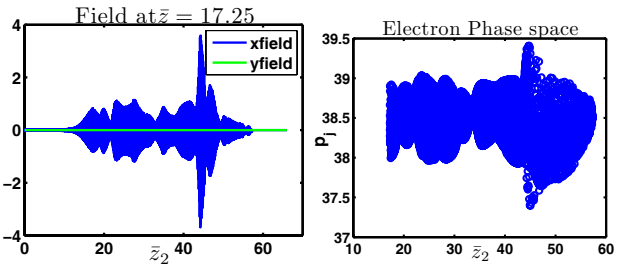

Figure 4: Simulation of the SASE bunching FEL. On the left is a plot of the x and y fields at the end of the wiggler. On the right is the electron phase space. Note the SACSE spike at $\bar{z}_2 \approx 42$. In the $\bar{z}_2$ frame the tail of the pulse is to the right and the head to the left. A section of the electron pulse from $\bar{z}_2 = 17.25$ to 32.25 which has evolved from noise only (no CSE) was selected for input into the crossed planar FEL.

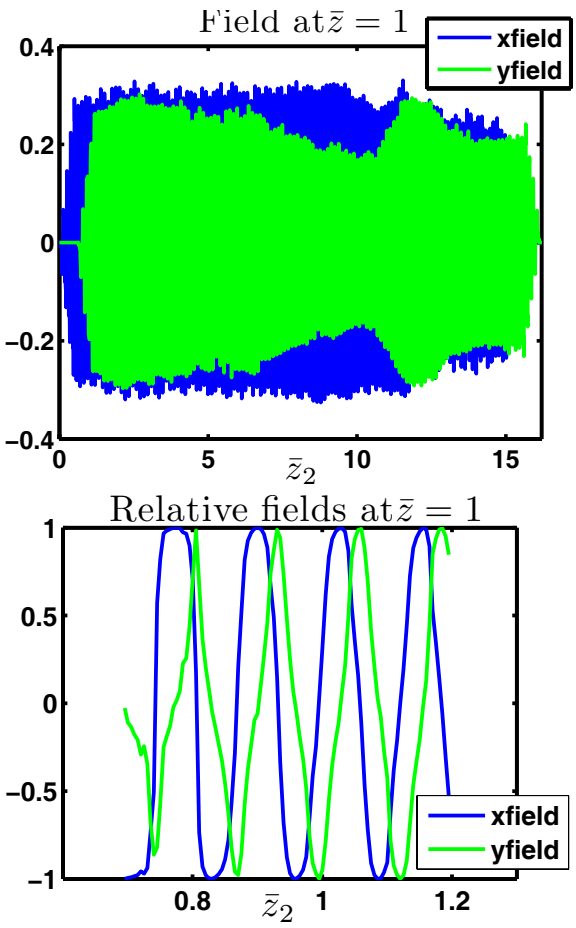

Figure 5: Simulation of the crossed planar FEL. The micro bunched electron beam has propagated to $\bar{z} = 1$. The wiggler polarization was switched from a planar in y to a planar in x and a $\pi/2$ phase shift added at $\bar{z} = 0.5$. The x and y fields are shown here, the bottom plot is enlarged to show the structure of the fields, and the magnitudes are scaled to the total magnitude of the radiation vector for ease of comparison.

this section only of the beam was selected for input into the two crossed planar wigglers with the remainder of the beam discarded.

The shortened beam was then injected into a combined cross wiggler a total of 1 gain length long. As the beam had been pre-bunched, high power radiation is emmitted in both wigglers sections. After one half a gain length the planar wiggler polarization was rotated by $\pi/2$, to change from a y to x polarized planar wiggler, and a $\pi/2$ phase shift was added to the electron beam.

Figure 5 shows the resulting transverse radiation fields. As this model is unaveraged the higher harmonics evolve self consistently and the odd harmonics of the planar wiggler are seen in Fig. 6. The waveforms in Fig. 5 show the fields in both planes are modulated, possibly by the harmonic content, which may adversely affect the generation of good circular polarization. The scaled instantaneous radiation power $|A_\perp|^2$ shows significant modulation indicat-

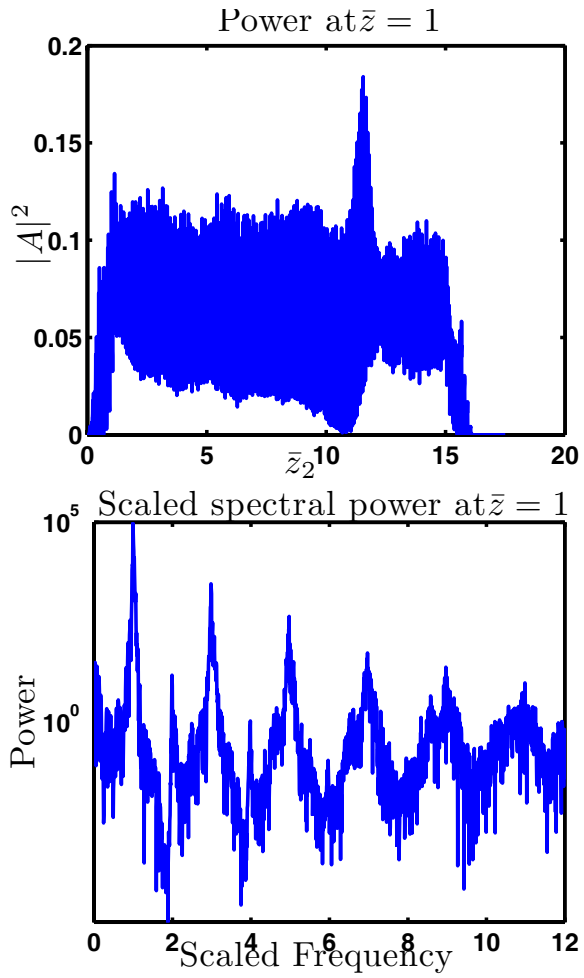

Figure 6: Simulation of the crossed planar FEL. On top is the scaled power, and the bottom shows the frequency content of the signal scaled to the frequency of fundamental.

ing that the degree of circular polarization of the radiation is quite poor. Also note that the amplitude of the y component of the radiation field is less than that of the x component. This may result from electron de-bunching in the first y polarized planar wiggler reducing power output in the second x polarised wiggler. Further optimisation may mitigate such effects.

CONCLUSION

The model presented here is a potentially powerful tool for investigating variable polarization effects in the FEL, allowing fully variably polarized wigglers and radiation fields to be modelled self consistently. The examples shown are 'work in progress' and, although rudimentary, demonstrate the potential of the code to investigate polarization phenomena in FEL physics. The example simulation of the crossed planar FEL is an initial step towards examining how the beam characteristics affect the final field polarization. The field polarization must now be described in a quantitative manner, for example via Stoke's parameters. The form of the transverse field components are written here in terms of the common complex field envelope. To determine the Stokes' parameters this description must now be related to the independently varying magnitude and phase of the transverse fields.

REFERENCES

[1] P. Emma, R. Akre, J. Arthur et al, Nature Photonics **10** 1038 (2010) Avialable from `http://www.newlightsource.org/`

[2] K.J. Kim, Nucl. Instr. and Meth. **219**, 42 (1984)

[3] K.J. Kim, Nucl. Instr. and Meth. **445**, 329 (2000)

[4] Y. Ding, Z. Huang, Phys. Rev. S.T. **11**, 030702 (2008)

[5] Y. Li, B. Faatz, J. Pflueger, E.A. Saldin, E.L. Schneidmiller, M.V. Yurkov, Study of controllable polarization SASE FEL by a crossed planar wiggler, Presented at the European Particle Accelerator Conference, Italy, (2008)

[6] Y. Li, B. Faatz, J. Pflueger, 3D polarization properties for crossed-planar undulators, DESY print TESLA-FEL 2010-0, Hamburg (2010)

[7] L.T. Campbell and B.W.J. McNeil, A Fully 3D Unaveraged, Non-localised Electron, Parallelized Computational Model of the FEL, Proceedings of FEL 2010, Malmo, Sweden (*ibid*).

Appendix D

CD Containing Code